

University of Alberta

The Design and Manufacture of a Comb-Driven Micropump

by

Else Elizabeth Gallagher



**A thesis submitted to the Faculty of Graduate Studies and Research
in partial fulfillment of the requirements for the degree of**

Master of Science

Mechanical Engineering

**Edmonton, Alberta
Spring 2007**



Library and
Archives Canada

Bibliothèque et
Archives Canada

Published Heritage
Branch

Direction du
Patrimoine de l'édition

395 Wellington Street
Ottawa ON K1A 0N4
Canada

395, rue Wellington
Ottawa ON K1A 0N4
Canada

Your file *Votre référence*
ISBN: 978-0-494-29959-3
Our file *Notre référence*
ISBN: 978-0-494-29959-3

NOTICE:

The author has granted a non-exclusive license allowing Library and Archives Canada to reproduce, publish, archive, preserve, conserve, communicate to the public by telecommunication or on the Internet, loan, distribute and sell theses worldwide, for commercial or non-commercial purposes, in microform, paper, electronic and/or any other formats.

The author retains copyright ownership and moral rights in this thesis. Neither the thesis nor substantial extracts from it may be printed or otherwise reproduced without the author's permission.

AVIS:

L'auteur a accordé une licence non exclusive permettant à la Bibliothèque et Archives Canada de reproduire, publier, archiver, sauvegarder, conserver, transmettre au public par télécommunication ou par l'Internet, prêter, distribuer et vendre des thèses partout dans le monde, à des fins commerciales ou autres, sur support microforme, papier, électronique et/ou autres formats.

L'auteur conserve la propriété du droit d'auteur et des droits moraux qui protègent cette thèse. Ni la thèse ni des extraits substantiels de celle-ci ne doivent être imprimés ou autrement reproduits sans son autorisation.

In compliance with the Canadian Privacy Act some supporting forms may have been removed from this thesis.

Conformément à la loi canadienne sur la protection de la vie privée, quelques formulaires secondaires ont été enlevés de cette thèse.

While these forms may be included in the document page count, their removal does not represent any loss of content from the thesis.

Bien que ces formulaires aient inclus dans la pagination, il n'y aura aucun contenu manquant.


Canada

To

Eric Finley

Certainly I will be a master in my field
when I have taught you
as much as you've taught me.

Abstract

This work presents two attempts that were made at designing and manufacturing a comb-driven micropump, with the intention of extending the capabilities of micropumps and exploring those of comb drives. The first attempt involved pairing a new type of micropump with a standard comb drive. An initial design was completed, along with some preliminary process optimization, but ultimately it was decided that standard comb drives on their own may not be the best type of actuator for micropumps. The second attempt involved pairing a new type of comb drive with a standard micropump. Again, an initial design was completed, along with some preliminary process optimization. In this case, however, more extensive research will need to be done to determine whether this type of comb drive is useful for actuating micropumps, although some of the workings of the new comb drive were able to be characterized much more thoroughly.

Acknowledgements

The fabrication of the prototypes and most of their testing was carried out in the University of Alberta NanoFab. The author would like to thank Ken Westra and Shane McColman, in particular, for process advice and training. Murray Paulson at BigBangwidth assisted with some preliminary testing of the lateral comb-driven prototypes, and Graham McKinnon of Norcada gave advice on the design and fabrication of the vertical comb-driven prototypes. The author would also like to thank Dr. Henry van Roessel of the Department of Mathematical and Statistical Sciences at the U of A for an invaluable conversation regarding elliptic functions.

Tiansheng Zhou gave advice on the design and fabrication of the lateral comb-driven prototypes, as well as took the SEM pictures of them that appear near the end of Chapter 3. Yan Loke gave advice on the fabrication of the vertical comb-driven prototypes. The author would also like to thank Micralyne, as well as NSERC and MSTR, for funding of the project.

Table of Contents

Chapter 1: Introduction	1
1.1 Objective of Research	1
1.2 Overview of Thesis	2
Chapter 2: Background	3
2.1 MEMS and Micromachining	3
2.1.1 Depositing or Growing Material Layers	3
2.1.2 Photolithography	4
2.1.3 Etching Material Layers	5
2.2 Micropumps	6
2.3 Comb Drives	9
2.3.1 Comb Drive Theory	10
2.3.2 Typical Fabrication Processes	11
Chapter 3: Lateral Comb-Driven Micropump	16
3.1 Design Considerations	16
3.2 Prototype Design	16
3.2.1 Piston Design	17
3.2.2 Valve Design	17
3.2.3 System Design	18
3.3 Prototype Variations	18
3.4 Mask Design	22
3.5 Fabrication	22
3.5.1 Mask Fabrication	23
3.5.2 Prototype Fabrication	23
3.6 Fabrication Results	24
3.7 Prototype Testing	25
3.8 Design and Process Recommendations	26
3.9 Finite Element Simulations	27
3.9.1 Building the Models	27
3.9.2 Analysing the Models	28
3.10 Conclusions	28
3.11 Next Steps	29
Chapter 4: Vertical Comb-Driven Micropump	44
4.1 Design Considerations	44
4.2 Process Selection and Modification	45
4.2.1 Process Selection	45
4.2.2 Process Modification	46
4.3 Evolution of Design	47
4.4 Design Calculations	48
4.4.1 Weight Considerations	48
4.4.2 Vertical Spring Constant	49
4.4.3 Side-Sticking Criteria	50
4.5 Design Variations	51
4.6 Performance Predictions	54

4.6.1 Natural Frequency	54
4.6.2 Piston Displacement	55
4.6.2.1 Numerical vs. Analytical Prediction of Net Electrostatic Force	57
4.6.2.2 Full-Model Simulation Results	58
4.7 Examination of Assumptions Made in Derivation of Analytical Fringe-Correction	58
4.7.1 Effect of w on Net Electrostatic Force	58
4.7.2 Effect of s on Net Electrostatic Force	59
4.8 Derivation of Numerical Fringe Correction	60
4.9 Prototype Fabrication	61
4.9.1 Mask Design	61
4.9.2 Processing Completed	62
4.9.3 Process Recommendations	64
4.10 Conclusions	65
Chapter 5: Conclusion	81
5.1 Future Work	83
Bibliography	84

List of Tables

Table 3.1: A comparison of prototype design characteristics.	32
Table 4.1: A summary of the dimensions and other characteristics of the three piston designs.	70
Table 4.2: The first three natural frequencies of the piston designs predicted with finite element simulations.	73
Table 4.3: A summary of the final displacements of the three pistons predicted with different electrostatic theories.	76
Table 4.4: The coefficients of the fringe-correction derived from simulation data.	79

List of Figures

Figure 2.1:	Isotropic etch profiles.	13
Figure 2.2:	The Bosch process – (a) isotropic etching of the substrate, (b) deposition of the passivation layer, (c) anisotropic etching of the passivation layer followed by isotropic etching of the substrate.	13
Figure 2.3:	A typical reciprocating displacement micropump. Adapted [8].	13
Figure 2.4:	A reciprocating displacement micropump with a parallel-plate electrostatic driver. Adapted [8].	14
Figure 2.5:	A typical comb drive machined from an SOI wafer.	14
Figure 2.6:	Opposing comb teeth and their dimensions that have a large effect on the electrostatic forces between them.	14
Figure 2.7:	An older method for fabricating comb drives. Adapted [15].	15
Figure 2.8:	A newer method for fabricating comb drives.	15
Figure 3.1:	A top view of the comb drive used for pairing with a new type of reciprocating displacement micropump. Model drawn in IntelliSuite™'s IntelliMask™ module.	31
Figure 3.2:	A top view of the main components of the comb-driven micropump. The dark regions indicate the parts of the device layer of the SOI wafer that will remain after it has been etched through. Model drawn in IntelliSuite™'s IntelliMask™ module.	31
Figure 3.3:	The arrangement of the springs and combs for configurations C and D (a); and that for configuration E (b). Models drawn in IntelliSuite™'s IntelliMask™ module.	32
Figure 3.4:	The process followed in the fabrication of the lateral comb-driven prototypes.	33
Figure 3.5:	A top view of one of the prototypes on completion of the DRIE process step.	34
Figure 3.6:	The tops of the lattice structures that lost their masking oxide and were etched during the DRIE process step.	35
Figure 3.7:	The tapered bottom edge of a spring.	35

Figure 3.8:	A comparison of the thickness of the spring beams and lattice structures relative to that of the wider structures.	36
Figure 3.9:	A comparison between the designed cross-section of the spring beams (left) and the estimated actual cross-sections of the prototype beams (right).	37
Figure 3.10:	A spring beam (of configuration E) broken free of its piston shaft.	38
Figure 3.11:	A spring beam (of configuration E) that has broken from the piston shaft, and comb pairs with oxide remaining between their teeth.	38
Figure 3.12:	A schematic showing how the electrical circuit was applied to the prototypes during testing.	39
Figure 3.13:	A movable comb that has broken free of its handle wafer.	39
Figure 3.14:	The actuation of a movable comb. (a) shows the undeformed shape; (b) shows the deformed shape.	40
Figure 3.15:	A bottom view of the finite element model of the movable comb of configurations A and B. The model was built in IntelliSuite™'s 3D Builder™ module.	40
Figure 3.16:	The mode shape of the first natural frequency of configuration E. The mode shape was calculated in ANSYS®.	41
Figure 3.17:	Another type of lateral comb-driven micropump. Adapted [18].	42
Figure 3.18:	A schematic of a typical vertical comb drive. Adapted [31].	43
Figure 4.1:	The electrostatic forces that act on a movable tooth in the z - and x -directions when a voltage difference is applied between the fixed and movable combs.	66
Figure 4.2:	The process decided upon for the fabrication of the vertical comb-driven prototypes.	67
Figure 4.3:	A schematic of the double-gimbaled two-axis tilting micromirror that the chosen fabrication process is intended to make. Adapted [26].	68
Figure 4.4:	Schematics of the basic piston design at rest (a) and during actuation (b). Model built in IntelliSuite™'s 3D Builder™ module and deformed in the ThermoElectroMechanical Analysis™ module.	68

Figure 4.5:	A close-up of the piston schematic showing the dimensions of the spring beams. Model built in IntelliSuite™'s 3D Builder™ module.	69
Figure 4.6:	Side-views of the wide spring beams. (a) shows the relationship between the displacement of their ends and the angles they are raised to; (b) the forces and moments exerted on their ends.	69
Figure 4.7:	An electrostatic boundary element mesh of a unit comb drive showing the w and s dimensions. Model built in IntelliSuite™'s 3D Builder™ and ThermoElectroMechanical Analysis™ modules.	73
Figure 4.8:	The model used to estimate the natural frequencies of the three piston designs. $k_b = 2KG/L_s$.	73
Figure 4.9:	A schematic of opposing comb teeth showing the difference between the electrostatic forces occurring within the region directly between them (local forces), and the electrostatic forces occurring outside of this region (global forces). Adapted [39].	74
Figure 4.10:	A schematic of opposing comb teeth displaying some of the dimensions used in the analytical fringe correction given in Equations 4.10 – 4.19.	74
Figure 4.11:	A comparison of the proposed electrostatic force models on prototypes A (a), B (b), and C (c).	76
Figure 4.12:	A study of the effect of tooth width, w , on the magnitude of the electrostatic force exerted on the movable teeth of a comb drive.	77
Figure 4.13:	A study of the effect of the distance between the ends of the teeth and the inside walls of the opposing combs, s , on the magnitude of the electrostatic force exerted on the movable teeth of a comb drive.	77
Figure 4.14:	The simulation data used to derive the numerical fringe correction.	78
Figure 4.15:	The surface (a) fit to the simulation data and a contour plot (b) of this same surface.	78
Figure 4.16:	An SEM picture of the cross-section of one of the Bosch-etched coin-rolled wafers.	79
Figure 4.17:	An SEM picture of a thin spring beam Bosch-etched from one of the coin-rolled wafers.	80

List of Symbols

- ε – the permittivity of the medium between the comb teeth
- θ – the angle the wide spring beams of the vertical comb-driven prototypes are raised to as their movable combs displace
- a' – the position of the surface of a movable tooth farthest away from the fixed teeth in the direction it would displace in
- A_c – the area that fixed and movable combs overlap
- α_s – half of the thickness of the thin spring beams of the vertical comb-driven prototypes
- b' – the position of the surface of a movable tooth closest to the fixed teeth in the direction it would displace in
- b_s – half of the width of the thin spring beams of the vertical comb-driven prototypes
- C – the capacitance between the opposing comb pairs
- c' – the position of the surface of a fixed tooth farthest away from the movable teeth in the direction they would displace in
- d' – the position of the surface of a fixed tooth closest to the movable teeth in the direction they would displace in
- E – the modulus of elasticity of the material being considered
- F – the incomplete elliptic function of the first kind
- f_a – the analytical fringe-correction found in the literature
- F_e – the net electrostatic force exerted on the movable combs
- F_{ex} – the electrostatic force exerted on the side of a movable tooth in the direction that would decrease the gap, g , between it and its adjacent fixed tooth
- f_s – the proposed numerical fringe-correction
- F_{un} – the unbalanced electrostatic force exerted on the movable combs due to misalignment between them and the fixed combs

- G – the bulk shear modulus of the material being considered
- g – the horizontal gap between the sides of opposing comb teeth
- I – the moment of inertia of a beam's cross-section
- K – the factor replacing the polar moment of inertia in the standard expression for torsion in circular cross-sections so that it can be used for rectangular cross-sections
- k_{\perp} – the spring constant of a fixed-fixed beam for the case where one of its ends is displaced in a direction perpendicular to its length
- k_x – the spring constant of the spring beams that anchor the movable combs to the substrate, in the direction of the movable combs' displacement, x
- k_z – the spring constant of the spring beams that anchor the movable combs to the substrate, in the direction of the movable combs' intended displacement
- L – the length of a spring beam of a lateral comb drive
- L_b – the effective length of the wide spring beams of a vertical comb-driven prototype
- L_s – the length of the thin spring beams of a vertical comb-driven prototype, each set between the end of a wide spring beam and a movable comb
- L_t – the dimension by which the fixed and movable comb teeth overlap that does not vary with the motion of the movable combs
- M – the moments exerted by the thin spring beams of the vertical comb-driven prototypes on the ends of the wide spring beams
- m – the mass of a structure
- n – the total number of movable teeth of a comb drive
- o – the initial offset between opposing combs
- p – the natural frequency of a structure corresponding to a particular mode shape
- q_e – the total charge on the capacitor formed by opposing comb pairs
- t – the thickness of the movable teeth of a vertical comb-driven prototype

- t_f – the dimension of a fixed comb tooth in the direction of the movable comb's displacement (ie. the thickness of a fixed tooth in a vertical comb drive)
- t_m – the dimension of a movable comb tooth in the direction of its displacement (ie. the thickness of a movable tooth in a vertical comb drive)
- U – the electrical potential energy stored in the capacitor formed by opposing comb pairs
- V – the voltage difference between the fixed and movable combs
- x – the distance the movable combs travel from their original positions, in the direction that changes the gap, g , between them and the fixed combs
- z – the distance the movable combs travel from their original positions, in the direction of intended actuation
- z' – an alternate scale with which to measure the displacement of the movable combs; its origin is where the movable combs align with the fixed in the direction of their intended actuation

Abbreviations

- BOE – buffered oxide etch
- DRIE – deep reactive ion etching
- HMDS – hexamethyldissilazane
- ICP – inductively coupled plasma
- IPA – isopropyl alcohol
- LPCVD – low pressure chemical vapour deposition
- MEMS – microelectromechanical systems
- RF – radio frequency
- RIE – reactive ion etching
- SCS – single-crystal silicon
- SEM – scanning electron microscope
- SOI – silicon-on-insulator
- UV – ultraviolet light

Chapter 1: Introduction

1.1 Objective of Research

Microscale mechanical systems – comprised of anything from diaphragms and spring beams to valves and microchannels, and usually driven and/or monitored electrically – have great potential in furthering the medical, space, computer, and communications industries, among others. Known as MEMS (microelectromechanical systems), their size and batch fabrication make them portable, implantable, lightweight and disposable, and allow the devices they are placed in to operate automatically. Being a relatively new technology, however, there are still limits to the fabrication processes that can be used to manufacture them, which must be given particular consideration in their design.

Micropumps are a type of MEMS that are made up of arrangements of drivers, channels, and valves, often in a manner very similar to their macroscale counterparts. They too have a number of important applications in a variety of fields; however, while many different types of drivers and arrangements of channels and valves have been studied, micropumps are still limited in the needs they can fulfill. Continuing to study new types of drivers and arrangements of micropump components is thus a worthy endeavor, as there are many that have yet to be fully explored.

Comb drives are a type of actuator in MEMS that provide reciprocating motion, typically parallel to their respective substrates, as electrostatic forces alternately draw their movable components in one direction, and springs restore them to their original positions. They also have many applications, but may have many more, and, as an emerging technology, should be studied further so that they may be understood, and characterized, more thoroughly. While it is known that they have a number of advantages over other types of actuators, for instance, the foremost among them being that their electrostatic forces are generated between plates that move parallel to each other (so that these forces can be approximated as remaining constant over the displacement of the plates), it is not well understood what range of movement this assumption is valid within, nor what the electrostatic forces are outside of this range, if not constant.

The objective of the research presented here is thus to explore the capabilities of comb drives, particularly their potential for actuating micropumps, by designing a system where the two are connected such that the former actuates the latter.

1.2 Overview of Thesis

Two attempts were made at designing a system where a comb drive is used to actuate a micropump. These are described in Chapters 3 and 4, after micropumps, comb drives, and microfabrication in general are discussed more thoroughly in Chapter 2.

The first attempt made at designing a comb-driven micropump, described in Chapter 3, is based on pairing a standard comb drive with a new type of pump design. The design includes a piston and valves that can be machined beside the comb drive with minimal added process steps. The chapter describes this design, as well as what has been completed in terms of the fabrication of prototypes – which is an initial round involving only the typical process steps for the comb drives, so that the details of these steps may be tested before further steps are carried out to finish the pumps. The chapter also describes the results of the prototype testing, outlines recommendations on how the prototype design and fabrication process may be improved, and states reasons for the focus of the research shifting to a different approach.

The second attempt made at designing a comb-driven micropump, described in Chapter 4, is based on pairing a new type of comb drive with the most common type of micropump design. In this attempt the pump itself was not designed, only the piston that would relay a reciprocating motion to it, as well as the driver for the piston. A fabrication process for the new type of comb drive was selected from the literature and simplified for its intended purpose, and a comb drive was designed from it similar to that which the process was originally intended for. Sets of governing equations (considering the forces that would be exerted on the movable components of the comb drive by the springs attached to them, etc.) were assembled to assist in deciding on the dimensions of the prototypes.

While some preliminary fabrication of the prototypes was done, and some initial recommendations contemplated on the optimization of the process followed, during the design of the prototypes it was realized that a special consideration needs to be made for this new type of comb drive when used for linear reciprocating motion. It does not have the same advantage as regular comb drives in that the range over which its electrostatic forces can be assumed to remain constant is very short. Some literature was found that derived an analytical expression to better characterize the electrostatic forces acting on the comb drive's movable components. In Chapter 4 it is compared to finite and boundary element simulation, and the performance of the prototypes is predicted. Finally, an alternate expression to characterize the electrostatic forces within comb drives is derived from the conducted simulations and is presented towards the end of Chapter 4.

Chapter 2: Background

2.1 MEMS and Micromachining

Small, mechanical systems connected to circuits made with processes derived from nanoscale circuit-making technology, MEMS are often smaller versions of macroscale systems such as pumps, rotors, accelerometers, switches, and pressure and chemical sensors that are more portable and implantable than their larger counterparts. With perhaps an overall size on the order of millimeters, the dimensions of their components are in the micrometer range. They tend to either receive electrical input to produce mechanical motion (perhaps indirectly, with several energy conversions in between (i.e. electrical, to thermal, to pneumatic)), or receive mechanical stimuli to produce electrical signals.

While machined with similar techniques as nanoscale electrical circuits, MEMS are also machined from similar materials. They have metals such as gold to conduct electricity, and insulators such as silicon dioxide to isolate conductive components of different potentials. They are usually etched from or from layers on top of a substrate or wafer that is often composed of single-crystal silicon (SCS), itself a semi-conductor. Of particular relevance to the research at hand are silicon-on-insulator (SOI) wafers, which consist of two SCS wafers bonded together with a layer of silicon dioxide between them. The top wafer is usually polished down to become the device layer of the SOI wafer, while the bottom or handle wafer is left at its original thickness of a few hundred micrometers.

The micromachining of MEMS consists largely of applying chemicals to layers of different materials arranged such that the top layers shield portions of the layers below them and the exposed portions of the bottom layers are etched away by the chemicals. Thus the design of MEMS involves deciding which portions of the structural layers will be shielded, and what depths their exposed portions will be etched to (i.e. the lengths of time the chemicals will be applied to them). Descriptions of the specific fabrication techniques used or considered in the research presented here are given in the following sections.

2.1.1 Depositing or Growing Material Layers

Depositing or “sputtering” metal onto the surface of a substrate to act as a shielding layer, or to make the surface more conductive (and perhaps assist in adhering wires from an external circuit to its MEMS components), is typically done in a vacuum chamber containing two electrodes at differing potentials. The wafers to be covered in metal are placed on the anode, and the target (a disc of the material to be deposited, kept at a negative potential) is mounted on the cathode [1]. A small amount of an inert gas (usually argon) is injected into the chamber

and ionized by the high voltage between the electrodes. The electric field between the electrodes accelerates the positive ions towards the target, where they transfer their momentum to the metal atoms. Whole, neutral atoms become dislodged from the target and condense on the substrate at the anode [2]. Good adhesion of the metal layer is achieved by high-energy bombardment of the substrate – the momentum transferred to the metal atoms is enough for the first few that reach it to penetrate its surface. The low pressure in the chamber allows the metal atoms to keep their energy as they traverse the distance between the electrodes, producing a higher density and purity of the deposited metal. The pressure is high enough, however, that good step coverage (uniformity over previously patterned layers) is also achieved, as the metal atoms undergo enough collisions on their way to the substrate that they arrive at random angles [3].

Silicon can also be deposited on wafers – not in its single crystal form, but as a granular, amorphous solid usually referred to as polysilicon [3]. In a low pressure furnace kept at around 600°C, silane (SiH_4) is pyrolysed – an endothermic decomposition process – to produce silicon, which is deposited on the wafers, and hydrogen gas [4]. Low pressure chemical vapour deposition (LPCVD) of polysilicon is slow, however. It can take days to deposit more than a few micrometers [3], and it needs to be annealed afterwards to reduce the stresses inherent to it [5, 6]. In similar processes, “low temperature” silicon dioxide (SiO_2) can also be deposited out of the vapour phase from the reaction of silane with oxygen in a furnace kept at around 400°C [3], and silicon nitride can be deposited by the reaction of ammonia (NH_3) with dichlorosilane (SiCl_2H_2) in a furnace kept at around 800°C [3, 4].

A more common way to form a layer of silicon dioxide on a silicon substrate, however, is to grow it. A silicon surface will naturally oxidize when in contact with air; this process can be enhanced with the addition of heat and water vapour. This is typically done in a furnace kept at around 1000°C, that pure water vapour is injected into and the by-product of hydrogen gas is expelled out of. The high temperature allows relatively thick oxide layers (usually of an amorphous type) to form quickly by aiding the diffusion of the oxygen atoms through the already-formed oxide so that they may react with the silicon interface. Because part of the silicon is consumed in this process (a layer with a thickness of approximately 44% of the final thickness of the oxide layer) good adhesion of the oxide is achieved [3, 4].

2.1.2 Photolithography

What determines the patterns of the deposited material layers that shield the etches of the layers below them is typically the prior patterning of a radiation-sensitive polymer layer by selective exposure to ultraviolet (UV) light [3, 4]. The radiation-sensitive polymer, or *photoresist*, is poured onto the wafers while they are spun at high speeds so that the liquid’s inertia draws it outwards to cover the wafers and thins it to a particular, predictable, thickness. Afterwards the wafers are usually soft baked – placed on a hotplate for a few seconds to remove solvents and stress from the photoresist and to promote its adhesion to the wafers.

The selective exposure of the photoresist to UV light occurs through a mask – a glass wafer, itself transparent to UV light, that has a patterned opaque layer on one side (usually of chromium). The patterned side of the mask is placed over the photoresist on the wafer to be patterned, and brought into direct, vacuum contact with the wafer to produce a 1:1 image. The UV light shining through the mask alters the chemistry of the photoresist on the wafer so that it is either more or less soluble in a developer solvent. The photoresist used in the research described here is of a positive type, meaning that UV radiation weakens the polymer in the exposed areas such that it is these that are etched away in the developer. After immersion and agitation for a set time in a dish containing the developer, the wafers are often hard baked for a few minutes in an oven. This process increases the resistance of the photoresist to subsequent etching steps.

The masks themselves are made by a similar process. The glass wafers start with a layer of photoresist over un-patterned chromium, which is exposed with a laser system directed by a computer containing a drawing file of the mask design. The photoresist is then developed, parts of the chromium etched away, and the rest of the photoresist is removed.

2.1.3 Etching Material Layers

Etching is a process wherein material is removed from the exposed sections of the layers by having it react with a chemical applied to it such that the products of that reaction diffuse back into the etchant. The simplest, most basic method of applying chemicals to the wafers is to immerse them in solutions of the chemicals. This method tends to produce isotropic etches, where the same amount of material is removed in all directions beyond the openings in the masking layers. As shown in Figure 2.1(a), this leads to undercutting of the masking layers, such that the final widths of the trenches etched are larger than the holes in the masks. If only narrow areas are shielded from the etchant, the undercut can be enough to completely remove the material beneath them. This technique can be used to release some structural elements from a substrate while leaving wider elements attached, as shown in Figure 2.1(b).

To achieve anisotropic etches, the chemicals are usually applied to the wafers in the form of plasmas. A type of anisotropic etching, reactive ion etching (RIE) is a combination of physical sputtering and chemical reactions, involving chemically reactive species (ions, etc.) that are generated from an otherwise inert gas [3, 4]. These react with the material to be etched to produce volatile reaction products that evaporate back into the plasma, which are eventually removed from the chamber with a vacuum pump. While a plasma on its own, like a chemical solution, will tend to produce isotropic etches, the reactive species within it can be directed with a radio frequency (RF) field such that the wafers are bombarded more heavily with the ions from a direction perpendicular to the wafer surfaces. With optimized process parameters, this can produce relatively deep, narrow trenches in the wafers with almost no undercut at all. Typically, this process is carried out by mounting the wafers directly on the cathode of a diode-type reactor (a vacuum chamber with two RF electrodes) similar to that used for sputtering, so

that positive ions can be accelerated towards the wafer surfaces with a bias generated between the wafers and the plasma.

To produce even higher aspect ratio trenches in a silicon substrate, a method described as inductively coupled plasma (ICP) Bosch deep-RIE (DRIE) is often employed. Unlike in traditional RIE, the means by which the ions are generated in this process is separate from the means by which they are given kinetic energy, and the directional etch is in fact not produced by strong ion bombardment at all [7]. Driven inductively, the plasmas have relatively low energies, although high densities and low pressures [3].

The process of Bosch-etching involves alternating between two phases – sequential etching and depositing – that are each carried out for a few seconds before the other's gas is let into the reaction chamber [3, 7]. The etching phase, done with a plasma made from SF₆, is actually isotropic. The deposition phase is where the surfaces of the wafers are covered with a polymer – a teflon-like substance formed in the C₄F₈ plasma. The ions in the SF₆ plasma, traveling perpendicular to the wafers, etch the polymer on their horizontal surfaces, including at the bottoms of their trenches. Once sections of the passivating layer are cleared away, the exposed substrate material proceeds to react with the fluorine neutrals in the plasma. The Bosch process is shown schematically in Figure 2.2.

While this type of DRIE produces trenches with relatively vertical sidewalls, the alternating isotropic etches and sidewall passivation lead to scalloping of the walls, and, if the amount of etching and passivation are not perfectly balanced (i.e. the durations of these phases and the energies imparted to their plasmas are not optimized), the sidewalls will not be perfectly straight and normal to their substrates. Another disadvantage of this process is that the depths of the trenches etched may not be uniform over a wafer and in some cases the required depths may not be reached at all. The etch rate is limited by the rate of diffusion of the reactive species to the substrate material, and decreases with increasing aspect ratio of the trenches. Thus trenches of different widths will etch at different rates. Also, depending on where the trenches are, relative to each other, microloading can occur – where a wide trench locally decreases the availability of the etching species at the expense of any narrow trenches beside it [3]. Unfortunately, the optimal process parameters are specific to each mask design and required depth [7].

2.2 Micropumps

Micropumps have a variety of current and potential applications as components of MEMS, as much as their larger counterparts have a variety of applications in traditional systems. The ability to move small quantities of fluids through arrangements of microchannels can be useful in everything from dissipating heat from microchips, to transporting chemical and biological samples and analytical agents in lab-on-a-chip devices, to delivering controlled amounts of therapeutic agents to specific portions of the body (i.e. engineered

macromolecules into tumors or the bloodstream, or insulin within diabetics). Micropumps can also find use in providing vacuums in analysis systems on lightweight spacecraft, or even propelling such spacecraft. Besides being portable and implantable, lightweight and disposable, systems including micropumps can reduce the quantities of samples and reagents required for chemical and biological analyses, as well as allow these analyses to be performed more quickly and with less manual intervention [8].

The demands placed on micropump designs vary from application to application, as it does in the macroscale. Cooling microelectronics, for example, requires high flow rates and thus high pressures for pressure-driven flows. Conversely, micropumps used for dispensing therapeutic agents into the body generally do not need to dispense large quantities of them (diabetics tend to require less than 1mL of insulin a day), and thus do not need to produce high flow rates. They may, however, be required to work against high back pressures, as those encountered in the body can be as much as 25kPa [8].

At present, micropumps are somewhat limited in the pressures and flow rates they can produce, and are often too large (implanted insulin delivery systems tend to be over 50cm³ in size [8]), require too much power, are not reliable or biocompatible, or cannot be machined in bulk and are very expensive to manufacture. Thus micropumps suitable for some of the applications mentioned above are still not widely available.

In the last few decades many different types of micropumps – ranging from scaled-down versions of regular-sized pumps to those that rely on properties of fluids that only become significant in the microscale – have been designed, manufactured, and tested. They can generally be categorized the same way as their larger counterparts, according to the means by which they produce fluid flow and pressure [8]: dynamic micropumps continuously add energy to the working fluid in a way that either increases its momentum (as in centrifugal pumps), or its pressure directly (as in electrohydrodynamic and electroosmotic pumps); displacement micropumps exert pressure forces on the working fluid through moving boundaries. Some of the more common examples of these two types are outlined below.

Centrifugal pumps themselves, although the most common example of dynamic pumps, have only been miniaturized to a limited extent, as they tend to be ineffective at low Reynolds numbers [8]. Dynamic micropumps that employ electromagnetic fields to move fluids, on the other hand, such as electrohydrodynamic, magnetohydrodynamic, and electroosmotic pumps, only become efficient in the microscale. All three depend on the movement of ions in their fluids to drag the bulk of their fluids down their respective channels. In electrohydrodynamic pumps, the ions in dielectric fluids are moved with electrostatic forces directly; in magnetohydrodynamic pumps, the ions are forced down channels between pairs of north and south magnetic poles, and positive and negative electrodes, set perpendicularly to each other. Electroosmotic pumps use the fact that solids tend to develop a surface charge when in contact with liquids, and that counter ions in the liquids accumulate in the vicinity of the charged walls of microchannels. Externally applied electric fields cause the motion of the

counter ions down the channels. A final example of dynamic micropumps are acoustic streaming or ultrasonic pumps, that induce net fluid flow by propagating waves through membranes in contact with their fluids.

Rotary micropumps are an example of displacement pumps – the few that have been researched are mostly microgear pumps [8]. Minimizing the gaps in these systems where backflow can occur is challenging, and they are best for use with higher-viscosity liquids. Aperiodic displacement micropumps, like other displacement pumps, exert pressures on their working fluids with moving surfaces, but the movement of these surfaces is generally in one direction for a finite amount of time. Thus they are useful for moving finite volumes of fluids. Boundaries between different fluids often replace traditional moving surfaces. Sometimes these pumps are driven pneumatically, with valved pressure sources such as reservoirs of compressed gases, or with phase changes (by locally boiling liquids), or through electrowetting, where electrical control of interfacial tension moves the interfaces in the required direction [8].

The most common example of displacement micropumps, and indeed, micropumps in general, are reciprocating displacement pumps in which the surfaces that exert pressures on the working fluids, moving periodically, are diaphragms [8]. Sealed piston structures have generally not been used in micropumps. Instead, the pump chambers are usually bound on one side by deformable plates with fixed edges, as shown in Figure 2.3. An actuator acts on the diaphragm to alternately increase and decrease the chamber volume, such that fluid is drawn into the chamber during expansion and forced out during contraction. Often two passive valves, one at the inlet, oriented to favour flow into the pump chamber, and one at the outlet, oriented to favour flow out of the chamber, rectify the periodic fluid motion to produce net, if oscillatory, flow. Sometimes a number of actuators and diaphragms are positioned along a channel, without valves, to act as a peristaltic pump.

Several types of actuators have been reported as being used to drive reciprocating displacement micropumps. Piezoelectric disks are a typical example. Used laterally, with one face attached to the pump diaphragm, or axially, with one face attached to the diaphragm and the other constrained by a rigid support, they are polarized in the axial direction with the application of an axial electric field. In the lateral case, the diaphragm bows either into or away from the pump chamber to balance the lateral stresses in the disk. In the axial case, the axial strain induced in the disk expands and contracts the chamber. Although they offer a relatively small stroke, piezoelectric actuators have a short mechanical response time, and thus can be operated at high frequencies [8].

Thermopneumatic actuators are also often used to drive reciprocating displacement micropumps. Their driver chambers, on the other side of their diaphragms as their working fluids, are filled with a secondary fluid (usually air) that is heated with resistive elements. When their secondary fluids expand, they exert pressure on the pump diaphragms, discharging the working fluids out the pump outlets. Intake occurs when the heating elements are turned off. Although thermopneumatic pumps (often with low-modulus diaphragms) can achieve relatively large strokes, they tend to operate best at low frequencies, as their

response is limited by the rate of heat transfer into and out of the driving fluid. They can be made with standard micromachining processes, however, and be operated at low voltages [8].

Finally, while some work has been done with using electrostatic actuators to drive reciprocating displacement micropumps, so far the focus of this work has been on using parallel-plate arrangements, like that shown in Figure 2.4 [8]. With one plate electrode mounted on the pump diaphragm, and the other on a rigid support opposite it, a voltage difference between them creates an attractive force between them, and the one on the diaphragm moves towards the other. The working fluid is discharged from the pump chamber when the voltage difference between the electrodes is removed, and the elasticity of the diaphragm restores it to its starting position. Since the starting distance between the electrodes is necessarily small, and they can only travel a finite distance before they come into contact with each other, parallel-plate actuators tend to provide a relatively short stroke. Dielectric coatings are used to prevent shorting between contacting electrodes.

2.3 Comb Drives

Comb drives are another type of electrostatic actuator and are becoming common in MEMS. The processes involved in their manufacture are also becoming well established. Usually machined from silicon, as shown in Figure 2.5 they are comprised of arrays of parallel plates arranged into opposing comb pairs, where one comb in each pair is simply fixed to the substrate (and is referred to as the fixed comb), and the other is fixed to the substrate through a spring structure (and is referred to as the movable comb). When a voltage difference is applied between the fixed and movable combs the electrostatic forces generated between them attract the movable combs towards the fixed combs. Because their plates (or teeth) are staggered, such that each movable tooth is laterally equidistant from two fixed teeth, the net electrostatic force on each movable tooth pulls it in between the fixed teeth – *parallel* to their orientation. When the voltage difference is removed the springs restore the movable combs to their original positions.

Because the magnitudes of the electrostatic forces acting on the movable combs vary directly with the charging and discharging of the comb pairs, comb drives are capable of almost immediate electromechanical responses. Since their movable teeth travel parallel to their fixed teeth, the displacement of their movable combs is not limited by the small gap between them and the fixed teeth, and, since comb structures allow a large number of electrode surfaces to be arranged into a compact area, lower voltage differences need to be applied between them to produce high electrostatic forces. Also, as will be seen below, the nature of the electrostatic forces is such that they tend to remain constant over most of the displacement of the movable combs, making the output of the actuators simple to predict.

Comb drives have applications in numerous microsystems that require reciprocating motions imparted to them, and in even more that include further mechanisms to convert reciprocating motions into other forms of work. One example is a microconveyer system [9] that moves microcontainers down a channel between comb drives attached to ratchet mechanisms. Other examples include positioning systems that move microstages in two dimensions [6, 10], or micromirrors or microshutters back and forth to either modify the path of a beam of light or block a portion of it [11]. Applications requiring precise positioning are simplified by the easily-controllable output of the comb drives.

A different sort of application comb drives can be used in is actuating sensors [5]. The frequencies of resonant micromechanical structures can be very sensitive to physical or chemical parameters in their environments that affect their mass or stiffness. The electrostatic excitation that comb drives can provide, combined with capacitive sensing, is an attractive arrangement because of its simplicity and compatibility with micromachining technology.

2.3.1 Comb Drive Theory

The opposing fixed and movable comb pairs of a comb drive, being isolated conductors, form capacitors when they are charged. The fixed and movable combs have equal and opposite charges of $+q_e$ and $-q_e$, although their total charge is considered to be q_e . The “capacitance,” C , of a comb drive is the proportionality constant that relates the charge on the combs to the voltage difference, V , between them (as in Equation 2.1), and it is dependant only on the physical geometry of the comb pairs [12].

$$q_e = CV \quad (2.1)$$

The physical geometry of the comb pairs is usually considered to consist of a number of overlapping parallel plates, that are connected in parallel, and assumed to be large enough and close enough together that the electric fields between them are uniform (i.e. the fringing of the electric fields around the corners of the comb teeth can be ignored) [12]. The expression most often used to describe the capacitance between parallel plates is that of Equation 2.2, where ϵ is the permittivity of the medium between the plates (which for comb drives is usually air, thus $\epsilon = 8.85 \times 10^{-12}$ F/m), g is the lateral gap between the plates (shown in Figure 2.6), and A_c is their overlapping area, which, for comb drives, can be expressed in terms of their total number of movable teeth, n (assuming there are enough fixed teeth that they exert electrostatic forces on both sides of each movable tooth), the overlapping length of the teeth, L_t , and the initial offset between the combs, o . z represents the distance the movable combs travel from their original positions.

$$C = \frac{\epsilon A_c}{g} = 2\epsilon n L_t \frac{(z - o)}{g} \quad (2.2)$$

Summing the amount of work done to charge the combs against an increasing voltage difference, and using the relationship between the charge and voltage difference given in Equation 2.1, the energy stored in a capacitor, U , no matter its geometry, can be shown to be described as [12]:

$$U = \frac{1}{2}CV^2. \quad (2.3)$$

The net electrostatic force exerted on the movable combs of a comb drive, F_e , is typically found by considering the change in the electric potential energy between the comb teeth as they slide past each other. Taking the derivative of this energy with respect to the displacement of the movable combs gives Equation 2.4 – the expression for the electrostatic force exerted on the movable combs. Because the derivation of Equation 2.2 assumes the corners of the comb teeth have a negligible effect on the capacitance between them, the capacitance between them is assumed to vary linearly with the area that they overlap, and thus the electrostatic force, not at all.

$$F_e = \frac{\partial U}{\partial z} = \epsilon n L_t \frac{V^2}{g} \quad (2.4)$$

The fact that their electrodes travel parallel to one another is perhaps one of the biggest advantages comb drives have over other types of actuators. As long as a reasonable amount of overlap is maintained between their opposing sets of teeth, the net electrostatic force on their movable combs can be assumed to not vary with their displacements [5, 13, 14]. Since comb drives traditionally provide reciprocating motions parallel to the substrates they are machined on, and, as will be seen below, are able to be machined with very long teeth that lie parallel to their substrates, they can generally provide relatively large displacements while maintaining a “reasonable amount of overlap,” and thus an easily predictable output in terms of actuating force and displacement.

Finally, the static displacement of the movable combs for a particular applied voltage is generally predicted using Hooke’s law [5, 6, 10, 13], where k_z is the spring constant of the arrangement of spring beams that attach the movable combs to the substrate, in the direction opposing the net electrostatic force on the movable combs.

$$z = \frac{F_e}{k_z} \quad (2.5)$$

2.3.2 Typical Fabrication Processes

There are two main methods by which comb drives are typically fabricated. Due to the two-dimensional nature of micromachining, both can produce

relatively long comb teeth oriented parallel to their substrates, as well as long, compliant spring beams.

The older method [5, 10] involves surface micromachining, where the structural components of the comb drives are machined from layers (usually of polysilicon) deposited on the surfaces of silicon wafers. Sacrificial layers of a different material, that are removed at the end of the process, separate portions of the structures from the substrate, while holes etched through these layers allow the structures to be anchored to the substrate. An example of this type of process is shown in Figure 2.7.

Often this process begins with the deposition or growth of passivation layers – a thermally-grown layer of SiO_2 beneath a layer of LPCVD silicon nitride – to isolate the comb drives from their conductive substrates. Around $2\mu\text{m}$ of sacrificial oxide is then deposited as a platform for the comb teeth and springs; etching through it in certain areas allows the comb structures to be anchored to the passivation layers beneath it. A layer of polysilicon, also around $2\mu\text{m}$, is then deposited to act as the structural layer. It is annealed to alleviate mechanical stresses, and patterned with standard photolithography steps. It then undergoes RIE so that the comb teeth and springs have vertical sidewalls, and the entire sacrificial oxide layer beneath it is removed in a solution of hydrofluoric acid.

As SOI wafers have become more common, and advances have been made in high aspect ratio micromachining, a newer method [9, 11] of fabricating comb drives, shown in Figure 2.8, has become popular. It requires only one photolithography step be applied to the tops of the SOI wafers, although an extra masking layer of SiO_2 may be needed depending on the thickness of the device layers. Once patterned, the device layers are etched through with a type of RIE or DRIE step. The exposed insulator layers are then isotropically etched, usually with a hydrofluoric acid solution, such that the SiO_2 beneath the narrow comb teeth and spring beams no longer fixes them to the substrate while that beneath the wider structures at their ends still anchor them to the substrate.

Using SOI wafers for machining comb drives offers a number of advantages. Their device layers can be much thicker than deposited polysilicon layers, which allows for longer free-standing beams, as well as simply thicker comb teeth. As can be seen in Equation 2.4, increasing the dimension of the comb teeth that lies perpendicular to the plane the movable teeth reciprocate in (which in this case is their thickness) can reduce the voltage required for a particular electrostatic force. Also, SCS device layers do not acquire stress through their fabrication, and thus do not need to be annealed during the fabrication of the comb drives. Finally, with carefully-timed etches of the insulator layers, fewer masks (typically only one) are required to pattern comb drives in SOI wafers.



Figure 2.1: Isotropic etch profiles.

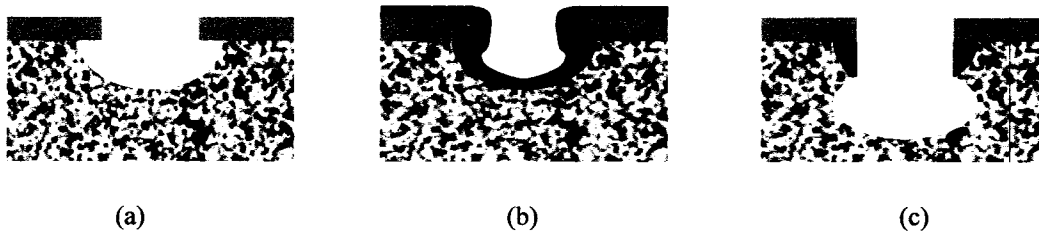


Figure 2.2: The Bosch process – (a) isotropic etching of the substrate, (b) deposition of the passivation layer, (c) anisotropic etching of the passivation layer followed by isotropic etching of the substrate.

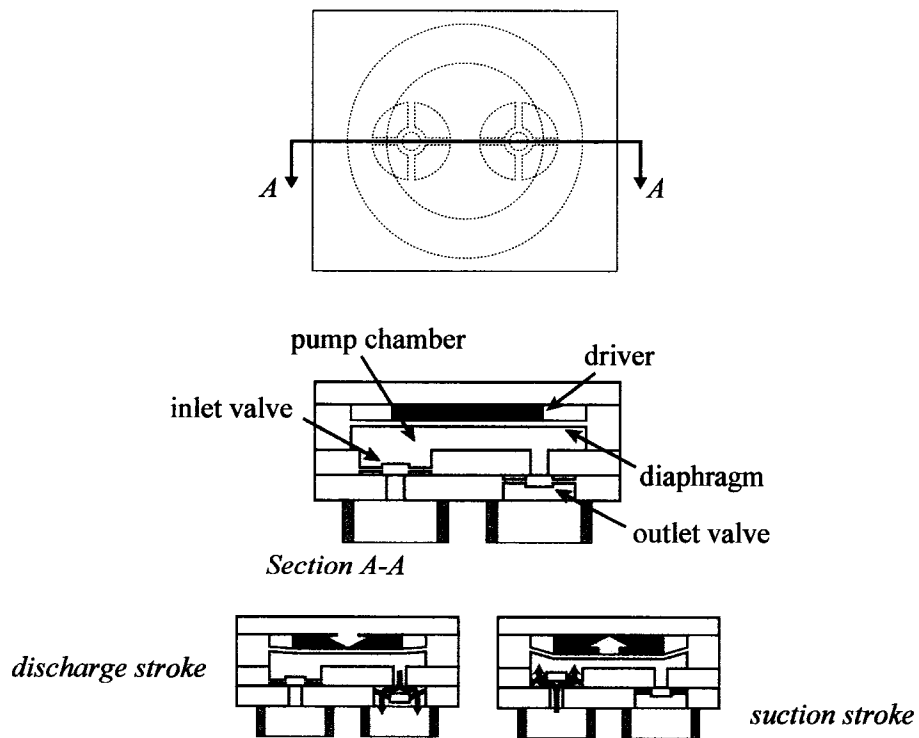


Figure 2.3: A typical reciprocating displacement micropump. Adapted [8].

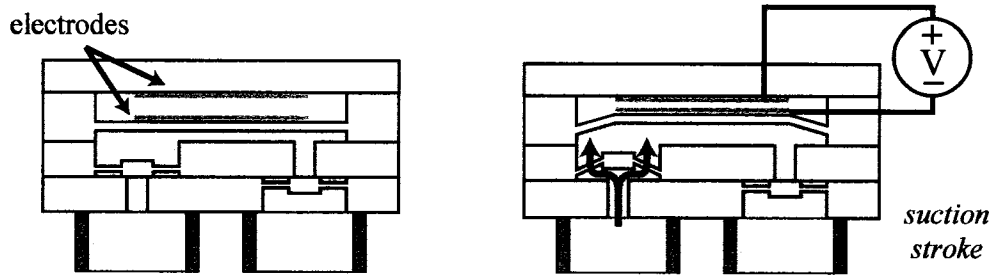


Figure 2.4: A reciprocating displacement micropump with a parallel-plate electrostatic driver. Adapted [8].

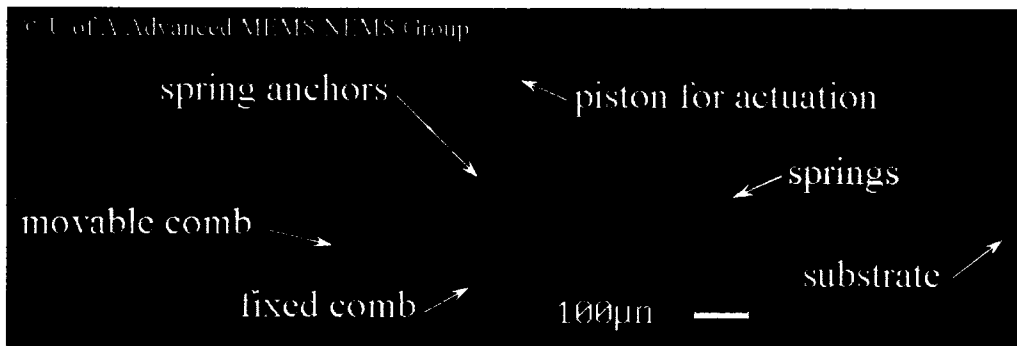


Figure 2.5: A typical comb drive machined from an SOI wafer.

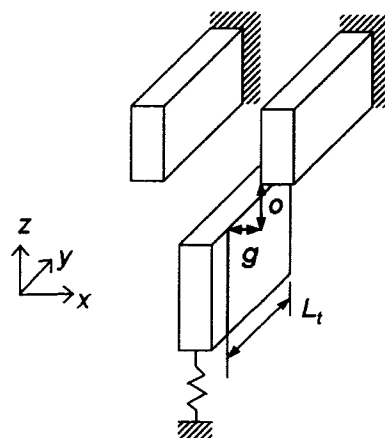


Figure 2.6: Opposing comb teeth and their dimensions that have a large effect on the electrostatic forces generated between them.

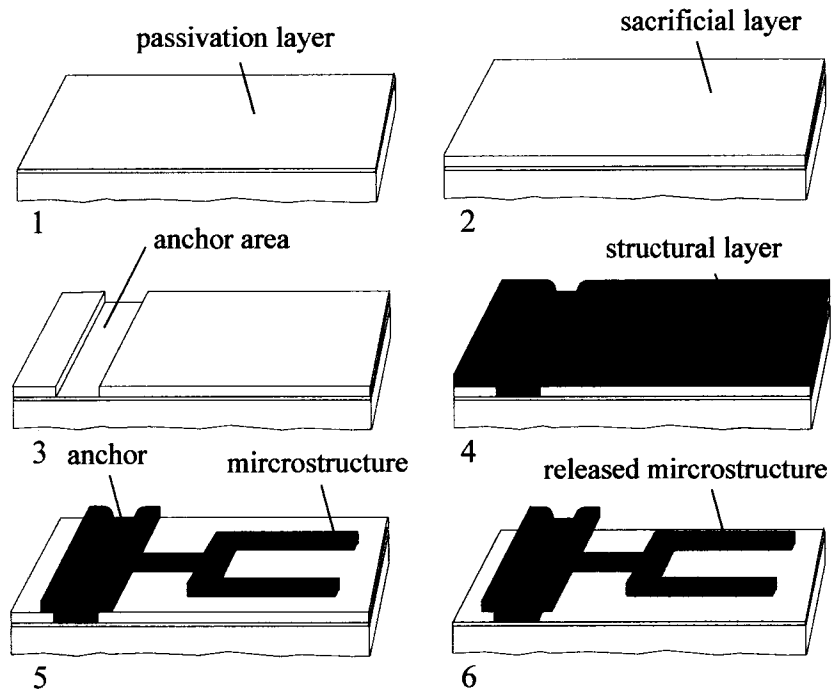


Figure 2.7: An older method for fabricating comb drives. Adapted [15].

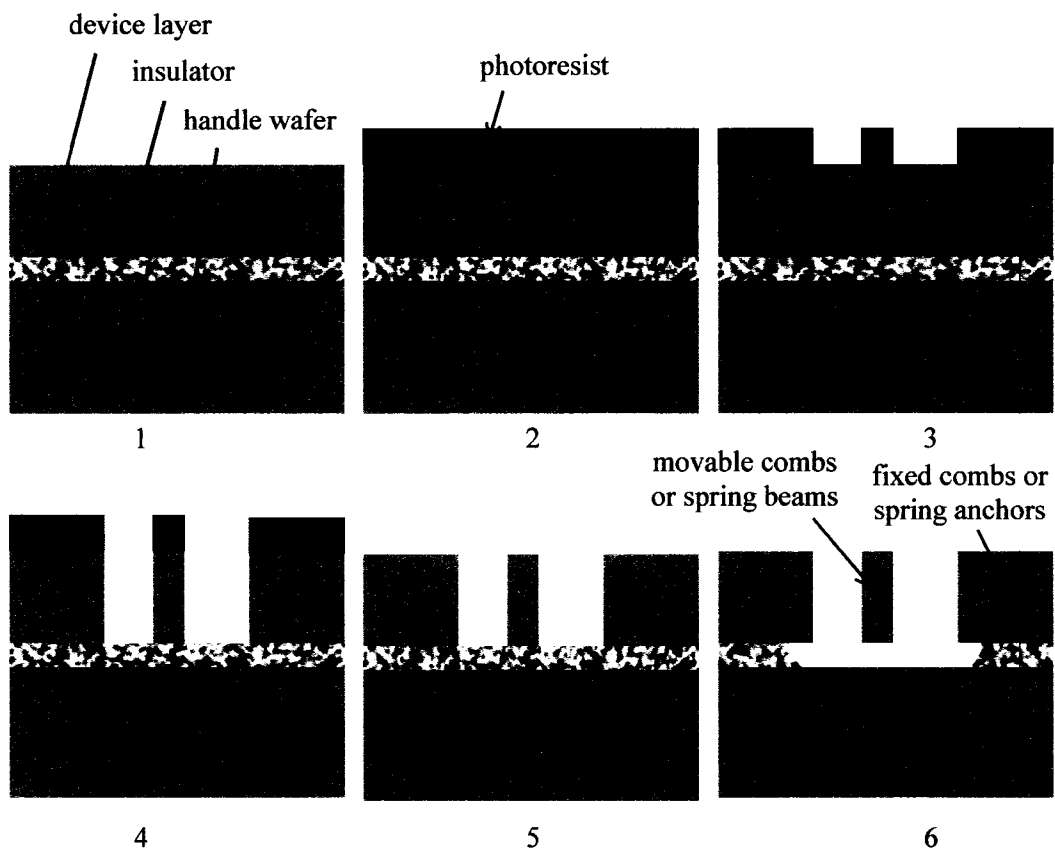


Figure 2.8: A newer method for fabricating comb drives.

Chapter 3: Lateral Comb-Driven Micropump

The following chapter describes an initial attempt at exploring the capabilities of comb drives by using them to actuate micropumps. This attempt was made by designing a style of reciprocating displacement piston-pump that could be connected to a standard lateral comb drive, and then partially fabricating several prototypes of the resulting system to test whether the fabrication process for the chosen comb drive needed any adjustments before extra process steps were added to it to accommodate the pumps.

3.1 Design Considerations

Because comb drives are traditionally machined with all of their comb pairs in the same plane just above their substrate, they tend to provide a reciprocating motion parallel to their substrate (hence the name *lateral* comb drive). Reciprocating displacement micropumps, however, are traditionally machined with thin diaphragms that lie parallel to their substrate, so they require reciprocating motions be provided to them in a direction perpendicular to their substrate. Thus if a standard lateral comb drive is to be used to actuate a reciprocating displacement micropump, the pump must be designed in a non-traditional manner – so that it can accept actuation parallel to its substrate, and, preferably, so that it can be machined using as many of the same techniques traditionally used for lateral comb drives as possible.

3.2 Prototype Design

For the first set of prototypes it was decided that the comb drives should be machined out of SOI wafers – their structures would be etched from the device layers and the movable components of their structures would be freed from the handle wafers by removing parts of the insulator layers in a wet isotropic etch. The particular comb drive design used, shown in Figure 3.1, is meant to have teeth that are as thick as possible in order to maximize the electrostatic force that will be generated between them. Because of process limitations (the difficulty of high aspect ratio etching), this thickness was prescribed as $100\mu\text{m}$, and the corresponding width of each tooth is $5\mu\text{m}$. Although the gap between the teeth of the opposing comb pairs, g , is designed to be $2.5\mu\text{m}$ during actuation, the teeth are not initially engaged. The gap between the teeth of one comb, then, is $10\mu\text{m}$ – which is much easier to machine. All of the holes in the skeleton structures

supporting the movable combs and making up the shaft of the comb drive are also $10\mu\text{m} \times 10\mu\text{m}$ squares, and the width of the lattice parts in the skeleton structures, as well as the other movable components in the comb drive (including the spring beams), is $5\mu\text{m}$.

3.2.1 Piston Design

Since fabricating a membrane perpendicular to a substrate would be exceedingly difficult, as would attaching two substrates together perpendicularly, it was decided that the micropumps should be driven with pistons. As shown in Figure 3.2, the piston is also designed as a skeleton structure, having a large overall width of $50\mu\text{m}$ to maintain its rigidity, while also having no part any wider than $5\mu\text{m}$ (with the same $10\mu\text{m}$ spacing between these parts as the comb it is attached to) so that the oxide beneath it can be etched away as quickly as that beneath the movable comb. To maximize the volume of fluid it could displace with a limited stroke, its overall length was made to be as large as was deemed reasonable: $945\mu\text{m}$.

3.2.2 Valve Design

The valves (on the sides of the pump chambers) are designed in a manner similar to the piston. Although the use of active valves was considered briefly – whether they would be attached, somehow, to the piston or run off the same current as the fixed combs – it was decided that the use of passive valves should be explored first. While their performance may be less predictable than that of active valves (as it depends entirely on the pressure differences produced inside the pumps), they are, in general, simpler to manufacture and employ.

Various flap configurations (many of which would have amounted to vertical cantilevers) were considered, but such components would be similar to membranes, and they would be difficult to manufacture in the orientation required. Eventually the decision was made to try something similar to a ball valve – something that would slide back and forth between stoppers with the flow of the working fluid the same way the pistons would slide back and forth to produce it. As shown in Figure 3.2, stems were added to the “balls” to provide some alignment in their motion, and the balls themselves were given the same skeleton structure as the pistons.

A major disadvantage of the ball design is that special consideration had to be given towards how one would prevent the balls from floating away in the etchant during their release from the handle wafer. Several options were suggested [16], including placing metal straps over the rectangular stoppers to hold the stems in between them or giving the balls springs similar to those of the movable combs. Eventually a solution was settled upon whereby the valves would be etched from the device layer in the shape shown in Figure 3.2, with the balls anchored to the sides of the channels. The anchors would be cut or broken later on in the fabrication process after a glass plate is placed over the pump chambers.

3.2.3 System Design

It was decided that a glass cover would need to be bonded to the top of the device layer each prototype is machined out of to keep the fluid in the pump chambers as well as allow their inner workings to be observed. Consequently, at some point during the fabrication process the tops of the moving components in the device layer would have to be etched down below the tops of the components that are to be fixed to the glass.

The only modification made to the comb drives themselves was the increase in the size of the electrical contacts of the fixed combs to 1mm x 1mm squares. This was done to ease their connection with current-carrying wires. Holes will need to be drilled in the glass above them to allow these connections, and the contacts will be covered with a thin layer of metal to improve conductivity and ease wire bonding.

Thus the main bodies of the comb-driven micropumps will be sandwiched between their substrate and a glass plate, with their movable components being sufficiently narrow relative to their fixed components so that a timed etch of the insulating layer will release one set from the substrate and not the other. The maximum width of any part of a structure that is to be freed from the substrate is approximately 5 μ m, and the minimum distance between these parts is approximately 10 μ m (to ensure that the device layer is indeed etched all the way through in these areas). Conversely, the smallest dimension of anything that is to remain fixed to the substrate is 30 μ m (which is the width of the rectangular valve stoppers).

Finally, the overall length and width of the comb-driven micropump (including its contacts and reservoirs, which are not shown in Figure 3.2) is approximately 4mm and 3.5mm, respectively.

3.3 Prototype Variations

It was decided that five different configurations of comb drives and pistons should be tested with the micropump design to explore different power requirements, maximum displacements and natural frequencies, flow characteristics, and fabrication weaknesses. The prototype shown in Figure 3.2 is the simplest with a single comb pair to one side of the pump chamber. The other four involve single comb pairs on opposite sides of the chamber, two pairs on one side, two pairs on both sides, and two pairs on both sides with a different style of flexure springs. These configurations were named A, B, C, D, and E, respectively, and are compared in Table 3.1.

Configuration E was given a different style of springs in an attempt to increase the maximum allowable displacement of its movable combs. The spring anchors of the other configurations are positioned close to the piston shafts such that they will prevent the pistons from moving any more than 10 μ m in either direction. The anchors for configuration E were thus shifted to the ends of the springs furthest away from the shafts, as shown in Figure 3.3, such that only the

piston hitting the chamber wall (at 15 μm) will limit their displacement. The widths of the spring beams of configuration E were also made to be 10 μm , as opposed to the 5 μm of the other configurations.

The spring constants, natural frequencies, and required voltages listed in Table 3.1 are intended to be initial estimates, and were calculated assuming isotropic properties for single-crystal silicon. They were determined using simple beam and spring theories for piston-motion of the movable combs parallel to the fixed comb teeth. The springs, shown in Figures 3.2 and 3.3, are made up of various arrangements of fixed-fixed beams set to lie parallel to each other. The spring constant, k_{\perp} , of such a beam for the case where one of its ends is displaced in a direction perpendicular to its length is known to be

$$k_{\perp} = \frac{12EI}{L^3}, \quad (3.1)$$

where L is the length of the beam, I is the moment of inertia of the beam's cross-section (with its neutral axis lying perpendicular to the substrate), and E is the modulus of elasticity of the material, taken here as 160GPa – an average value for crystalline silicon, and approximately equal to that of polysilicon. In configuration E, four of these beams are connected in parallel to the piston shaft, thus:

$$k_{zE} = \frac{48EI_E}{L_E^3}. \quad (3.2)$$

In the rest of the configurations, the bar connecting the four beams that make up one side of each spring is assumed to be rigid, thus the two beams in parallel (with length L_1) are in series with the other two beams in parallel (with length L_2). Since two of these assemblies are connected in parallel to the piston shafts of configurations A and B, the spring constant for each of their pistons is:

$$k_{zA,B} = \frac{48EI_{A-D}}{L_1^3 + L_2^3}, \quad (3.3)$$

and, since four of these assemblies are connected in parallel to the piston shafts of configurations C and D, the spring constant for each of their pistons is:

$$k_{zC,D} = \frac{96EI_{A-D}}{L_1^3 + L_2^3}. \quad (3.4)$$

From these equations it is apparent that the spring constant of configuration E is an order of magnitude larger than those of the other two because it does not have a series connection in its beam arrangement, and because the moment of inertia of

its spring beams – influenced heavily by their width – is much larger than that of the other configurations.

Assuming motion where the pistons move back and forth above the substrate, parallel to the fixed comb teeth, and using the typical relation for a natural frequency (the square root of the effective stiffness of the system divided by its effective mass), the natural frequencies of the three different pistons are expected to be:

$$p_{A,B} = \sqrt{\frac{48EI_{A-D}}{(L_1^3 + L_2^3)m_{A,B}}}, \quad (3.5)$$

$$p_{C,D} = \sqrt{\frac{96EI_{A-D}}{(L_1^3 + L_2^3)m_{C,D}}}, \quad (3.6)$$

and

$$p_E = \sqrt{\frac{48EI_E}{L_E^3 m_E}}, \quad (3.7)$$

where the masses, m , of the systems are taken as the volume of the movable combs and skeleton pistons multiplied by a density of 2.3g/cm^3 . Again, the natural frequency corresponding to this type of motion is much higher for configuration E than it is for the other configurations because configuration E has much stiffer springs. For the same reason, the theoretical voltage required to produce $10\mu\text{m}$ of piston displacement is much higher for configuration E – as can be seen by relating Equation 2.4 to Hooke's law.

Here it should be noted that the voltage required to produce such a displacement in configurations C and D is slightly higher than that required for configurations A and B because the double-comb arrangements actually have 120 teeth in total, while the single-comb arrangements have 62. Thus configurations C and D have twice the springs that configurations A and B have, but not quite twice the teeth, so a slightly higher voltage is required to move their pistons the same distance. The voltage required for configuration E to reach full displacement, is, of course, even higher than the voltages required for the other two piston designs, as the piston for configuration E has farther to move and an increasing restoring force to act against.

The flow rates and pressures of the fluids passing through the pump chambers, as well as the electrical power required to produce the flow, will depend largely on the frequency of the ac voltage supplied to the fixed combs of each system. Assuming the same frequency is used for all of the configurations, and that the frequency is low enough that each piston can reach its maximum displacement in every cycle, some general comparisons can be made between the different configurations in terms of the flow rates and pressures they will produce and the amount of electrical power they will require. These three quantities in Table 3.1 are given as multiples of Q, P, and W to illustrate these comparisons.

Besides being a more efficient use of the pump chamber volume, putting two pistons on opposite sides of the pump chamber, as in configurations B and D, should produce flow rates double that of A and C, respectively, as well as double the pressure exerted on the fluid. Actuating twice the number of combs will require twice the current, however, and thus twice the electrical power. Connecting two comb drives and two springs in parallel to each piston shaft, on the other hand, as in configurations C and D, will not affect the flow rate as it is being considered in this analysis – with the same stroke as A and B, the volume of the fluid that will be displaced and the frequency at which it is displaced will remain the same regardless of the arrangement of springs and combs attached to the pistons. The stroke should be completed in a shorter amount of time, however, in configurations C and D, since both the driving and restoring forces – and the difference between them – should be twice that of configurations A and B. Approximately twice the electrical power will be required to charge the surfaces of almost twice the number of comb teeth, but the advantage of the double-comb arrangements is that the pistons they are attached to have a better chance of continuing to reach their maximum stroke as their frequency is increased. Another potential advantage of the double-comb arrangements, depending on the application, is that by producing twice the net force of the single-comb arrangements over their range of actuation, configurations C and D have the potential to produce twice the pressure in their pump chambers as configurations A and B, respectively.

Configuration E, on the other hand, displaces three times the volume of configuration A, and, undergoing the same frequency, will produce three times the flow rate. The comb and spring arrangements attached to each piston of configuration E will also produce larger forces than those of configuration A – not by a constant amount throughout the cycle as in configurations C and D – but larger forces, nonetheless. The maximum net force on the piston of configuration E will be applied to it at the beginning of the cycle when the electrostatic forces are starting to pull the movable combs towards the fixed and there is still a negligible spring resistance. The higher voltage difference and greater number of teeth of configuration E should produce a net force twenty-six times that of configuration A at that point in the cycle. Multiplying this force by two to include both pistons in the pump chamber, the pressure produced by configuration E should be fifty-two times that of configuration A – if only for a brief amount of time. However, the electrical power required to produce this pressure and flow rate is expected to be fourteen times that required by configuration A, as configuration E has four times the number of combs (and thus will require four times the current) and will use approximately 3.6 times the voltage.

Finally, the difficulties involved in fabricating the various configurations are expected to be similar, save that the wider springs and larger spring anchors of configuration E should be less vulnerable to over-etching of the device layers and insulator layers of the SOI wafers being used.

3.4 Mask Design

On the masks the five different configurations are arranged to be 5mm apart (centre to centre, lengthwise) in a column. In order to fit as many as possible on an SOI wafer 100mm in diameter while leaving a reasonable (>4mm) amount of space around its edges open for handling purposes, an array of three rows containing nine, fifteen, and nine of these columns (again, positioned 5mm apart, centre to centre) was created. Because each pump configuration would be spread throughout the wafer, at least some prototypes of each configuration should survive the fabrication process if a particular section of the wafer is damaged over the course of it. Also, while the quality of the individual prototypes may vary from processes that do not affect the wafer uniformly, if each configuration is spread throughout the wafer each will have both high and low quality prototypes, as opposed to one configuration having high and another low.

Three different masks were designed for the fabrication of the entire comb drive-pump assemblies: one containing the shapes of the depressions to be etched in the device layer to keep the moving components of the pumps and combs free from the glass cover, one containing the shapes of the pumps and combs to be etched through the device layer, and one containing the shapes of the metal layers to be left on the electrical contacts. Since the masks were designed for use with positive photoresist, most of the chrome was to be left on the glass wafers, so windows were added to the masks to assist in their use. Alignment marks were also added to assist in aligning the masks with etches patterned by previous masks. The alignment marks are arrangements of squares and crosses located to the sides of the comb-pump arrays and organized in sets of two such that the masks can be used in any order. With their smallest dimension being 5 μ m, it is estimated that an offset of 1 μ m would be noticeable under a microscope.

The shapes for two sets of test structures to be etched out of the device layer were also placed beside each column (in the second mask mentioned above). The etching of the device layer should produce long strips of silicon 3 μ m, 4 μ m, 5 μ m, and 6 μ m wide to be successively carried away as the SiO₂ beneath them is removed. Their absence is meant to indicate that the moveable components of the pumps and comb drives have been freed from the handle wafer.

3.5 Fabrication

It was decided that the initial attempt made at machining the comb drive-pump systems should begin with the typical process steps for lateral comb drives so that the movement of the pistons could be studied before further processing was done to complete the pumps. Thus only one of the masks described above – that which would be used to define the shapes of the systems in the device layers of the SOI wafers – was actually made.

3.5.1 Mask Fabrication

A Heidelberg DWL-200 Laser Pattern Generator with a 50mm lens was used to transfer the mask design from its computer file onto a 125x125x3mm glass plate coated on one side with layers of chromium and photoresist. The exposed photoresist was then developed and parts of the chrome etched away to produce the physical mask, which was subsequently inspected beneath a microscope. After the features were judged to have been transferred clearly, the remaining photoresist was removed with acetone and isopropyl alcohol (IPA), and the mask was placed in a cold (<40°C) piranha cleaning solution (warm, diluted H₂SO₄) for 15min.

3.5.2 Prototype Fabrication

The wafers used in the fabrication of the comb-driven micropump prototypes were standard 100mm-diameter SOI wafers with device layer thicknesses of 100µm and buried oxide thicknesses of 2µm. A detailed account of the fabrication process that was followed is listed below (and shown in Figure 3.4):

- 1.) **Piranha Cleaning** – The wafers were placed in a fresh (>100°C) 3:1 H₂SO₄ and H₂O₂ solution for 15min, rinsed with water, and then spun dry.
- 2.) **Thermal Oxidation** – A 1.1µm layer of SiO₂ was grown on the wafers in a Minibrute oven to shield certain parts of the device layers during etching. The oven was kept at 900°C and the water was boiled at 98°C (to produce a maximum amount of steam).
- 3.) **Deposition of Hexamethyldissilazane (HMDS)** – An automatic YES HMDS dispense oven was used to deposit a film on the wafers that gave the top of their new oxide layers the adhesion properties of silicon.
- 4.) **Application of Photoresist** – Positive photoresist was spun onto the wafers to a thickness of 1.3µm.
- 5.) **Quartering** – The wafers were placed face-down on a clean surface, divided into quarters with a ruler and a diamond pen, and then cleaved along the lines drawn.
- 6.) **Development of Photoresist** – The photoresist on each quarter was exposed to ultraviolet light through a portion of the mask and then etched with a developer.
- 7.) **Pattern Transfer to Oxide** – The outlines of the comb drive-pump systems were wet-etched through the SiO₂ on top of the device layers in a 10:1 buffered oxide etch (BOE) solution (which took approximately 22min).
- 8.) **Attachment to Dummy Wafers** – The back of each quarter was coated in IPA and pressed on to a scrap silicon wafer covered in photoresist.
- 9.) **Deep Reactive Ion Etch** – The outlines of the systems were Bosch-etched through the device layers in an Oxford Plasma Lab 100 ICP RIE.

- 10.) **Oxygen Plasma Cleaning** – The polymer from the Bosch process was removed with a 20min oxygen plasma bombardment.
- 11.) **Structural Release** – The SiO₂ beneath the device layers was wet-etched in a 10:1 BOE solution for 90min to free the moveable components of the systems from their handle wafers.
- 12.) **Detachment from Dummy Wafers** – The quarters and their respective dummy wafers were soaked in IPA and then pulled apart.
- 13.) **Critical Point Drying** – To avoid a receding liquid/vapor boundary causing stiction of the movable system components, the quarters were dried in a controlled temperature and pressure environment [17].

3.6 Fabrication Results

The initial attempt at machining the comb drive-pump systems resulted in the simultaneous over and under-etching of the device layer and insulator layer during the DRIE and Structural Release process steps such that the prototypes varied immensely from what had been designed.

Figure 3.5 shows an example of the outcome of the DRIE step – a top view of one of the prototypes after the outlines of the pumps had been etched through the device layer. The skeleton structure of the movable comb and piston can be seen in some areas; the darker regions indicate where the holes have not been etched all the way through. At the same time, the silicon dioxide on top of the device layer that was meant to shield it during the DRIE step can also be seen to have receded from the edges of the fixed comb and pump chamber and clearly no longer covers the movable comb and piston at all. Figure 3.6 is a closer view of the top of a skeleton structure that lost its protective oxide and had begun to be etched during the DRIE step.

Besides being over-etched on top, the structures were also over-etched on their sides. Figure 3.6 shows the nominal width of the spring beams and lattice parts of the skeleton structures that were meant to be 5 μ m as being closer to 2 μ m, which may be due to the isotropic etching of their protective oxide and the subsequent undercut beneath its masking photoresist. As well, the DRIE step did not provide an etch straight down into the device layer, but one at an angle of approximately 89° to the substrate such that the bottoms of the structures are much thinner than their tops. Figure 3.7 shows the tapered bottom edge of one of the spring beams; Figure 3.8 the resulting thickness of the narrow beams relative to that of the wider structures. It is estimated that the actual cross-sections of the spring beams and lattice parts that were intended to be 5 μ m x 100 μ m rectangles are in fact isosceles triangles with top widths of 2 μ m and depths of 70 μ m, as illustrated in Figure 3.9.

Because of the increased fragility of these parts, many of them broke later on in the fabrication process, and although the wider springs of configuration E were somewhat sturdier, the movable combs they are attached to were not. Figures 3.10 and 3.11 show examples of wider springs that have broken at their

connection points to the piston shafts. In general, it seemed that all of the prototypes were over-etched enough for configuration E to not have an advantage in this fabrication run.

Overall, approximately 75% of the prototypes have broken springs or are missing pistons or entire movable combs. Similarly, all of the test structures that were intended to be successively carried away during the Structural Release step were in fact released during the DRIE step because of the 89° etch.

The Structural Release step further decreased the overall yield of the fabrication process in two ways: by over-etching the insulator layer beneath some of the components that were to remain fixed to the handle wafer (to the point where none of the rectangular valve stoppers remain at all) and by under-etching the insulator layer beneath some of the components that were to be freed from the handle wafer. Figure 3.11 shows some of the oxide still between the teeth of one of the comb pairs. It is suspected that bubbles formed between the teeth during the Structural Release step and prevented the BOE from getting to the oxide [16].

On the whole, then, none of the prototypes turned out as expected. Even if their movable components remained intact as they were freed from the handle wafer their valve stoppers floated away in the BOE. Since the plans for the preliminary testing of the prototypes did not involve fluids and thus valves, however, it was decided that some of the prototypes – about 20% – were suitable for an attempt at electrical actuation.

3.7 Prototype Testing

The preliminary testing of the prototypes involved simply applying voltages to the fixed combs and observing the displacements of the movable combs to see whether they had been freed from the handle wafer and how the addition of the pistons affected their movement. The prototypes were connected to the testing circuit as shown in Figure 3.12, with two probes grounding the handle wafer and movable combs and one or two probes passing currents to the fixed combs. (The fixed combs of the configurations that had two comb pairs per piston – C, D and E – were split in two to allow the piston shafts to pass through them. Thus these configurations required additional probes so that both sides of their combs could be actuated.)

The preliminary testing confirmed that some of the prototypes had indeed been under-etched during the Structural Release process step. The pistons of those that still had oxide visible between their comb teeth, for example, would not move even with mechanical stimulation (where the tip of a probe was used to physically push the pistons). The testing also confirmed that some of the prototypes had been over-etched during this step. In many cases the oxide left beneath the spring anchors was not enough to keep them fixed to the handle wafer when a probe was placed on top of them. Figure 3.13 shows a movable comb that has broken free of its handle wafer, as well as the size contrast between the anchors at the ends of its springs and what remains of the oxide that was meant to hold its anchors to the handle wafer. In order to ground the movable combs

without breaking their spring anchors free, a thin wire that extended past the probe tip was attached to it and used to make the connections with the spring anchors instead. This procedure proved to be reasonably successful, as the wire would bend before enough pressure was applied to the anchors to break them free of the handle wafer.

In attempting to actuate the movable combs electrically, just enough current was delivered to the fixed combs to charge their surfaces. The voltages required to displace the movable combs, however, varied from those predicted considerably – ranging from as little as 14V to as much as 175V, with hardly any distinction between the different configurations at all. While for the most part the movable combs were drawn towards the fixed combs as expected (and as shown in Figure 3.14), it was noticed during testing that some were coming in asymmetrically and many were not returning to their rest positions. Furthermore, their displacements tended to occur very suddenly – there did not seem to be a range of voltages over which the magnitudes of their displacements could be varied. These observations suggest that the springs were over-etched to the point where they could not supply a proper restoring force, and the voltages required to displace the movable combs were in fact determined by the force needed to overcome any sticking or friction between them and the substrate (and it is wondered whether perhaps configuration E is more prone to this friction, having only a single spring at the end of its piston shaft).

Although a method of probing the prototypes had been found that did not break the spring anchors free from the handle wafer, the springs themselves continued to fracture as the movable combs were actuated. Because a way could not be found to completely prevent the testing from being destructive, and the prototypes being tested were not accurate representations of the original designs in any case (even the thickness of the comb teeth was likely not what was expected, hence neither were the electrostatic forces on the movable combs), it was decided that the mask and fabrication process should be improved before further electrical actuation was attempted.

3.8 Design and Process Recommendations

Several ideas were considered as to how to adjust the designs and the fabrication process to increase the yield and improve the quality of the prototypes. Among them are:

- o increasing the size of the holes in the skeleton structures and/or reducing the size of the pump chambers and the areas left open around the prototypes (there is no need for them to be so large, and decreasing their size may decrease the microloading on the skeleton structures) – to better the chance of all of the holes being etched all the way through the device layers
- o increasing the size of the spring anchors to better their chance of remaining fixed to the handle wafers

- o increasing the thickness of the masking oxide on top of the device layers so that it will not be etched through so quickly during the DRIE step and/or decreasing the bias voltage and/or time of the deposition cycles during the DRIE step, as it is in these cycles that the oxide is etched by energetic ions [7]
- o reactive ion etching the masking oxide (rather than wet-etching it isotropically) so that the thin structures in the systems will retain their designed widths
- o taking the wafers out of the BOE periodically during the Structural Release step and rinsing the bubbles from between their closely-packed structures so that the etchant can get to the insulator layer [16]

3.9 Finite Element Simulations

While it is impossible to confirm the required voltages calculated for Table 3.1 with the prototypes of the first fabrication run, it is similarly impossible to confirm the natural frequencies. Any kind of sweeping in the ranges expected would certainly be destructive to the prototypes and, again, because the spring stiffnesses are not what they were meant to be, the results of such testing would be inaccurate in any case. It is hoped that operating the movable combs at resonance will decrease the force (and thus the voltage) required to move them, however, so it is of interest to find their natural frequencies to see whether or not this would be feasible. It was decided that confirmation should be attempted with finite element models, then, as they tend to be sturdier than physical ones.

3.9.1 Building the Models

Three models of movable combs (configurations A and B have the same style of movable comb, as do configurations C and D) were built in IntelliSuite™'s 3D Builder™ module. They include every detail of the original designs in a 100µm silicon layer and have a 2µm insulator layer beneath their spring anchors for constraining purposes. The full structure of the simplest model – that of configurations A and B – is shown in Figure 3.15.

Once built, the models were exported to one of IntelliSuite's analysis modules to refine their meshes and define their material properties. As an initial estimate, both the device and insulator layers were assumed to have the properties of polysilicon. The numerical values used to represent these properties were those supplied by the IntelliSuite database: 2.3g/cm³ for the density of the material, 160GPa for the modulus of elasticity, and 0.42 for the Poisson's ratio. When complete, the models were exported from the module in a format readable by ANSYS®.

3.9.2 Analysing the Models

The simulations conducted with the models built in the IntelliSuite modules were run in ANSYS. The elements of the models transferred from one program to the other well in terms of their geometries, however, their material properties required some adjustment after the transfer. It is suspected that the two programs interpret units differently – the density of the polysilicon, for instance, did not remain constant relative to its modulus of elasticity. Also, it would seem that ANSYS requires a shear modulus and the IntelliSuite modules do not. From the modulus of elasticity and the Poisson's ratio a shear modulus of 56.338GPa was calculated and added to the models.

Once these values were corrected for each of the models, the nodes at the bottom of their insulator layers were constrained to have zero displacement in all directions, and the settings of the simulations were tuned towards modal analyses. For the first two models (that of configurations A and B, and C and D), the expected mode shape (of oscillating motion parallel to the insulator layer) was found to coincide with their first natural frequencies of 3186Hz and 3530Hz, respectively. The first mode shape of the third model (that of configuration E), however, involves its piston moving perpendicular to the insulator layer as the springs twist around their axes, as shown in Figure 3.16. The second natural frequency of the third model, at 10778Hz, was found to coincide with the expected mode shape.

All of the natural frequencies found with the finite element models were thus below those calculated for Table 3.1, perhaps because the calculations assumed that the skeleton structures of the pistons and piston shafts are perfectly rigid (which would increase the overall stiffnesses of the movable combs) and neglected the masses of the springs. Nonetheless, the frequencies obtained from the models deviate from those in Table 3.1 by less than 10%, which confirms that both sets of values are good initial estimates.

3.10 Conclusions

In an effort to explore the capabilities of comb drives, a preliminary investigation was conducted into the possibility of using them to actuate micropumps. This was done by taking a typical lateral comb drive design and coming up with a style of reciprocating displacement piston-pump that could be paired with it. Five variations of the resulting system – each with different advantages in terms of stroke, pressure and flow rate, power consumption, and fabrication difficulty – were then partially machined (such that they would have their internal components etched from the device layers of SOI wafers, with those components that are meant to be movable freed from the handle wafers with a partial etch of the insulator layers), following a standard process for lateral comb drives.

The prototypes made in the first fabrication run turned out to be very poor representations of the components that were designed. Both the device and insulator layers of the SOI wafers were over and under etched such that some of the components that were meant to be movable remained fixed to the handle wafers, and the anchors of those components broke free of the handle wafers. The narrow structures (such as the spring beams) turned out to be much narrower than they were designed to be, to the point where even their thicknesses were reduced. This made the structures overly fragile, so that many of them broke in subsequent fabrication steps or when attempts were made to actuate the comb drives electrically. Even if they did not break themselves, the springs were observed to be too weak to be providing proper restoring forces to the pistons.

Although some success was had with finite element models (in confirming the natural frequencies predicted, and discovering some potential problems with one of the design variations), a number of issues with the current design and fabrication process will need to be resolved before much of a judgment can be made on whether pairing micropumps with lateral comb drives in the manner discussed here will, in fact, extend the capabilities of micropumps.

3.11 Next Steps

While the fabrication and design recommendations made above, if followed, may increase the yield of the prototypes that truly represent the systems designed, there are a number of issues with the concept of a piston-driven micropump that have yet to be addressed in this study – the main one being leakage. For fabrication purposes, there must be a certain amount of space between the piston and its surrounding chamber walls. The piston of the current design has 10 μm between it and its side walls to ensure that the DRIE process step separates the two, 2 μm between it and the bottoms of its pump chamber as prescribed by the thickness of the insulator layer, and at least a few microns between it and the glass cover so that the two will not be bonded together. Thus there is certainly an opportunity for the fluid to flow past the piston and decrease the pressures and flow rates produced by the pump, if not hinder the workings of the comb drive itself.

While it may be possible to seal the space around the piston with another, more viscous fluid than that going through the pump chamber, if lateral comb drives are to be used to actuate micropumps the micropumps should be designed to use aspect ratio limitations to their advantage and the reciprocating motions of the comb drives should be converted into something more efficient. A fluid should be dragged along with the flat side of a necessarily thin micromachine component, for example, rather than be pushed with the edge of it. One such micropump has been reported [18] where two comb drives, positioned perpendicularly to one another on their substrate (as shown in Figure 3.17), are used to turn a series of gears that mesh with the side of a disk that has a spiral groove etched into the bottom of it. The fluid trapped between the groove and the

substrate is viscously dragged between inlet and outlet holes etched through the back of the substrate as the disk is spun.

There is also another option for actuating micropumps with comb drives, which may at least prevent leakage of the working fluid into the areas between the comb drive components. Over the course of the study on lateral comb drives, some literature was found [19 – 30] that discusses the fabrication and use of a different type of comb drive – one that could provide a reciprocating motion perpendicular to its substrate. *Vertical* comb drives – whose teeth are offset vertically as shown in Figure 3.18 – operate in the same manner as lateral comb drives, in that their movable combs are drawn towards their fixed when a voltage difference is applied between them, and springs restore the movable combs to their original positions when the voltage difference is removed. The motion of vertical comb drives is in another direction than that of lateral comb drives simply because their comb pairs are offset in another direction.

Though a relatively new technology, vertical comb drives have thus far found much use as mechanisms by which to lift and tilt (in one or two axes) micromirrors and microlenses at high speeds. Acting as optical switches or scanners, like their lateral counterparts they can obstruct a beam of light coming from optical fibres, and can steer a beam of light in a one- or two-dimensional space. This can be useful in laser printing, barcode reading, optical data storage, laser machining, and laser projection display – as well as in optical communications networks. Usually vertical comb drives have spring beams that are designed to twist about their axes, and have their comb pairs positioned on either side of a mirror so that they may apply a force to one edge or the other as voltage differences are applied between the combs of one pair at a time.

If a vertical comb drive could be connected to the diaphragm of a standard reciprocating displacement micropump, the diaphragm would separate the fluid in the pump chamber from the actuation mechanisms of the comb drive completely. It may also be possible to machine the comb drive such that a lower voltage is required to produce the electrostatic forces within it. As shown in Equation 2.4, the dimension of the comb teeth that is a factor in the magnitude of the net electrostatic force between them is perpendicular to the motion of the movable comb. Thus a lateral comb drive requires teeth with large dimensions perpendicular to its substrate, while a vertical comb drive requires teeth with large dimensions parallel to its substrate – which is generally much simpler to machine. For the next stage in exploring the potential of connecting comb drives to micropumps, then, it was decided that the capabilities of vertical comb drives should be explored.

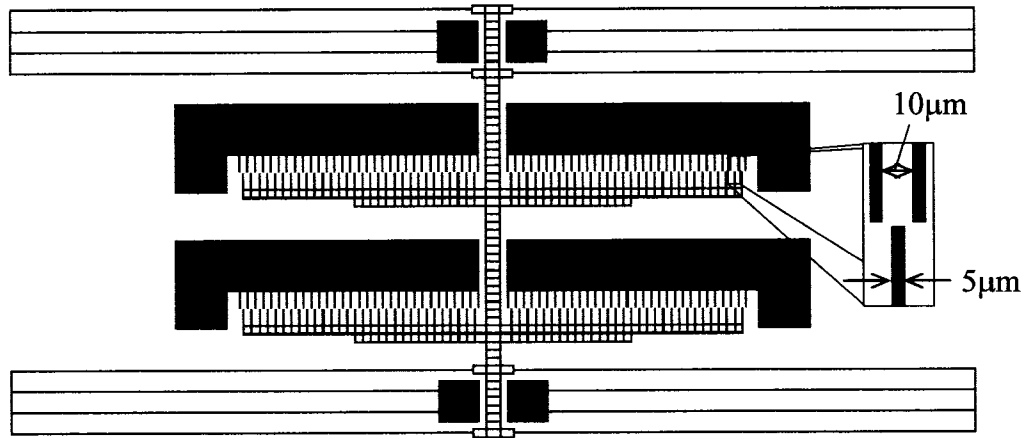


Figure 3.1: A top view of the comb drive used for pairing with a new type of reciprocating displacement micropump. Model drawn in IntelliSuite™'s IntelliMask™ module.

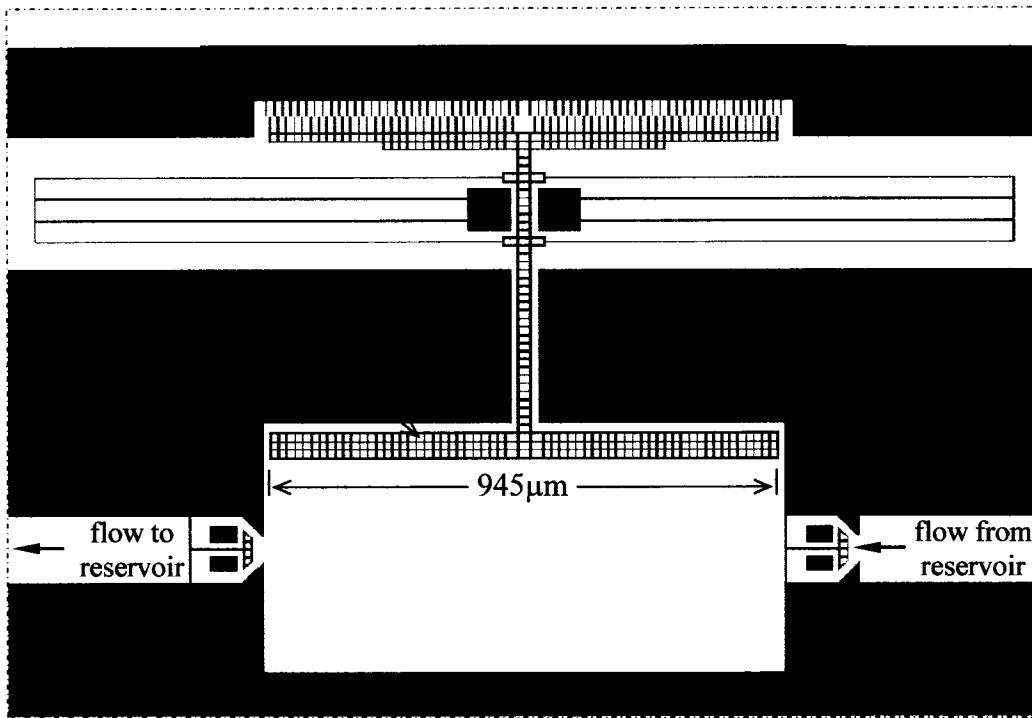


Figure 3.2: A top view of the main components of the comb-driven micropump. The dark regions indicate the parts of the device layer of the SOI wafer that will remain after it has been etched through. Model drawn in IntelliSuite™'s IntelliMask™ module.

Table 3.1: A comparison of prototype design characteristics.

Design	A	B	C	D	E
Maximum Displacement	10 μ m				15 μ m
Spring Stiffness	6.89N/m		13.8N/m		116N/m
Natural Frequency	3434Hz		3887Hz		11354Hz
Voltage for 10 μ m Displacement	56V		57V		165V
Voltage for Maximum Displacement	56V		57V		202V
Flow Rate	Q	2Q	Q	2Q	3Q
Maximum Pressure	P	2P	2P	4P	52P
Electrical Power Required	W	2W	2W	4W	14W
Relative Fabrication Difficulty	similar				less

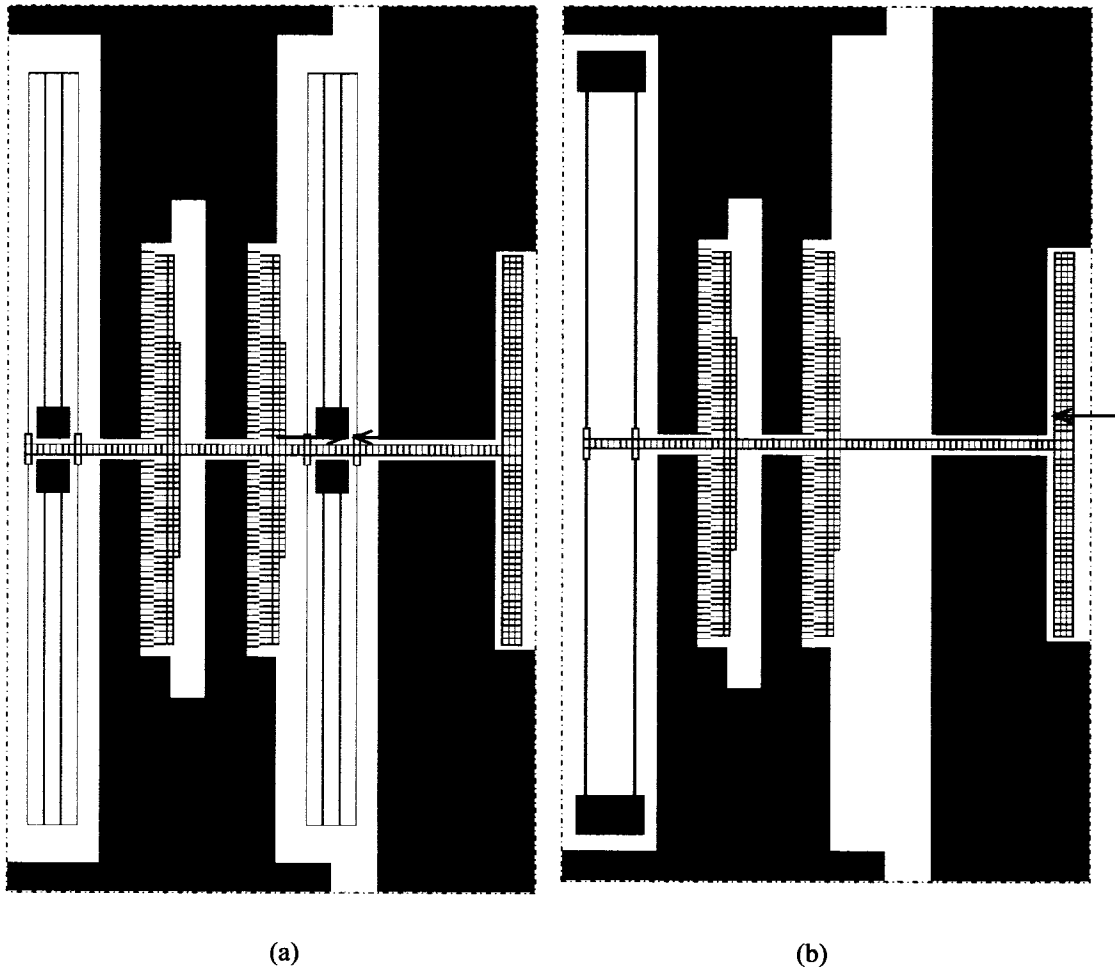


Figure 3.3: The arrangement of the springs and combs for configurations C and D (a); and that for configuration E (b). Models drawn in IntelliSuite™'s IntelliMask™ module.

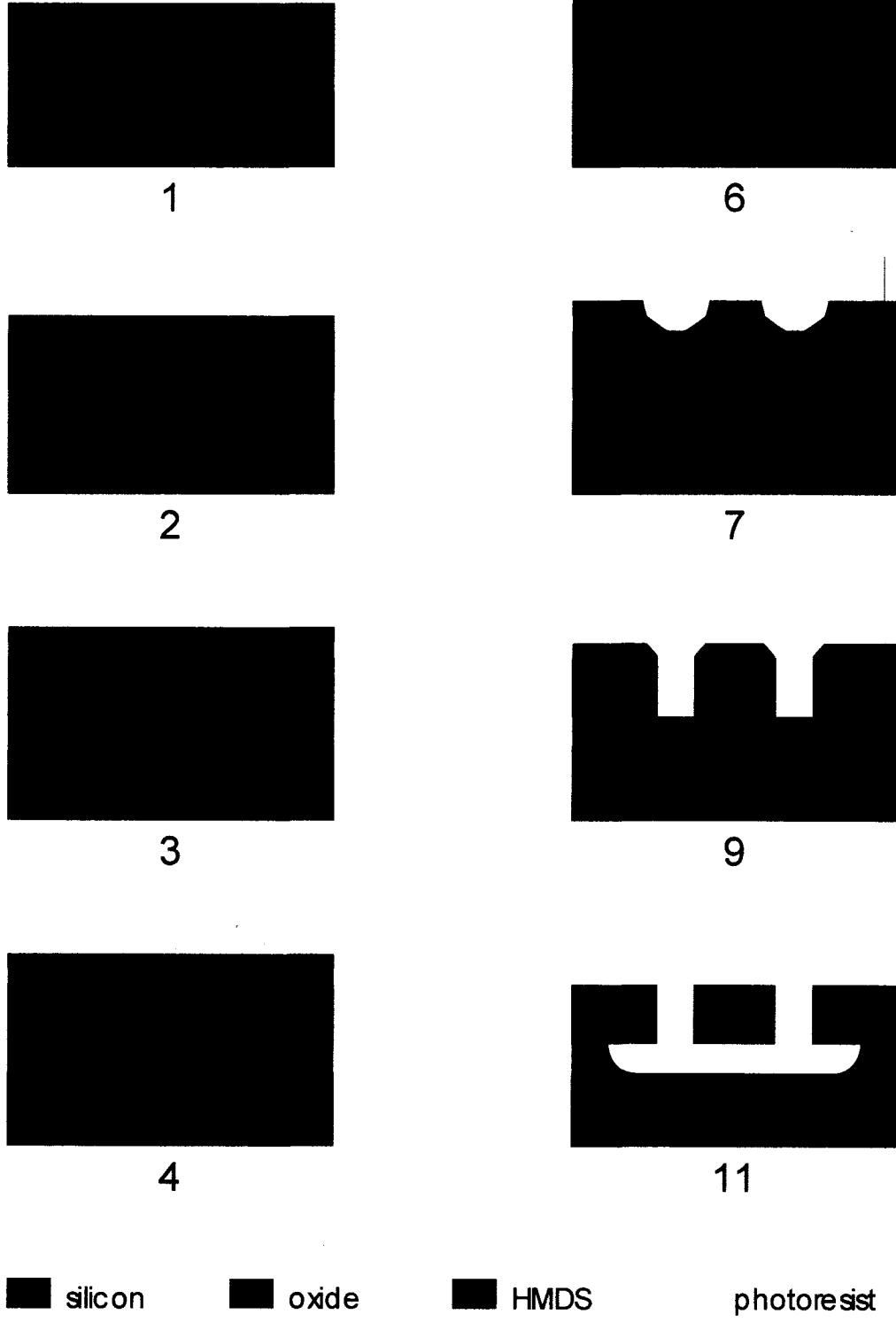


Figure 3.4: The process followed in the fabrication of the lateral comb-driven prototypes.



Figure 3.5: A top view of one of the prototypes on completion of the DRIE process step.



Figure 3.6: The tops of the lattice structures that lost their masking oxide and were etched during the DRIE process step.

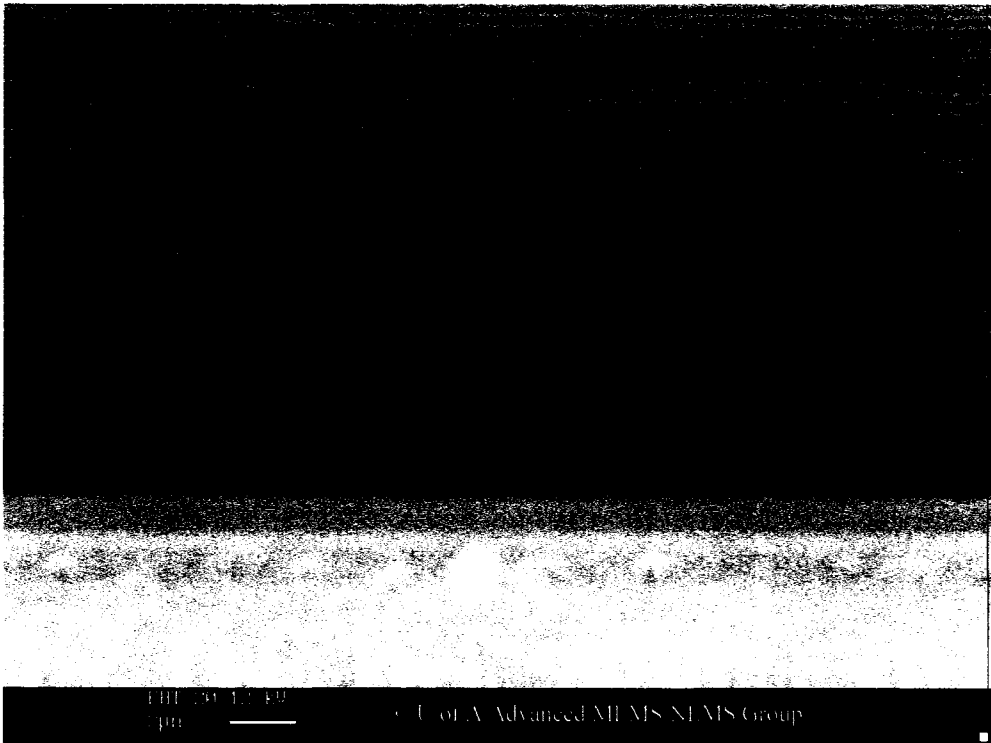


Figure 3.7: The tapered bottom edge of a spring.

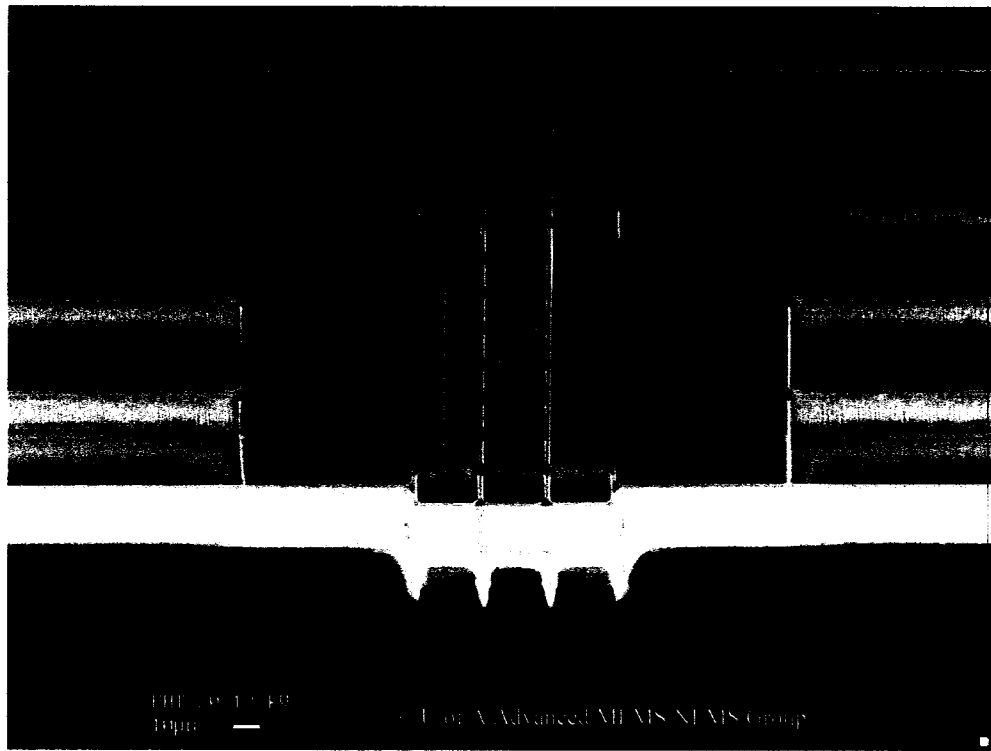


Figure 3.8: A comparison of the thickness of the spring beams and lattice structures relative to that of the wider structures.

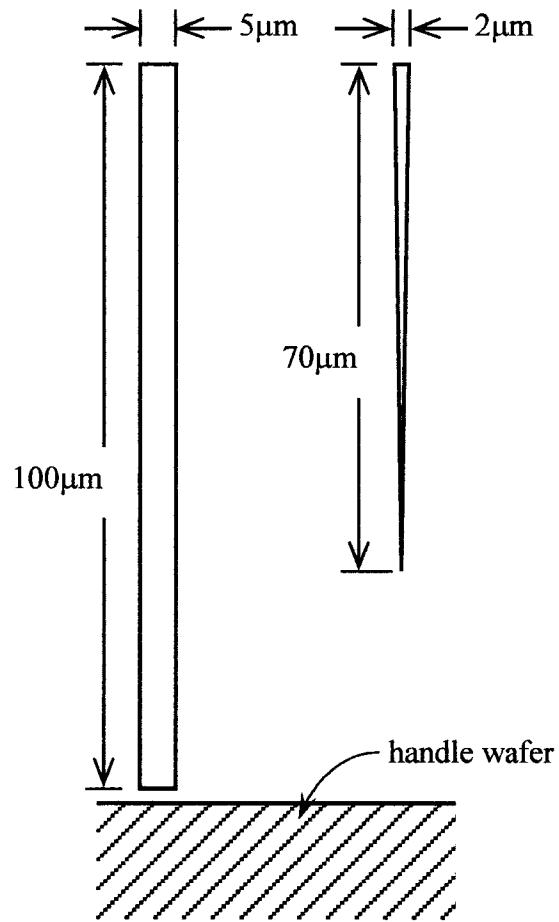


Figure 3.9: A comparison between the designed cross-section of the spring beams (left) and the estimated actual cross-sections of the prototype beams (right).

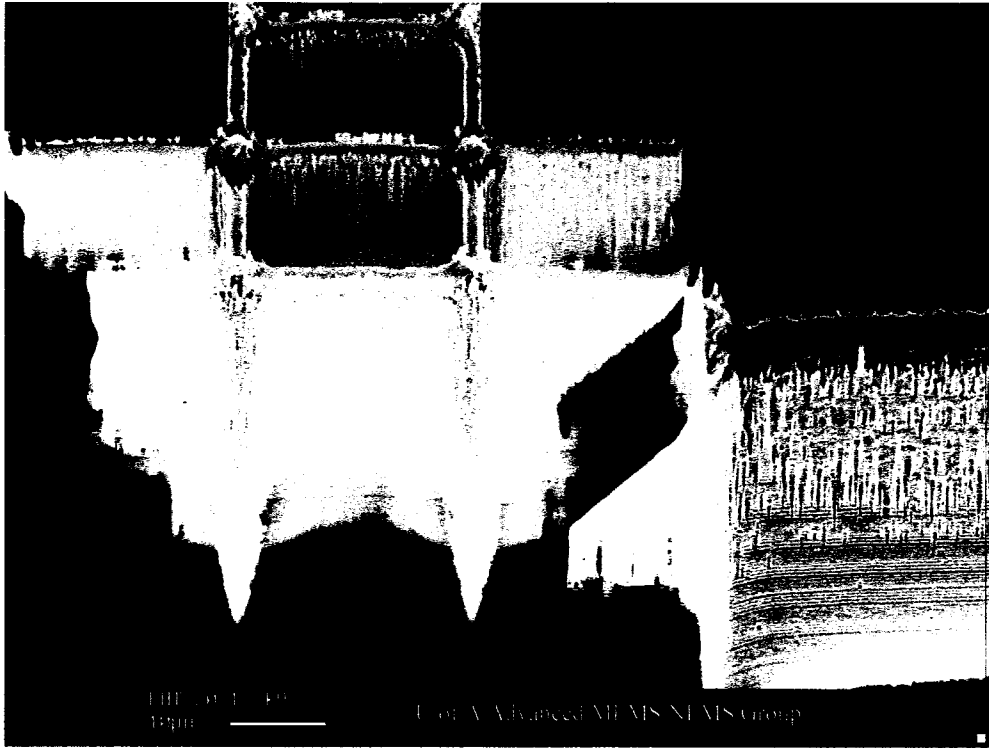


Figure 3.10: A spring beam (of configuration E) broken free of its piston shaft.



Figure 3.11: A spring beam (of configuration E) that has broken from the piston shaft, and comb pairs with oxide remaining between their teeth.

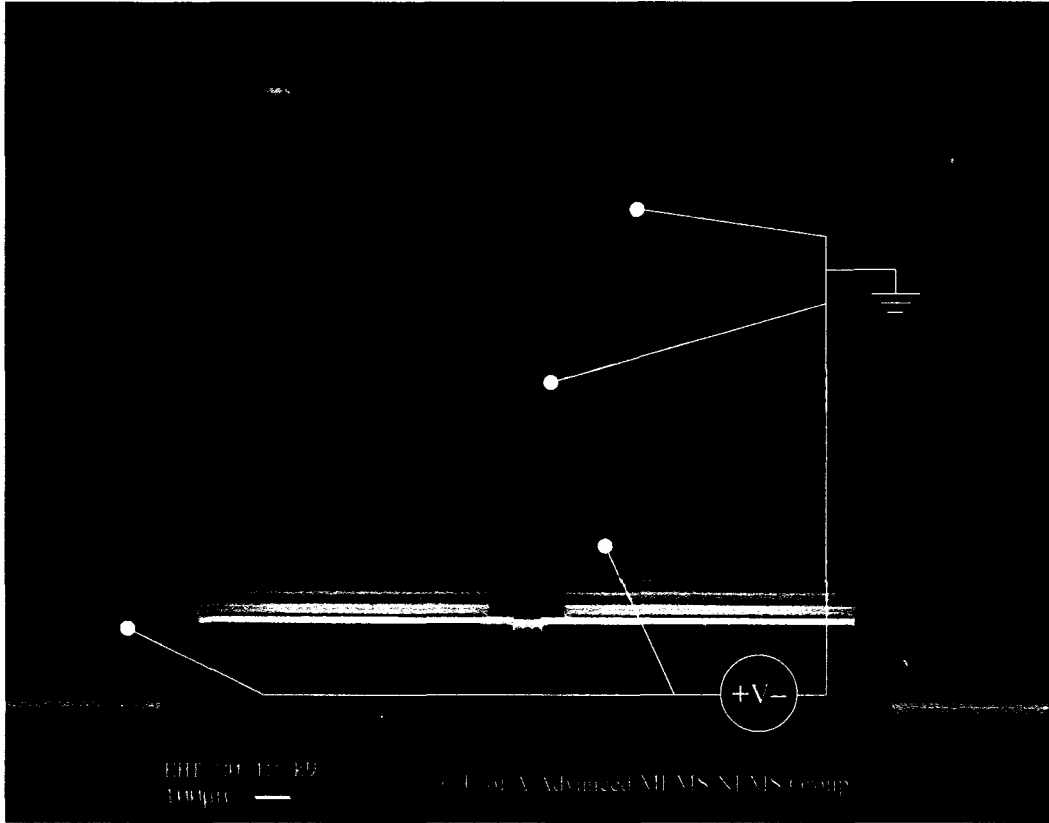


Figure 3.12: A schematic showing how the electrical circuit was applied to the prototypes during testing.

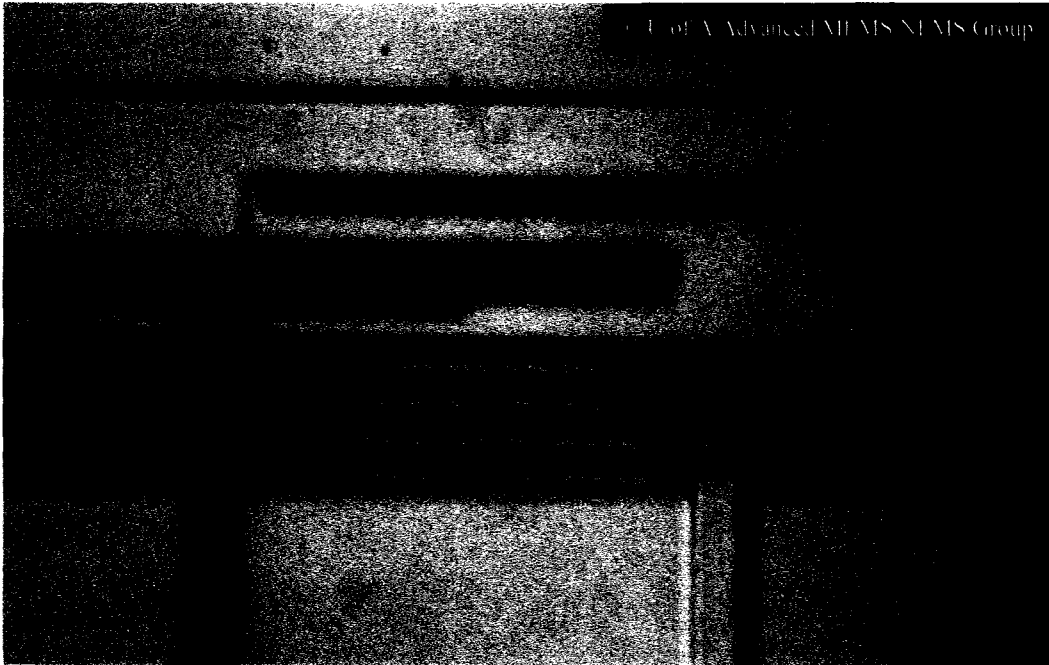


Figure 3.13: A movable comb that has broken free of its handle wafer.

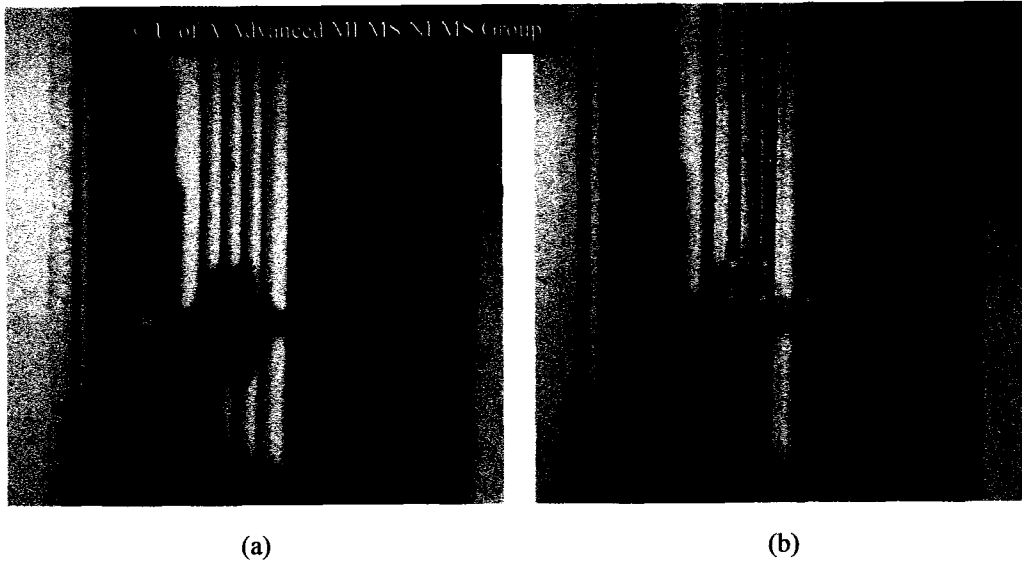


Figure 3.14: The actuation of a movable comb. (a) shows the undeformed shape; (b) shows the deformed shape.

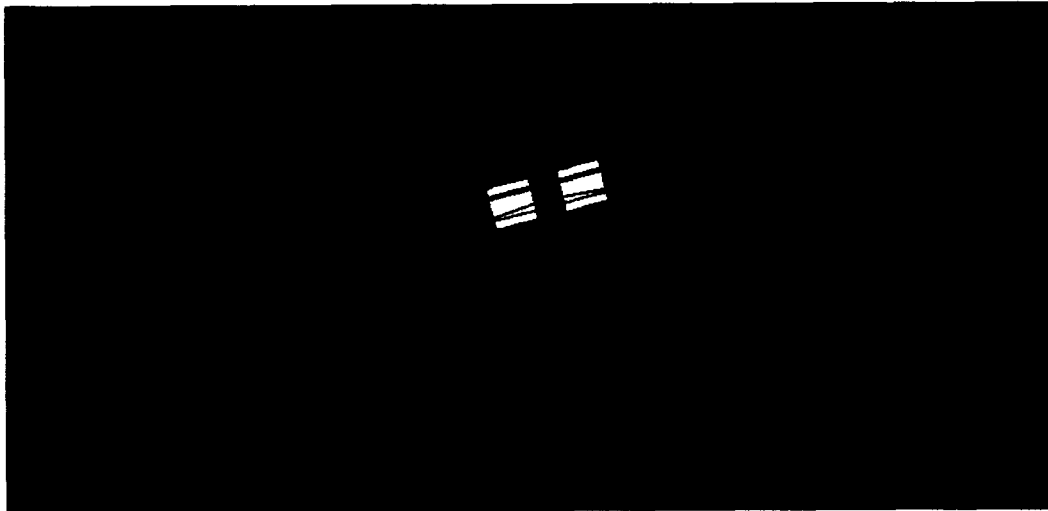


Figure 3.15: A bottom view of the finite element model of the movable comb of configurations A and B. The model was built in IntelliSuite™'s 3D Builder™ module.

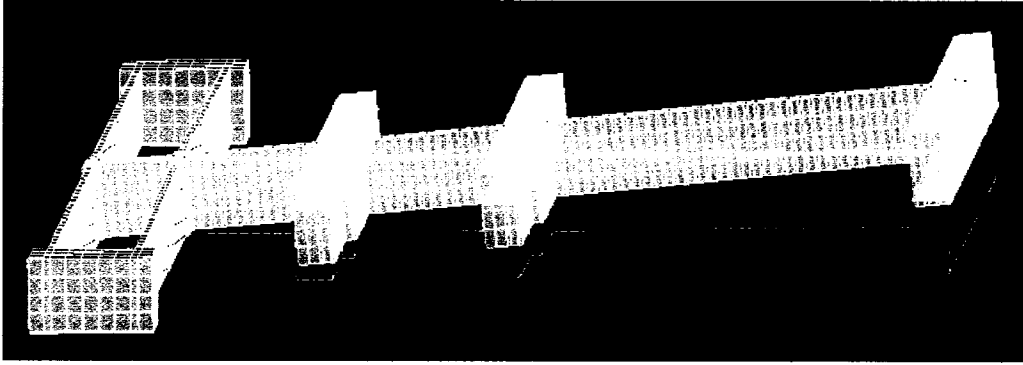


Figure 3.16: The mode shape of the first natural frequency of configuration E. The mode shape was calculated in ANSYS®.

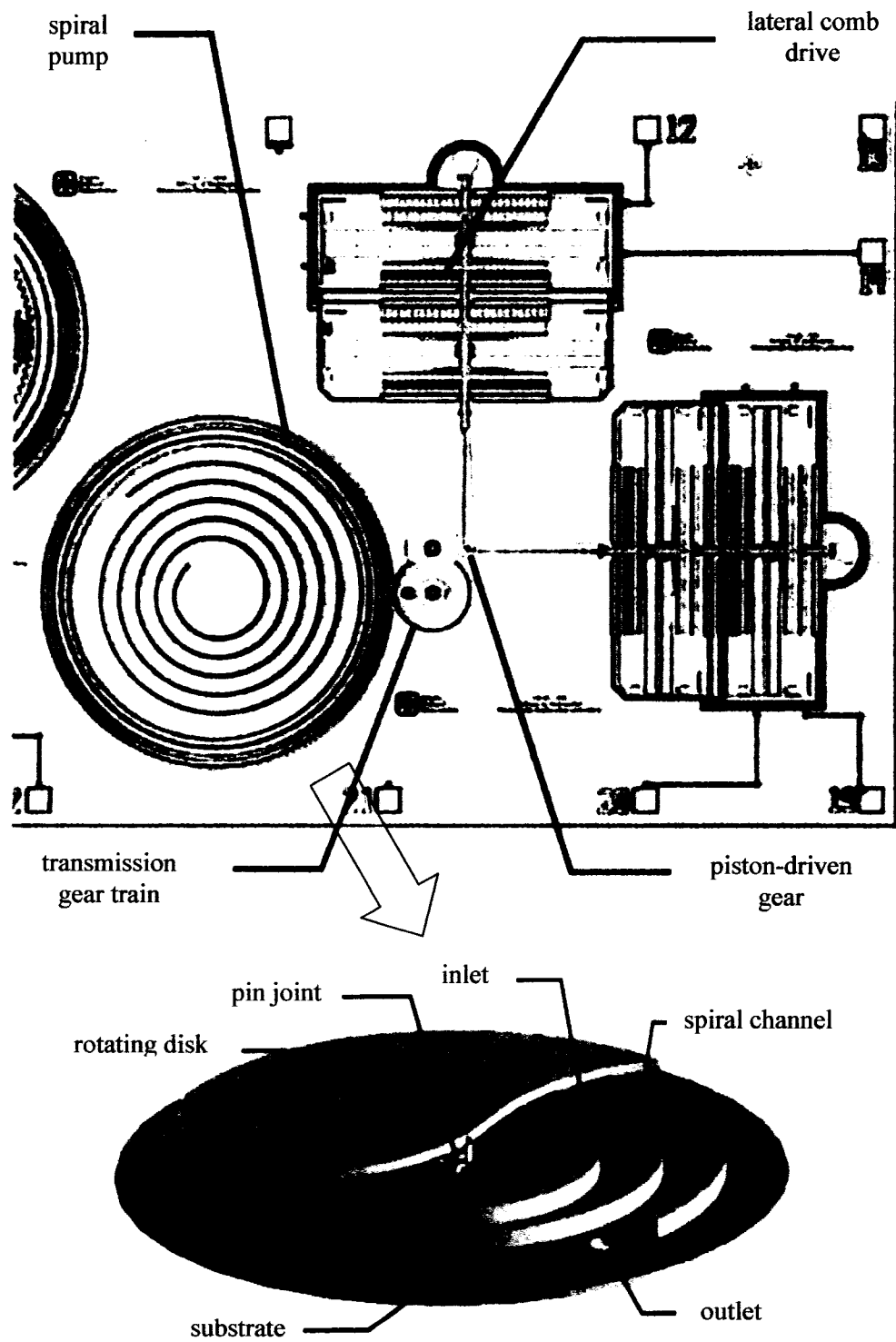


Figure 3.17: Another type of lateral comb-driven micropump. Adapted [18].

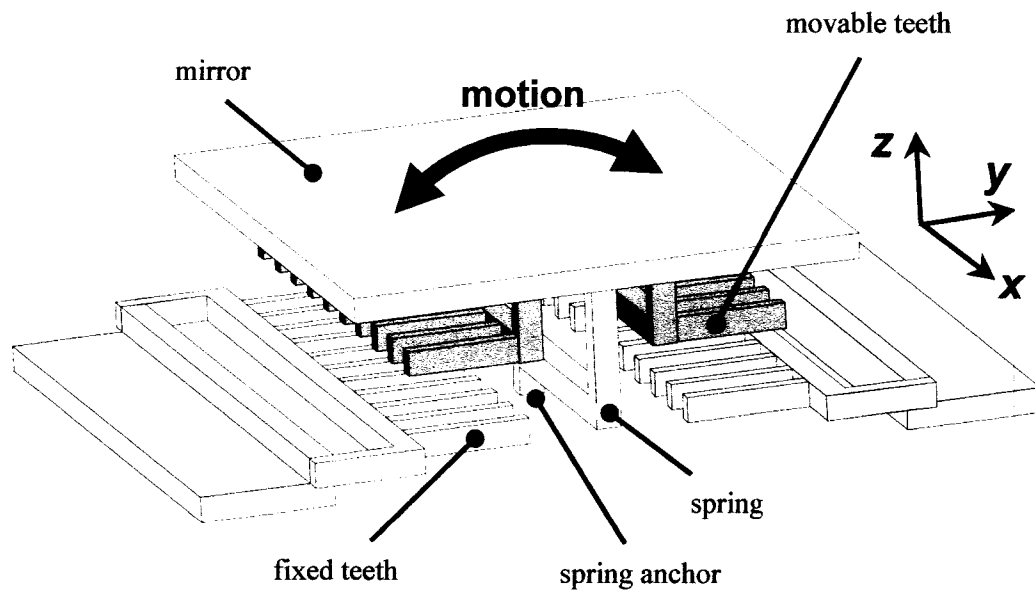


Figure 3.18: A schematic of a typical vertical comb drive. Adapted [31].

Chapter 4: Vertical Comb-Driven Micropump

For the second attempt made at pairing comb drives with micropumps, the opposite approach was taken: a new type of comb drive (also attached to a piston) was designed that could push against the diaphragm of a standard reciprocating displacement micropump. Taking a typical vertical comb drive and replacing its characteristic mirror with a piston, adjusting its springs to better allow pure vertical motion, and arranging to apply voltage differences within all of its comb pairs surrounding the piston simultaneously was thought to be a means by which to achieve this goal.

In order to fabricate, and thus design, vertical comb drives to actuate pistons, a typical fabrication process for vertical comb drives was first selected from the literature. The process and the design it was originally intended for was then modified to add a piston, and the design itself was modified so that the piston could undergo pure vertical motion. A set of governing equations was assembled to characterize the forces that would act on the movable combs attached to the piston, such that decisions could be made regarding the dimensions of the prototypes to be fabricated. Once these dimensions were chosen, the performance of the prototypes – in terms of their actual static displacement for a given voltage difference – was predicted. Finally, the prototypes of the vertical comb-driven pistons were partially fabricated, and the optimization of the fabrication process was begun.

4.1 Design Considerations

The vertical comb drives, without being overly large themselves, must be able to move up and down perpendicular to their handle wafers with as large a displacement as possible, as a relatively low voltage difference is applied between their fixed and movable combs. Their inherent ability to have long teeth in the orientation necessary for increasing the net electrostatic force between their combs should assist with this. However, while it may be simple to machine long teeth in the orientation required, it is not as simple to offset them in the vertical direction while maintaining their alignment in that direction.

Unfortunately, aligning its movable teeth properly between its fixed is crucial to the operation of any type of comb drive. In addition to the electrostatic force acting parallel to each side of each movable tooth, pulling it up between the fixed teeth on either side of it as described by Equation 2.4, an electrostatic force also acts perpendicular to each side of each movable tooth, pulling it towards its adjacent fixed teeth as in a parallel-plate actuator (and as illustrated in Figure 4.1).

Ideally, the force, F_{ex} , pulling the movable tooth in the positive x -direction, as described by Equation 4.1, will be balanced by an equal force on the opposite side of the tooth pulling it in the negative x -direction. These forces will only be equal, however, if the gaps, g , on both sides of the tooth are equal.

$$F_{ex} = \frac{1}{2} \varepsilon \frac{L_t (z - o) V^2}{g^2} \quad (4.1)$$

4.2 Process Selection and Modification

4.2.1 Process Selection

Several papers on the fabrication of vertical comb drives [19 – 23, 26, 28 – 30, 32] were reviewed in the search for a fabrication process that could be suitably modified to include the machining of a piston that would undergo piston-motion. All of the papers found describe a unique method of fabrication; most are detailed enough that the method suggested could be followed in another facility.

All of the papers found that describe fabrication processes for vertical comb drives (with the exception of one [20] that explains a method by which the top and bottom combs are fabricated separately and then aligned and bonded with the use of specialized equipment and fabricated alignment keys) tell of ways to properly arrange the movable teeth between the fixed by patterning their final shapes with one mask. Some processes seem more difficult to implement than others, however. One [28] begins with the machining of all of its combs from the device layer of an SOI wafer, and then relies on residual stresses (caused by the different thermal expansion coefficients of silicon and SiO₂) to deflect beams attached to the fixed combs, permanently positioning them lower than the movable combs. Many other processes involve materials and process techniques that are not the most widespread [22, 30], and/or extra process steps for trimming the heights of springs and teeth [22, 23] in ways that are unnecessary for the application at hand.

One of the simpler processes found in the literature search seems to be intended more for smaller deflections [19], as its movable combs are machined from a deposited polysilicon layer. The limited possible thickness of this layer would limit the centreline offset between the fixed and movable teeth, which would in turn limit the maximum possible displacement of the movable teeth. Another process [29], although relatively straight-forward, seems to rely heavily on process steps where it would be difficult to predict and gauge the release of the comb teeth from the substrate, as well as control the initial offset between the comb pairs. Also, it is unclear on how the fixed and movable teeth are to be electrically isolated from each other, as they are both etched from a single silicon wafer. Another process is reported [32] that also has both sets of teeth etched from the same silicon wafer, but unfortunately it mentions only briefly the further processing that is required to isolate the comb pairs. Finally, yet another process

does include a technique by which electrical isolation can be achieved [21], but it involves the fabrication of a custom silicon-on-insulator wafer – which also requires process techniques that are not the most wide-spread.

The process that was eventually chosen [26] to be modified for making vertical comb-driven pistons is relatively simple and employs standard materials and process steps. It begins with an SOI wafer and proceeds to etch the fixed and movable combs from the silicon on opposite sides of the insulating layer – thus they are automatically electrically isolated from each other, and the process conditions can be varied to produce relatively thick teeth for larger piston displacements. The various structures of the comb drive are all patterned from the top of the wafer with different numbers of masking layers. The final pattern deposited is etched through both the device layer and handle wafer from the top such that the fixed and movable teeth are automatically aligned; the structures masked with fewer layers than the rest (namely the springs) are thinned simply by being exposed sooner and are ultimately comprised of only the silicon below the insulator layer.

4.2.2 Process Modification

The fabrication process chosen from the literature [26], as with most of the processes found, was intended to be used for fabricating scanning micromirrors. Thus the first modification made to the process was the elimination of one of the last steps – the deposition of a thin metal layer on top of the etched structures. It was decided that the piston did not need to be reflective, and that metallization of the electrical contacts could be done later if wire-bonding was required for the testing of the prototypes.

It was also decided that SOI wafers with 15 μm -thick device layers and 0.5 μm -thick insulator layers would be used to make the prototypes out of. Since these layers are much thinner than those intended to be etched with the original process (which are 40 μm and 3 μm , respectively), the maximum aspect ratio of any trench etched through the device layers in the fabrication of the pistons is expected to be much less than those of the mirrors. Thus further steps were able to be eliminated from the fabrication process, as stopping the etch half-way through the device layer to open up wider trenches is not necessary for the wafers being used.

Finally, the arrangement of the layers that would mask the etches of the wafers was simplified. The alternating layers of deposited polysilicon and low temperature silicon dioxide were replaced with slightly more common materials – a thick (>1 μm) layer of thermally-grown silicon dioxide and the last layer of photoresist used to pattern it. Again, because of the thinner device and insulator layers of the wafers to be used, and the shorter etch times required to cut through them, photoresist was deemed to be enough to act as a masking layer for the structural etches. Even if it is found not to be, the modified process is sufficiently robust for it to matter little – the silicon of the device layer the photoresist will cover will be etched away after the photoresist is removed in the next process step anyway, and the oxide the photoresist will cover will be much thicker than that of

the insulator layer so that etching both at the same time will still produce the required results. The modified process for fabricating vertical comb-driven pistons is thus as follows (and is shown in Figure 4.2):

- 1.) clean the SOI wafers in a hot piranha solution to remove any contaminants on their surfaces
- 2.) thermally grow SiO_2 on both sides of the wafers (these will act as masking layers for the etches of the silicon beneath them)
- 3.) deposit photoresist on the tops of the wafers and pattern it with mask 1; RIE the top SiO_2 , and remove the photoresist (mask 1 opens up the areas that will be over the tops of the springs)
- 4.) deposit photoresist on the tops of the wafers and pattern it with mask 2 (mask 2 aligns the movable teeth with the fixed by opening up the areas that will be etched through the wafers, and leaving the final shapes of both sets of teeth)
- 5.) RIE the top SiO_2 to expose the silicon to be etched with mask 2
- 6.) DRIE through the exposed portions of the device layers, and RIE through the subsequently exposed portions of the insulator layers
- 7.) deposit photoresist on the bottoms of the wafers and pattern it with mask 3; RIE the bottom SiO_2 , and partially DRIE the exposed portions of the handle wafers to the same thickness as the device layers; remove the photoresist on both sides of the wafers
- 8.) DRIE through the handle wafers from the top to release the movable combs
- 9.) RIE the tops of the wafers to remove the SiO_2 from the tops of the springs and the electrical contacts

4.3 Evolution of Design

The basic design of the vertical comb-driven pistons is based on the design, shown in Figure 4.3, that corresponds to the fabrication process chosen [26] to be modified for fabricating the piston prototypes. The chosen process is intended to be used to fabricate double-gimbaled two-axis tilting micromirrors. The first change made to the mirror design to transform it into that of a vertical piston was the simplification of the arrangement of the springs and comb pairs around the mirror surface to remove unnecessary degrees of freedom.

The only thing added to the design was the piston itself – a block of silicon, as shown in Figure 4.4, that would remain on the mirror surface after the device layer had been etched. The piston was positioned on top of the mirror surface rather than the bottom so that it could push against whatever it is to move (rather than pull it) as the fixed combs bring the movable combs upwards. It would be difficult to adhere another component, such as the diaphragm of a micropump, to the piston well enough for the bond to withstand the tension that would develop between the two if the piston were used to pull on the diaphragm.

Although a diaphragm could be adhered to a piston well enough to be pushed by it – which would eliminate the need for additional springs to return the movable combs to their neutral positions (which would be ideal, since such springs only add to the overall stiffness of the system that the fixed combs must work against) – this sort of arrangement would be difficult to fabricate. Hence a spring design was sought after and settled upon [33] that would best encourage pure vertical motion of the movable combs while not requiring further etches to be added to the fabrication process. The springs shown in Figure 4.5 are thus wide, rigid beams set between pairs of thin beams in such a way as to transfer their twisting motion into vertical displacement, and in such a way as they can be etched in the same step as the teeth of the movable combs. To further minimize the stiffness they add to the system, the layout of the prototypes was organized so that as few as possible (only two) were required to provide stability to the piston. Although to minimize the size of the system it would be best if the anchors of the springs were set within the span of the fixed combs, instead they were moved outwards to increase the moments that would act against any external twisting forces in directions perpendicular to the axes of the wide spring beams. The comb pairs were arranged simply around them with more fixed teeth than movable so that both sides of each movable tooth would have an upwards force acting on it.

4.4 Design Calculations

To decide on the dimensions of the prototypes of the vertical comb-driven pistons – the dimensions of the springs and those of the comb teeth – some equations were assembled to characterize the stiffnesses of the chosen spring design and the electrostatic forces that would act on the movable teeth in various different directions. Some of the dimensions would be constrained by fabrication limitations more than others, of course – such as the widths of the thin spring beams and the horizontal gaps between the comb teeth – but the equations would allow the rest of the important geometries to be determined so that maximum piston displacements could be achieved with minimum voltages.

4.4.1 Weight Considerations

One of the first calculations conducted regarding the design of the prototypes was to verify that the weight of the piston and movable combs could be considered to be negligible. The total weight of the structures to be lifted was estimated by calculating their approximate expected volumes and multiplying them by either a density of 2.3g/cm^3 (for silicon) or 2.2g/cm^3 (for silicon dioxide). When compared to preliminary calculations of the electrostatic force that would lift the structures, the weight was found to be four orders of magnitude smaller, and thus can be assumed to not add significantly to the forces acting on the piston, and does not need to be considered when calculating its final displacement. The assumption can also be made that the rest position of the tops of the movable teeth

will be $0.5\mu\text{m}$ below the fixed teeth – set by the thickness of the insulator layer of the SOI wafers to be used – and that this initial offset will not be increased significantly by the weight of the released piston and movable combs.

4.4.2 Vertical Spring Constant

To characterize the restoring force that would act on the movable combs, an expression for the combined stiffness of the springs in the vertical direction, k_z , was derived. This was done by first assuming that the displacement of the piston, z , will be approximately equal to the displacement of the ends of the wide spring beams. The angle, θ , the wide beams are raised to will then be related to the displacement of their ends by:

$$\theta = \frac{z}{L_b} \quad (4.1)$$

assuming that θ is a small angle, and where L_b , shown in Figure 4.5, is the length of a wide spring beam. The angle the wide beams are moved through will be the same as the angle of twist in the thin spring beams. The moments, M , exerted by the thin beams on the ends of the wide beams can then be determined from this angle with a modified version of the standard torsion equation for circular cross-sections, where the polar moment of inertia has been replaced with a factor K [34] (and the stiffening effects of the end constraints have been neglected):

$$M = \frac{2KG\theta}{L_s} \quad (4.2)$$

where G is the bulk shear modulus of the silicon in the direction the beam lies in [35]. A factor of 2 is added to Equation 4.2 because L_s refers to the length of the thin spring beam on one side of a wide beam. The factor K is given by:

$$K = a_s b_s^3 \left[\frac{16}{3} - 3.36 \frac{b_s}{a_s} \left(1 - \frac{b_s^4}{12a_s^4} \right) \right] \quad \text{for } b_s \leq a_s = \frac{1}{2}t \quad (4.3)$$

where $2a_s$ is the thickness of the thin spring beams and $2b_s$ is their width. It should be noted here that the thickness of the thin spring beams is the same as that of the movable teeth, t , as both are etched from the handle wafer in the same process steps.

To relate the moments exerted on the ends of the wide beams to the net electrostatic force on the movable combs (F_e), a force balance was conducted on one of the wide spring beams, as shown in Figure 4.6. Each of the two wide beams per piston take up an equal share of the applied upwards force. Assuming that the wide beam remains rigid, the angle of twist in the thin beams at either end of it will be equal, thus, the moments they apply to either end will be equal – which gives Equation 4.4:

$$F_e = \frac{4M}{L_b}. \quad (4.4)$$

Finally, linking Equations 4.1, 4.2, and 4.4 together enables the relation of the vertical force to the vertical displacement, the proportionality coefficient between the two being the expression for the vertical spring constant:

$$F_e = \left(\frac{8KG}{L_s L_b^2} \right) z = k_z z. \quad (4.5)$$

4.4.3 Side-Sticking Criteria

Even if the original alignment between the fixed and movable combs of a vertical comb drive is perfect, as a prototype is exposed to the vibrations inherent in its environment its movable combs will never be perfectly stationary. Any lateral movement of the comb drive's movable teeth caused by an external agent will change the distance between those teeth and the fixed teeth on either side of them – which, if they have a different electrical potential than the fixed teeth, will unbalance the electrostatic forces acting perpendicular to their sides (in the x -direction shown in Figure 4.1). If the restoring force provided by the springs in the x -direction does not increase faster than the unbalanced electrostatic force in the x -direction side-sticking will result – where the movable teeth are drawn into the fixed and discharge their built-up electrons, which ultimately limits the vertical displacement of the movable teeth. To prevent this particular mode of failure the spring constant of the comb drive in the x -direction must be greater than the derivative of the unbalanced electrostatic force in the opposite direction as they both tend towards $x = 0$ [6, 13, 36].

The unbalanced electrostatic force on the movable combs of a comb drive, F_{un} , is the difference between the two forces acting perpendicular to the sides of the movable teeth (the greater force being applied on the side where the lateral gap between the fixed and movable teeth, g , has decreased):

$$F_{un} = \frac{\epsilon n L_t (z - o) V^2}{2} \left[\frac{1}{(g - x)^2} - \frac{1}{(g + x)^2} \right] \quad (4.6)$$

where x is the displacement of the movable combs in the x -direction shown in Figure 4.1. The derivative of F_{un} near $x = 0$ is:

$$\left[\frac{\partial F_{un}}{\partial x} \right]_{x \rightarrow 0} = \frac{2 \epsilon n L_t (z - o) V^2}{g^3}, \quad (4.7)$$

where it is noted that the unbalanced force, and the rate of change of the unbalanced force, is a maximum when the displacement of the movable combs in the vertical direction is at its maximum.

In deriving the spring constant of the chosen spring design in the x -direction, k_x , a preliminary estimate of the stiffness of the wide spring beams indicated that they could be assumed to be rigid in that direction. Considering only the various series and parallel arrangements of the thin spring beams, then, the effective spring constant was found to be twice that of a single thin beam (which is that of a fixed-fixed beam with one end displaced perpendicular to its length), thus:

$$k_x = 2 \left(\frac{12EI}{L_s^3} \right) \quad (4.8)$$

where I is the moment of inertia of the beam's cross-section (with its neutral axis lying in the direction perpendicular to the handle wafer), and E is the modulus of elasticity of the silicon in the direction the beam lies in [35, 37]. Although derived under the assumption that the spring beams have undergone no vertical displacement, this expression can be considered to be valid for the entire range of vertical displacement of the movable combs, as this displacement will be very small, and any change in the stiffness of the thin spring beams due to their deformed state will also be very small. A brief study was conducted to confirm this with finite element simulations, where forces in the x -direction were applied to a preliminary model of a comb-driven piston that had undergone various vertical displacements. The resulting x -displacements were calculated, and when compared to the forces applied, showed that the proportionality constant between them remained relatively constant – regardless of the vertical position of the movable combs.

4.5 Design Variations

To increase the yield of the prototypes fabricated, the dimensions of the basic design most sensitive to the fabrication conditions (the smallest dimensions – such as the gaps between the comb teeth and the widths of the thin spring beams) were adjusted to make three variations of the basic design – A, B, and C. The rest of the dimensions of A, B, and C, in turn, were varied to complement the chosen gaps and widths.

The process of selecting the actual dimensions of the prototype variations began with considering the crystal orientation of the wafers to be used. Such considerations do not need to be made for the chosen fabrication process itself, simply for the design of the prototypes – as the direction the thin spring beams are etched in will determine their material properties and thus the dimensions they need to have to be of a particular stiffness. The most common type of silicon wafers, those of (100) orientation, are the type that make up the SOI wafers to be used to fabricate the comb-driven pistons. The prototypes are intended to be oriented on the wafers such that their thin spring beams lie along one of the

$\langle 100 \rangle$ axes, so they will have a modulus of elasticity of 130.2GPa, a Poisson's ratio of 0.279, and a bulk shear modulus of 79.4GPa [35, 37].

The device layer and insulator layer thicknesses of the SOI wafers to be used are 15 μm and 0.5 μm , respectively, so the fixed teeth of the vertical comb drives will be 15 μm and the initial vertical offset between their fixed and movable combs will be 0.5 μm . For this particular comb drive design the handle of the SOI wafer is meant to be thinned such that the thickness of the movable teeth will be equal to that of the fixed. Since these thicknesses will not vary between designs A, B, and C, all of the designs have the same theoretical limit to the displacement of their pistons – the vertical distance between the resting position of their movable combs to the point where their centres will align with that of their fixed combs is 15.5 μm .

The characteristics of designs A, B, and C are given in Table 4.1. Six variable dimensions were identified as being important to the performance of the pistons. Three of them are of the comb teeth – the horizontal gap between the fixed and movable teeth, g , the overlapping length of the fixed and movable teeth, L_t , and the number of movable teeth, n . These will influence the electrostatic forces that act on the pistons. The other three dimensions that affect the performance of the pistons are of the springs – the length of the wide spring beams, L_b , the length of the thin spring beams, L_s , and the width of the thin spring beams, $2b_s$. These will influence the restoring forces that act on the pistons.

Adjusting these six dimensions to design prototypes capable of large piston displacements generated by low voltages, while preventing side-sticking of the movable combs, requires a close examination of how much these parameters are affected by each of the dimensions. Generally, changing the dimensions of the comb teeth to increase the electrostatic force on the movable teeth in the vertical direction will also increase the unbalancing force on the movable teeth in the x -direction, and stiffening the springs in the x -direction to prevent side-sticking will also stiffen them in the vertical direction. However, the electrostatic forces exerted on the movable teeth in one direction depend more on some of the tooth dimensions than the electrostatic forces in the other direction. For instance, increasing the lateral gap, g , between the teeth will decrease the unbalanced lateral force more than the upwards driving force. Similarly, the stiffnesses of the springs in both directions also depend on the beam dimensions to differing extents. While the length of the thin spring beams, L_s , is important for both spring constants, it influences the constant in the x -direction much more than the one in the vertical direction. Finally, the length of the wide spring beams, L_b , is the one dimension that does not oppositely influence both the vertical displacement and the side-sticking criteria, as it does not influence the lateral restoring force at all. Increasing L_b lowers k_z without lowering k_x , and thus is limited only by rigidity concerns and the overall size of the prototypes.

The last considerations that had to be made in choosing the dimensions of the prototypes were in regards to the fabrication process constraints themselves. It is estimated that gaps between the fixed and movable teeth as small as 2 μm can be etched through both the device layer and handle wafer of the SOI wafers being used, and that spring beam widths as small as 3 μm can be etched from the handle

wafer. It is also estimated that variations in these dimensions will need to be of at least $0.5\mu\text{m}$ to make a difference in fabrication quality [38].

The final dimensions of the prototypes are given in Table 4.1, along with the properties of the designs calculated from them. Included are brief displays of how the derivatives of the unbalanced electrostatic forces are expected to increase over the vertical displacement of the movable combs. The actual constraints imposed on the voltage/displacement and side-sticking parameters that were used to determine the dimensions of the prototypes, that can also be seen in Table 4.1, are that: 1.) the derivative of the unbalanced force should be approximately $2/3$ of the horizontal spring constant at the maximum displacement of $15.5\mu\text{m}$; 2.) the applied voltage difference should be below 100V ; and 3.) the initial estimate of the piston displacement, calculated by equating Equation 2.4 with Hooke's law, should be greater than $15.5\mu\text{m}$ (as Equation 2.4 tends to overestimate the net electrostatic force in vertical comb drives, which will be examined in later sections). The dimensions of designs A, B, and C were adjusted to meet these constraints, as well as those of the fabrication process. It was decided that the minimum width of $3\mu\text{m}$ for the thin spring beams should be tested, and increased in steps of $0.5\mu\text{m}$ for the other designs to observe what sort of difference such a small variation would make in the quality of the springs. The minimum lateral gap found to satisfy the side-sticking requirements is also $3\mu\text{m}$, and again, is increased in steps of $0.5\mu\text{m}$ to observe whether such increments will make a difference in the fabrication. The lengths of the thin spring beams were alternately decreased and increased to stiffen the springs in the x -direction and soften them in the vertical direction, respectively, and the overlapping length of the comb teeth, as well as the number of movable teeth, were set as needed to compensate for high spring constants in the vertical direction. Lastly, while the lengths of the wide spring beams were lowered for design B for stiffness and size considerations (as its large number of comb teeth and large gap between them make it the biggest of the designs), the lengths were generally allowed to remain high for the other two – to maximize the displacement of design C and to minimize the voltage required by design A.

The remaining dimensions of the comb drives were simply chosen as what seemed reasonable – mainly for rigidity, as they are expected to have only a very small effect on the electrostatic and restoring forces that will occur in the prototypes. The widths of the wide spring beams of all of the designs are $50\mu\text{m}$, and the widths of their comb teeth, w , are $5\mu\text{m}$. The widths of the movable combs were increased with their length. The horizontal distance between the ends of the teeth and the insides of the opposing combs, shown as s in the unit comb drive of Figure 4.7, were chosen as what seemed necessary for freedom of movement, and thus are also $5\mu\text{m}$. It should be noted here that the total lengths of the comb teeth are the sum of this dimension and their “overlapping length”.

4.6 Performance Predictions

4.6.1 Natural Frequency

A few calculations were conducted to estimate what the natural frequencies of the three design variations would be. To examine piston-motion in the vertical direction, the comb drives were modeled as three masses connected in series by torsion springs as shown in Figure 4.8. By examining the forces that would be exerted on the masses by the springs, and the resulting accelerations of the masses, an equation of motion was derived to characterize the system, and the natural frequency was taken from it as the square root of the effective spring constant over the effective mass:

$$p = \sqrt{\frac{4KG}{L_s I_b^2 \left(\frac{m_p}{2} + \frac{m_b}{3} \right)}} \quad (4.9)$$

where m_p is the mass of the movable combs and piston, and m_b is the mass of the wide spring beams. Using this relation, the natural frequencies of designs A, B, and C for piston-motion are estimated to be 2900Hz, 3279Hz, and 3388Hz, respectively.

To confirm these values, and to discover which natural frequency of each design corresponds to piston-motion, finite element simulations were conducted with full three-dimensional models of the pistons, movable combs, and anchored springs in the ThermoElectroMechanical Analysis™ module of IntelliSuite. The first three natural frequencies of each design variation were calculated and are given in Table 4.2.

Upon inspection of the mode shapes also calculated by the simulation program, the expected piston-motion was found to correspond to the first natural frequencies of all three designs. Those calculated numerically tended to be 13-15% below those found with Equation 4.9, likely due to their inclusion of the mass of the thin spring beams, and the compliance of the wide spring beams and movable combs.

These natural frequencies will not be those of the systems if the rest of the micropump components are attached to them, of course – adding a diaphragm for the pistons to push against will stiffen the systems, and increase their natural frequencies. Any fluid in the pump chambers will dampen the motion of the pistons, as well. The amount of this damping will depend on the types of fluids being pumped and the geometries of the pump chambers. It is suspected that this damping will generally be more than the critical value for the system, however, as it is likely that the fluid to be pumped is relatively incompressible. Thus further evaluation of the chosen prototype designs focused on quasi-static motion of the pistons, as that is the frequency region where the maximum displacements of the pistons are expected to occur.

4.6.2 Piston Displacement

In attempting to predict the maximum vertical displacements of the prototype pistons, a disadvantage of using vertical comb drives for piston-motion was realized: while having long teeth that lie parallel to their substrates may allow them to provide greater electrostatic forces with smaller driving voltages, it will also limit their displacements. This limitation will make predicting their displacements more difficult, as there will be only very short distances over which their two sets of teeth will overlap before their edges begin to approach each other and start to affect the capacitance between their teeth. Thus the net electrostatic forces exerted on their movable combs cannot be assumed to stay constant with their displacements as it is for lateral comb drives, and cannot be described by Equation 2.4 alone.

Clearly, the electrostatic forces on the movable teeth of a vertical comb drive will diminish as they move away from the fixed teeth, but of particular interest is what will happen when they begin to align with them in the vertical direction. As the movable combs begin to align with the fixed, the electrostatic forces on them should diminish again, as the fixed combs will certainly not draw the movable combs past them. The springs attached to the movable combs will still apply an increasingly strong restoring force downwards, though, so statically, the movable teeth should never become fully aligned with the fixed teeth. In order to predict how close they get to becoming fully aligned (and thus the maximum displacement of the piston attached to them), a way to predict the fringe effects – the effects of the corners of the comb teeth on the electrostatic forces they exert on each other – must be found.

Some work has been done thus far in terms of developing expressions for the electrostatic forces that occur outside of the area directly between the comb teeth (shown in Figure 4.9), as well as more accurate expressions for those that occur inside this area [39]. Unfortunately, these particular expressions are only valid for when the comb pairs are either separated or engaged by a certain distance. The nature of the forces in between these regions is speculated upon using a linear fit function, which seems to be a reasonable approximation. However, the expressions themselves depend on the width of the comb teeth more heavily than seems reasonable, and, while they are certainly useful for finding the forces for specific cases of teeth geometries, they are not as practical for finding the optimum geometries for specific forces [40].

Further work has been done to characterize how the electrostatic forces between the movable and fixed teeth vary with the displacement of the movable teeth over their entire range of possible displacement [40]. This work involves conformal mapping of a two-dimensional model of a half unit comb drive (comprised of opposing halves of one fixed tooth and one movable tooth), where the widths of the teeth are assumed to be negligible, and the ends of the teeth are assumed to be far enough away from the insides of the combs – and the movable combs far enough away from any ground plane – that neither the sides of the combs nor a ground plane contribute significantly to the electrostatic force on the movable combs. The end result of this work is effectively a correction to

Equation 2.4, shown in Equation 4.10, that is based on the positions of the tops and bottoms of the fixed and movable teeth (a' , b' , c' , and d' – relative to a scale shown by the dotted line in Figure 4.10), or, the thicknesses of the teeth and the displacement of the movable teeth (t_f , t_m , and z , also shown in Figure 4.10):

$$F_e = \varepsilon n L_t \frac{V^2}{g} f_a(t_f, t_m, z) \quad (4.10)$$

$$= \varepsilon n L_t \frac{V^2}{g} \cdot \frac{\pi^2 \left(a \frac{b-d}{a-d} - b \frac{a-c}{b-c} \right)}{4(a-b) \left\{ F[\delta(u=0), q] + F[\kappa(u=0), q] \right\}^2}$$

where

$$q = \sqrt{\frac{(b-c)(a-d)}{(a-c)(b-d)}} \quad (4.11)$$

$$\delta = \sin^{-1} \sqrt{\frac{(b-d)(u-c)}{(b-c)(u-d)}} \quad (4.12)$$

$$\kappa = \sin^{-1} \sqrt{\frac{(a-c)(b-u)}{(b-c)(a-u)}} \quad (4.13)$$

and F is the incomplete elliptic function of the first kind – one representation of which is given in Equation 4.14 [41]. It must be approximated numerically.

$$F(\varphi, k) = \int_0^{\sin \varphi} \frac{dp}{\sqrt{(1-p^2)(1-k^2 p^2)}} \quad (4.14)$$

The remaining variables – a , b , c , and d – can be related to the physical endpoints through Equations 4.15 – 4.18.

$$a = e^{\pi(b'+t_m)/g} \quad (4.15)$$

$$b = e^{\pi b'/g} \quad (4.16)$$

$$c = -e^{-\pi t_f/g} \quad (4.17)$$

$$d = -1 \quad (4.18)$$

Finally, relating b' to z is trivial – the co-ordinate system chosen for the work described here has its origin at the rest position of the movable combs, and increases as they align with the fixed combs, thus:

$$b' = o - z \quad (4.19)$$

Calculations were conducted using the above equations to determine how they would predict the electrostatic forces for the three piston designs over their range of displacement, and several three-dimensional computer models of the pistons were built and analysed to determine the same. Here the results obtained from both will be compared, and used to predict the final displacements of the three comb drives undergoing piston-motion as their movable combs begin to align with their fixed.

4.6.2.1 Numerical vs. Analytical Prediction of Net Electrostatic Force

Figure 4.11 shows the various proposed magnitudes of the electrostatic forces, as well as the restoring force, that are expected to be exerted on the movable combs of pistons A, B, and C as the combs move from rest to a displacement of $15.5\mu\text{m}$. The horizontal “parallel-plate theory” lines are the electrostatic forces calculated from Equation 2.4 using the dimensions listed in Table 4.1, and neglect any kind of fringe effects; the “analytical fringe theory” curves are the electrostatic forces similarly calculated from Equations 4.10 – 4.19; and the “spring” lines are the restoring forces – and have slopes equal to the vertical spring constants also in Table 4.1.

The “simulated fringe theory” curves were generated by building a computer model of one comb pair from each of the three designs, applying a dielectric constant of 11.8 to the silicon teeth, and conducting boundary element “static electrostatic force vs. displacement” simulations with them in the ThermoElectroMechanical Analysis module of IntelliSuite. These analyses produced tables of the electrostatic forces exerted on the movable combs over their range of displacement; the values listed were collected and doubled to account for the second comb pair in each design not modeled. The curve fitted to the simulation data in Figure 4.11 is a 6th-order polynomial supplied by Microsoft® Excel.

As can be seen in Figure 4.11, both of the electrostatic force curves that include fringe effects increase as the movable teeth are initially drawn up between the fixed, and decrease abruptly as they begin to align with them. The analytical curve does not reach the parallel-plate constant force, while the simulated curve lingers both above and below it as if the constant force were an average value. Because the simulated curve begins to decrease sooner than the analytical curve, it will predict slightly smaller final displacements of the pistons.

By determining where the “spring” lines intersect the electrostatic force curves in Figure 4.11 (as these will be the new equilibrium positions when a voltage difference is applied to the comb pairs), the final displacements of the pistons were predicted to be $12.5\mu\text{m}$ and $13.1\mu\text{m}$ for design A (the lower value being from the simulated curve, the higher from the analytical), $12.5\mu\text{m}$ and $13.3\mu\text{m}$ for design B, and $13.5\mu\text{m}$ and $14.0\mu\text{m}$ for design C. All of the horizontal “parallel-plate theory” lines will intersect the “spring” lines well above the maximum possible displacement of $15.5\mu\text{m}$.

4.6.2.2 Full-Model Simulation Results

Displacement results from two full three-dimensional computer models (those of designs A and B) were also obtained to compare with the displacements predicted with Equations 4.10 – 4.19 and the “electrostatic force vs. displacement” simulations. The models used were similar to the ones built to find the natural frequencies of the piston designs – with the anchored springs and movable combs – although fixed combs needed to be added to the models and the pistons themselves were removed to reduce the number of elements. The electrostatic meshes on the comb teeth were refined to match those used on the combs for the “electrostatic force vs. displacement” simulations. “Static thermoelectromechanical relaxation” hybrid finite and boundary element simulations were conducted with the models in the ThermoElectroMechanical Analysis module of IntelliSuite, where a voltage difference was applied between their fixed and movable combs and the program calculated the deformed shapes of their springs.

The simulation performed with piston A converged to a final displacement of 9.0 μm . The results obtained for piston B were found to be converging – simple extrapolation techniques estimated a final displacement of 11.5 μm . These results are summarized in Table 4.3 along with those obtained from the intersections of the electrostatic and spring force curves. As can be seen in Table 4.3, the final displacements predicted by the analyses of the full models tended to be lower than the other displacements, and thus closer to those predicted by the simulated force curves.

4.7 Examination of Assumptions Made in Derivation of Analytical Fringe-Correction

In addition to the analysis of the three piston designs, a small study was conducted to investigate the validity of some of the assumptions made in the derivation of Equation 4.10 – specifically, whether the widths of the comb teeth, as well as the distance between the ends of the teeth and the insides of the opposing combs, have an effect on the electrostatic forces between the fixed and movable teeth. A model of a unit comb drive (shown in Figure 4.7) was made from the combs of piston A, and then modified to make further models with various different w and s dimensions. Again, these models were used to carry out “static electrostatic force vs. displacement” simulations (where the electrostatic forces on the movable teeth were obtained for various positions of the movable teeth over their range of displacement) in the ThermoElectroMechanical Analysis module of IntelliSuite.

4.7.1 Effect of w on Net Electrostatic Force

To investigate the effect of the widths of the comb teeth on the electrostatic forces generated between them, three models of unit comb drives were built with different tooth-widths than design A – one with widths twice that of design A

($10\mu\text{m}$ – which is much larger than is necessary for such a comb drive), one with widths that are approximately the smallest that is reasonable to attempt to fabricate from the SOI wafers being used ($3\mu\text{m}$), and one with widths much smaller than is reasonable to fabricate – to approximate teeth with negligible widths ($0.1\mu\text{m}$).

As shown in Figure 4.12, the magnitudes of the electrostatic forces generated in the unit comb drives, while obviously smaller than those in the full comb pairs previously analysed, do follow curves similar to those of the comb pairs. Over most of the range of the movable teeth's displacement, the variations in tooth widths do not seem to affect the electrostatic forces exerted on them significantly – particularly the maximum forces that occur when they overlap the fixed teeth by about one-third. As the overlap increases, however, wider teeth do seem to lead to lower forces, as do narrower teeth when the overlap is very small or the fixed and movable teeth are still separated. Since some of the electrostatic forces initially pulling the movable teeth upwards likely act on their top surfaces, this trend seems reasonable, as limiting these areas would limit the forces able to act on them. These observations suggest that the inclusion of the tooth widths in the numerical simulations may account for some of the differences between the curves they generate and those generated by Equations 4.10 – 4.19.

4.7.2 Effect of s on Net Electrostatic Force

The investigation of the effect the dimension s has on the electrostatic forces between fixed and movable comb teeth was tailored more specifically to the pistons designed. If s is small enough relative to the rest of the teeth dimensions, the forces exerted by or on their ends will, of course, be significant compared to the rest of the forces between them. The goal of this study, therefore, was to determine whether the teeth of the pistons designed are a good approximation of one of the assumptions made in the derivation of Equation 4.10 – that s is large enough that the forces at the ends of the teeth can be neglected. For this study, two models of unit comb drives were built with different spaces, s , than design A – one with spaces twice that of design A ($10\mu\text{m}$), and one with spaces that, again, are approximately the smallest that is reasonable to attempt to fabricate from the SOI wafers being used ($2\mu\text{m}$).

Similar to Figure 4.12, Figure 4.13 shows the magnitudes of the electrostatic forces generated in the s -varying models following curves typical of the simulations thus far conducted. It also shows that there is little difference between the electrostatic forces generated in the $5\mu\text{m}$ and $10\mu\text{m}$ models – which indicates that the space, s , in the pistons designed is large enough that the electrostatic forces exerted on the ends of their movable teeth, and on the areas in between them, will not contribute significantly to the total electrostatic force on their movable combs, nor to the difference between the electrostatic force curves generated from Equations 4.10 – 4.19 and the simulations.

A smaller space, s , of course, will increase the electrostatic forces between the combs, as shown by the $2\mu\text{m}$ model. This dimension should not be excessively decreased to maximize these forces, however, as in addition to

fabrication difficulties it could lead to side-sticking of the movable teeth in their lengthwise direction.

4.8 Derivation of Numerical Fringe Correction

In light of the differences between the electrostatic forces predicted by Equations 4.10 – 4.19 and the simulations conducted in the IntelliSuite modules, it was decided that an alternate fringe function should be derived based on simulation data. Equation 4.10 offers a correction to the original analytical expression for electrostatic forces in comb drives (Equation 2.4) involving only the thicknesses of their movable and fixed teeth, and the displacement of their movable teeth; here a similar correction will be constructed by varying the movable tooth thickness in models of unit comb drives and conducting more “static electrostatic force vs. displacement” simulations with them in IntelliSuite. The resulting forces will be non-dimensionalized (such that they do not depend on the applied voltage or other dimensions of the models, etc.) and graphed against the movable tooth thicknesses and their displacements – both of which will also be non-dimensionalized relative to the fixed tooth thickness. The new fringe function proposed will be the equation of a three-dimensional surface fit to the non-dimensionalized simulation data.

Again, the unit comb drive taken from piston A was used as the standard model with a movable-to-fixed tooth thickness ratio of 1. Incorporating different thicknesses of movable teeth, the ratios for the other six models built ranged between 0.25 and 2. The original total displacement of $15.5\mu\text{m}$ was also used – measured between the vertical midpoints of the fixed and movable teeth – although the scale was reversed in direction (ie. $z' = z - 15.5\mu\text{m}$) such that its origin corresponds to the midpoint of the fixed teeth and decreases downwards. The displacement of the movable teeth, in turn, was also non-dimensionalized – “-0.5,” for example, represents the midpoints of the movable teeth passing the bottoms of the fixed. The movable teeth in the model with the thickness ratio of 1 would begin to disengage the fixed teeth at “-1”; the movable teeth of the other models, being of different sizes, would disengage sooner if $t_m/t_f < 1$, and later, if at all in the $15.5\mu\text{m}$, if $t_m/t_f > 1$. The electrostatic forces on the movable teeth collected from the simulations were multiplied by “ $g/(\epsilon L_f V^2)$ ” and then plotted in Stanford Graphics©.

Figure 4.14 shows the data graphed; Figure 4.15, the surface fit to it. For the ranges plotted, it would seem that the thinner movable teeth generally experience lower peak forces over narrower periods of displacement. The peak forces tend to increase with the thickness of the movable teeth until it approaches that of the fixed, whereupon they level off; at the same time, the regions where they occur shift downwards – it appears as if they tend to arise shortly after the initial engagement of the comb teeth. Also, the electrostatic forces generated between combs with tooth thickness ratios close to 1 seem to begin to approach zero last as the combs start to align.

The orders of the polynomial surface that was fitted to the simulation data were chosen to be the lowest values that seemed to follow the contours of the data reasonably well – 6 for the z'/t_f -direction and 4 for the t_m/t_f -direction. Equation 4.20 is the predicted electrostatic force in a comb drive with the newly-proposed correction for fringe effects:

$$\begin{aligned}
 F_e &= \epsilon n L_t \frac{V^2}{g} f_s \left(\frac{t_m}{t_f}, \frac{z'}{t_f} \right) \\
 &= \epsilon n L_t \frac{V^2}{g} \cdot \sum_{i=0}^6 \sum_{j=0}^4 a_{ij} \left(\frac{z'}{t_f} \right)^i \left(\frac{t_m}{t_f} \right)^j
 \end{aligned} \tag{4.20}$$

where the coefficients a_{ij} are summarized in Table 4.4. The expression is, of course, most accurate near the centre of the region studied.

4.9 Prototype Fabrication

4.9.1 Mask Design

The design of the prototypes of the vertical comb-driven pistons continued with the design of the physical masks that would be used to pattern the 100mm-diameter wafers. A total of three masks would be required for the process outlined in Section 4.2.2; the first, to remove the sections of the device and insulator layers above the springs, the second, to etch the shapes of the springs and comb teeth through the SOI wafers, and the third, to thin sections of the handle wafers to make the springs and movable teeth.

The patterns of the masks were drawn using the dimensions listed in Table 4.1, along with some consideration towards alignment tolerances. Since it is unnecessary for the workings of the comb drives to take the device layer off the tops of the movable teeth, for the first round of prototypes it was decided that mask 1 should simply have rectangles positioned over the outlines of the springs in mask 2, such that the final shape of the pistons would be the outlines of the movable combs minus the ends of these rectangles. This way the edges of the rectangles could be set half-way between the ends of the thin spring beams and the ends of the fixed teeth. Conversely, if a pattern were to be arranged over the movable teeth, its edges would have to be set half-way between the fixed and movable teeth. For design A, with a gap of $3\mu\text{m}$, this would mean that the pattern could be misaligned by $1.5\mu\text{m}$ in either direction, whereas the rectangles could be misaligned by $15\mu\text{m}$. Mask 3, on the other hand, is meant to be used on the opposite side of the SOI wafers than the other two masks, and aligned with infrared light shone through the wafers. It is estimated that an accuracy of $5\mu\text{m} - 10\mu\text{m}$ can be achieved with this backside alignment, so openings were drawn in mask 3 beneath the prototype shapes of mask 2 $15\mu\text{m}$ outside the holes that would be etched through the wafers.

Beyond the patterns for the prototypes themselves, a few more shapes had to be added to complete the design of the masks. In case the testing of the prototypes required the wafers to be diced, visible lines (50 μ m wide) were placed on mask 1 to guide this process – such that the size of each die would be 1cm x 1cm. So as to not make the wafers weak from thinning too many areas on their backsides, only six prototypes were put on each die – two of each design – and arranged 4mm apart lengthwise, centre to centre, and 2.5mm apart width-wise. To leave at least 4mm around the edge of the wafers open for handling purposes, a total of 52 dicing boxes were arranged on mask 1. Also on mask 1, extra lines were drawn around the prototypes to isolate the fixed combs of one piston from another.

All three masks have four windows spaced such that the edges of the wafers can be centred in them to begin the alignment process. Each mask also has alignment marks to refine the alignment between patterned wafers and successive masks. These marks are arrangements of four squares set close together to make a cross in between them. Each cross is slightly smaller than the last so that it can be centred within the pattern on the wafer left by the last mark. The alignment marks of mask 1 allow groups of four squares to be etched through the top masking oxide of the wafers so appropriately-sized crosses on mask 2 can be aligned within 5 μ m of their centres. Mask 2, with a second set of alignment marks, also allows groups of four squares to be etched through the device and insulator layers of the wafers so appropriately-sized crosses on mask 3 can be aligned within 10 μ m of their centres. Each set of alignment marks is made up of two groups of squares positioned on opposite ends of the masks. Those sets that are to align mask 3 with mask 2 are positioned 60mm apart, centre to centre, for the equipment to be used for backside alignment. Those sets that are to align mask 2 with mask 1 are positioned 10mm beyond them.

4.9.2 Processing Completed

The masks for the prototypes of the vertical comb-driven pistons were fabricated in a fashion similar to that for the prototypes of the lateral comb-driven pistons – sections of the photoresist on the blank masks were exposed with a laser and then etched away with the chromium beneath them to uncover sections of the glass.

It was decided that the fabrication process for the prototypes should be tested with silicon wafers before being used on the SOI wafers. The resulting fixed and movable combs would not be isolated from each other, so the pistons could not be electrically actuated, but silicon wafers are less expensive and more readily available than SOI wafers, and can show almost as well whether the exposure times of the photoresist and etch profiles of the silicon are as they are intended. The silicon wafers were thus:

- 1.) **Piranha Cleaned** – placed in a fresh (110°C -130°C) 3:1 solution of H₂SO₄ and H₂O₂ for 15min, and then rinsed with water.

- 2.) **Thermally Oxidized** – baked in a Minibrute oven set at 1000°C for 7 hours while steam from water kept at 98°C-99°C was vented through the chamber. The SiO₂ layers grown on the wafers were measured to be approximately 1.2µm thick.
- 3.) **Covered in HMDS** – placed in an automatic YES HMDS dispense oven to prepare their surfaces for photoresist adhesion.
- 4.) **Patterned with Photoresist** – covered on top in HPR504 spun to a thickness of 1.3µm, softbaked on a hotplate, and exposed to UV light through mask 1 for 4.0s. The exposed photoresist was subsequently etched away with developer 354 in less than 25s, after which the wafers were quickly rinsed with water.
- 5.) **Reactive Ion Etched** – placed face-up in a Trion RIE. By measuring the thickness of the exposed SiO₂ after a few seconds of ion bombardment, the Trion was found to etch the oxide at a rate of 0.6nm/s. Thus to get through oxide layers of 1200nm the wafers were etched for a total of 2000s.

It should be noted here that RIE processes tend to “burn” photoresist. They do not etch it significantly, so it can be used to shield the layers beneath it, but its chemical properties tend to become drastically altered in the process.

- 6.) **Stripped of Photoresist** – rinsed with acetone, IPA, and then with water [42].
- 7.) **Re-patterned with Photoresist** – covered in HMDS, covered on top with 1.3µm of HPR504, softbaked, and then exposed to UV light through mask 2 for 2.8s – 3.0s. The exposed photoresist was then etched with developer 354.
- 8.) **Reactive Ion Etched** – placed face-up in a Trion RIE. This time they were etched for much longer than 2000s, however.

The silicon dioxide on the tops of the silicon wafers newly exposed by mask 2 seemed unable to be etched in the same amount of time as the silicon dioxide previously exposed by mask 1, or even in a much larger amount of time. It is believed that the first layer of photoresist may not have been removed properly and is still shielding portions of the oxide that need to be etched. Processing of the silicon wafers was thus paused here until a better way to strip the photoresist could be found.

A few more things were done to test the fabrication process further, though. The next step in machining the silicon wafers would have been to etch the shape of mask 2 into the wafers themselves. This would have involved deep reactive ion etching of the silicon – a process meant to etch vertical sidewalls that can be sensitive to the specific recipe used. It was therefore deemed important to test the process parameters and observe the resulting etch profiles to determine in advance what parameters might need to be adjusted and whether the required depth could be reached. For this study coin-rolled wafers – lower quality silicon wafers that are even less expensive than those used previously – were acquired and:

- 1.) **Piranha Cleaned** – placed in a fresh solution of H_2SO_4 and H_2O_2 , and then rinsed with water.
- 2.) **BOE Cleaned** – placed in a 10:1 buffered oxide etch solution to remove any native oxide on their surfaces, rinsed with calcium chloride to neutralize the solution, and then water.
- 3.) **Patterned with Photoresist** – covered in HMDS, covered on top with $1.3\mu m$ of HPR504, softbaked, and then exposed to UV light through mask 2 for 2.8s – 3.0s. The exposed photoresist was then etched with developer 354.
- 4.) **Deep Reactive Ion Etched** – Bosch-etched in an Oxford Plasma Lab 100 ICP RIE to a depth of approximately $30\mu m$.
- 5.) **Stripped of Photoresist** – placed in a Branson 3000 Barrel Etcher where the remaining photoresist was carried away in an oxygen plasma.
- 6.) **Cleaved** – placed face-up on a soft surface, where their edges were nicked with a diamond pen. This revealed the cross-sections of the etch.
- 7.) **Covered in Gold** – attached to holders with carbon tape to help ground them, and placed in a Denton SEM Gold Sputter Unit. The thin layer of gold sputtered on them is meant to improve the conductivity of their surfaces.
- 8.) **Inspected** – arranged inside a LEO 1430 Scanning Electron Microscope (SEM) and viewed from various angles.

Figures 4.16 and 4.17 are examples of what could be seen with the SEM. They show the scallops on the sidewalls of the structures left by the Bosch process and the type of surface that can be expected at the bottom of such an etch – which will be similar to the type of surface on the bottoms of the movable combs and springs of the finished prototypes. Although not a mirror-finish, the surface is generally flat enough that the structures on the other side of it can be assumed to be of a uniform thickness even with the occasional pillar (created by micro-masking from an imperfectly-clean substrate). Examining the edge of the wafer in the foreground of Figure 4.16, it would seem that the etch produced sidewalls at an angle slightly greater than 90° to the substrate. With this sort of profile it is expected that the thin spring beams will retain their thickness, and may even be a bit stiff; on the other hand, further inspection should be made of the depth of the gaps between the teeth of design A.

4.9.3 Process Recommendations

Although not all of the fabrication process parameters were able to be tested in the first fabrication runs, a few things were learned from them that could be used to improve the process for future trials.

The oxygen plasma recipe used to take the remaining photoresist off of the coin-rolled wafers, for instance, may be what is needed to strip the burnt photoresist from the silicon wafers. Also, it should be mentioned here that the first etch of the oxide on top of the silicon wafers caused the second layer of photoresist to streak as it was spun onto the wafers, creating considerable

inconsistencies in the thickness of the photoresist layer. It is unknown how these inconsistencies may affect subsequent etches without attempting them (i.e. whether the thin spring beams will be masked properly by the uneven photoresist, or whether thicker areas of the photoresist will be able to be exposed all the way through). It is thought that perhaps a much thinner layer of metal – 100nm of aluminium or chromium – could have been used to mask the silicon instead of the oxide. This would have lessened the roughness of the topography the photoresist would have to be spread over. It may also shield the etch of the insulator layer of each SOI wafer better than simply a thicker layer of the same material as the insulator layer, and, it could perhaps be left on the contacts of the combs to improve their conductivity – which would eliminate some of the final processing steps.

4.10 Conclusions

To explore what further potential vertical comb drives may have for being used in applications outside of the telecommunications industry, an attempt was made at designing a vertical comb-driven piston that could push on the diaphragm of a typical reciprocating displacement micropump. During this attempt a fabrication process for such a piston was put together, and from it was derived the piston's basic design. The dimensions of the prototypes to be fabricated were decided upon by considering the forces that would be exerted on their pistons in various directions.

In attempting to predict the performance of the prototypes in terms of the maximum static piston displacements that could be expected from them for a particular applied voltage, a disadvantage of using vertical comb drives for piston-motion was realized: their limited possible displacement does not allow them to be analysed in the same manner a lateral comb drives – the fringe effects caused by the corners of their opposing comb teeth approaching one another must be taken into account, particularly when predicting the final static displacement of their movable combs. An analytical expression was found in the literature that offers a fringe-correction to the equation typically used to analyse comb drives, that takes into account the positions of their tooth corners in a one-dimensional sense. This was compared to finite and boundary element simulation data obtained from three-dimensional models of the prototypes, and a numerical expression was ultimately derived to replace the analytical expression.

Finally, the prototypes were partially fabricated, and the optimization of the fabrication process was begun.

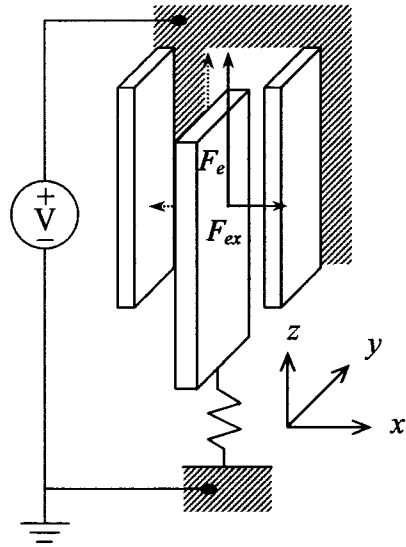


Figure 4.1: The electrostatic forces that act on a movable tooth in the z - and x -directions when a voltage difference is applied between the fixed and movable combs.

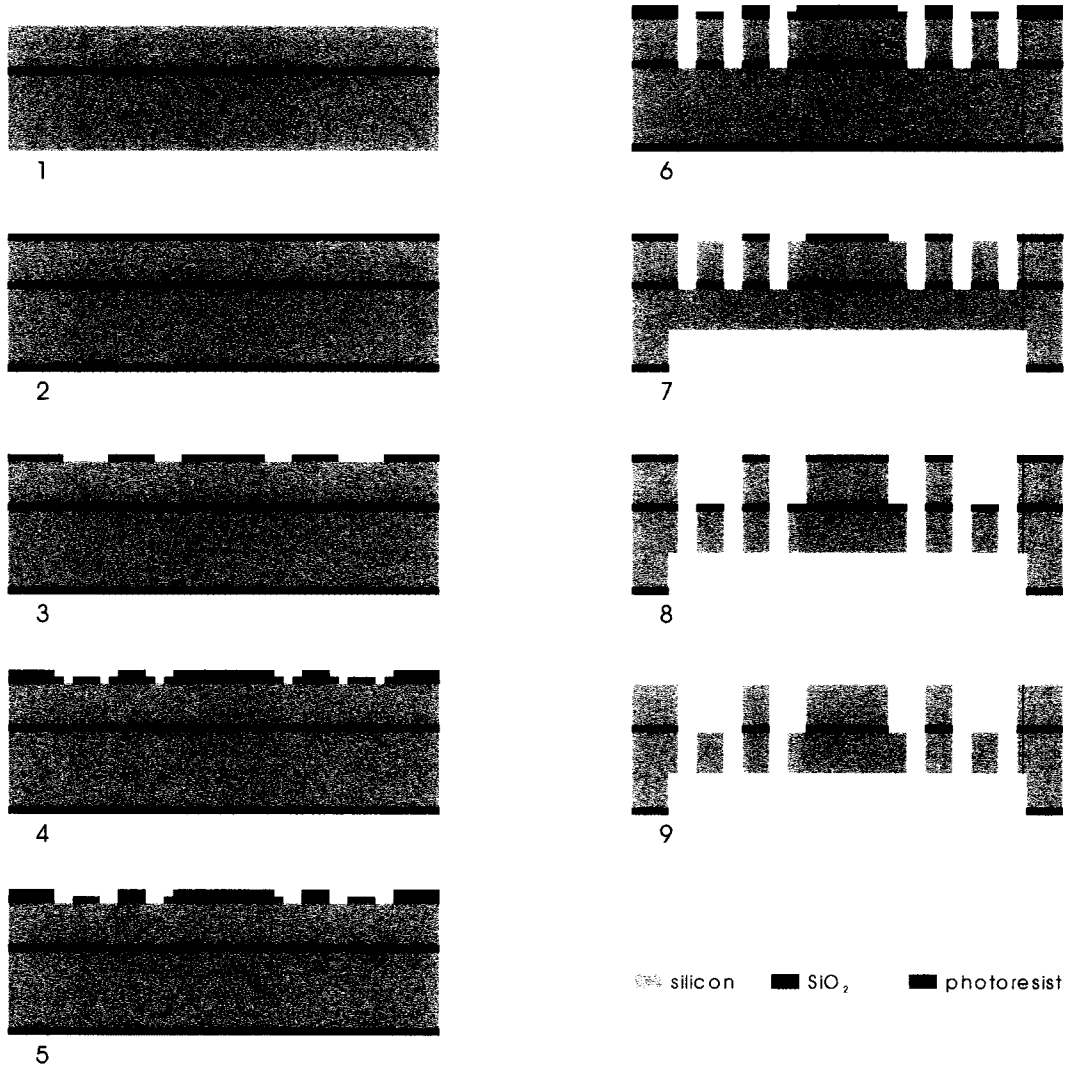


Figure 4.2: The process decided upon for the fabrication of the vertical comb-driven prototypes.

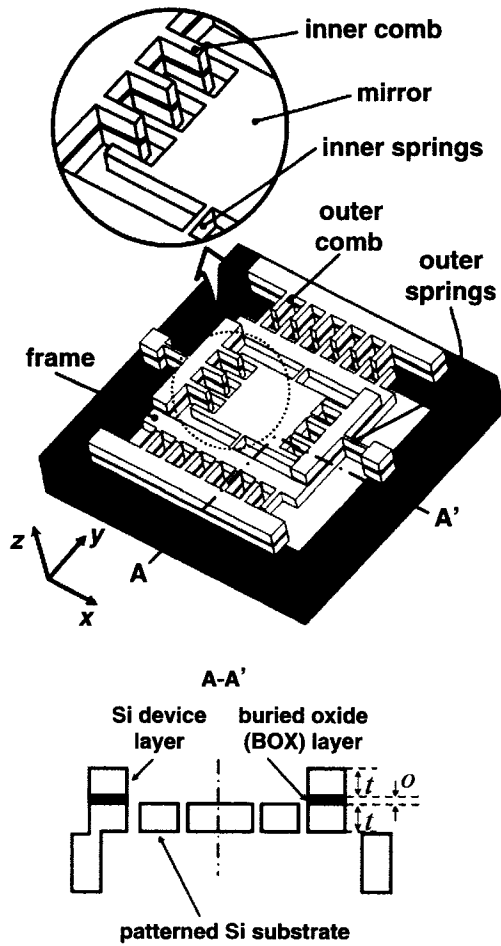


Figure 4.3: A schematic of the double-gimbaled two-axis tilting micromirror that the chosen fabrication process is intended to make. Adapted [26].

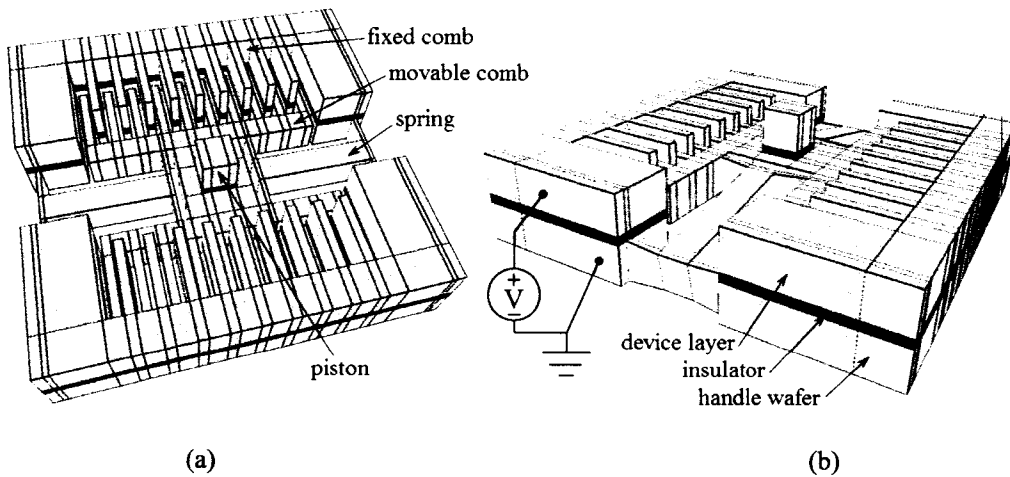


Figure 4.4: Schematics of the basic piston design at rest (a) and during actuation (b). Model built in IntelliSuite™'s 3D Builder™ module and deformed in the ThermoElectroMechanical Analysis™ module.

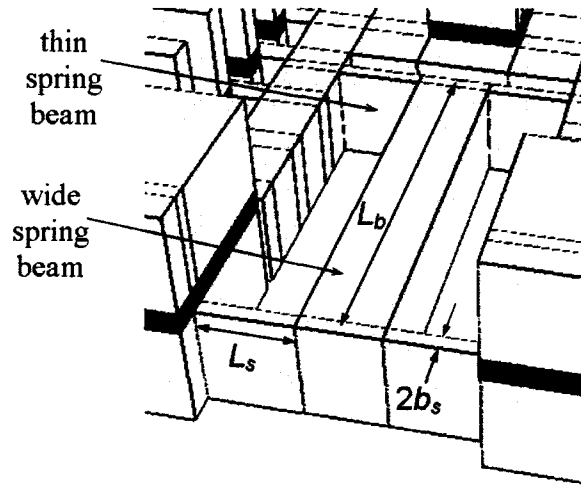


Figure 4.5: A close-up of the piston schematic showing the dimensions of the spring beams. Model built in IntelliSuite™'s 3D Builder™ module.

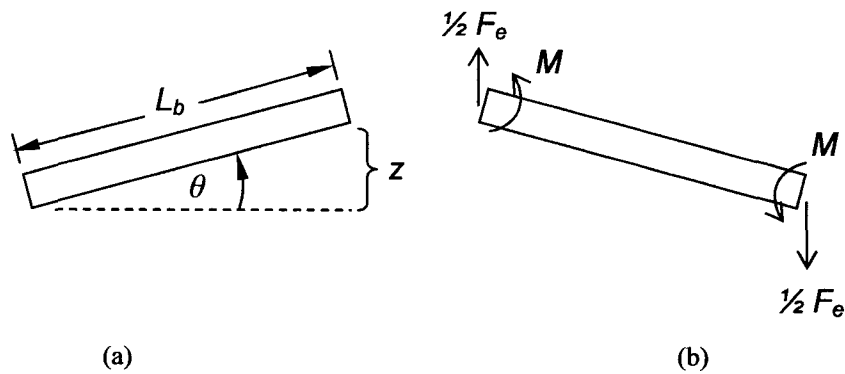


Figure 4.6: Side-views of the wide spring beams. (a) shows the relationship between the displacement of their ends and the angle they are raised to; (b) the forces and moments exerted on their ends.

Table 4.1: A summary of the dimensions and other characteristics of the three piston designs.

Design A		
Dimensions Dependent on Design Parameters		
gap between teeth (g)		3 μ m
overlapping tooth length (L_t)		75 μ m
number of movable teeth (n)		100
wide beam length (L_b)		475 μ m
thin beam length (L_s)		65 μ m
thin beam width ($2b_s$)		3 μ m
Dimensions not Dependent on Design Parameters		
wide beam width (w_b)		50 μ m
movable comb width (w_m)		25 μ m
tooth width (w)		5 μ m
space at ends of teeth (s)		5 μ m
Given Dimensions		
tooth thickness (t)		15 μ m
initial vertical offset (o)		0.5 μ m
Material Properties		
modulus of elasticity (E)		130.2GPa
bulk shear modulus (G)		79.4GPa
permittivity of air (ϵ)		8.85E-12F/m
Calculated Properties		
spring constant in x (k_x)		384.0 μ N/ μ m
side-sticking criteria:		
z	$[\partial F_x/\partial x]_{x=0}$	portion of k_x
(μ m)	(μ N/ μ m)	(%)
9.5	159.3	41.5
11.0	185.9	48.4
12.5	212.4	55.3
14.0	239.0	62.2
15.5	265.5	69.1
voltage difference (V)		60V
spring constant in z (k_z)		5.11 μ N/ μ m
Initial Estimates of Performance		
net electrostatic force (F_e)		79.7 μ N
vertical displacement (z)		15.6 μ m

Table 4.1: Continued.

Design B		
Dimensions Dependent on Design Parameters		
gap between teeth (g)		4 μ m
overlapping tooth length (L_t)		100 μ m
number of movable teeth (n)		140
wide beam length (L_b)		425 μ m
thin beam length (L_s)		70 μ m
thin beam width ($2b_s$)		4 μ m
Dimensions not Dependent on Design Parameters		
wide beam width (w_b)		50 μ m
movable comb width (w_m)		60 μ m
tooth width (w)		5 μ m
space at ends of teeth (s)		5 μ m
Given Dimensions		
tooth thickness (t)		15 μ m
initial vertical offset (o)		0.5 μ m
Material Properties		
modulus of elasticity (E)		130.2GPa
bulk shear modulus (G)		79.4GPa
permittivity of air (ϵ)		8.85E-12F/m
Calculated Properties		
spring constant in x (k_x)		728.8 μ N/ μ m
side-sticking criteria:		
z	$[\partial F_x/\partial x]_{x=0}$	portion of k_x
(μ m)	(μ N/ μ m)	(%)
9.5	282.3	38.7
11.0	329.3	45.2
12.5	376.3	51.6
14.0	423.4	58.1
15.5	470.4	64.5
voltage difference (V)		90V
spring constant in z (k_z)		13.38 μ N/ μ m
Initial Estimates of Performance		
net electrostatic force (F_o)		250.9 μ N
vertical displacement (z)		18.8 μ m

Table 4.1: Concluded.

Design C		
Dimensions Dependent on Design Parameters		
gap between teeth (g)		3.5 μ m
overlapping tooth length (L_t)		85 μ m
number of movable teeth (n)		110
wide beam length (L_b)		470 μ m
thin beam length (L_s)		60 μ m
thin beam width ($2b_s$)		3.5 μ m
Dimensions not Dependent on Design Parameters		
wide beam width (w_b)		50 μ m
movable comb width (w_m)		40 μ m
tooth width (w)		5 μ m
space at ends of teeth (s)		5 μ m
Given Dimensions		
tooth thickness (t)		15 μ m
initial vertical offset (o)		0.5 μ m
Material Properties		
modulus of elasticity (E)		130.2GPa
bulk shear modulus (G)		79.4GPa
permittivity of air (ϵ)		8.85E-12F/m
Calculated Properties		
spring constant in x (k_x)		775.3 μ N/ μ m
side-sticking criteria:		
z	$[\partial F_x / \partial x]_{x=0}$	portion of k_x
(μ m)	(μ N/ μ m)	(%)
9.5	313.5	40.4
11.0	365.8	47.2
12.5	418.0	53.9
14.0	470.3	60.7
15.5	522.5	67.4
voltage difference (V)		95V
spring constant in z (k_z)		8.76 μ N/ μ m
Initial Estimates of Performance		
net electrostatic force (F_e)		213.4 μ N
vertical displacement (z)		24.3 μ m

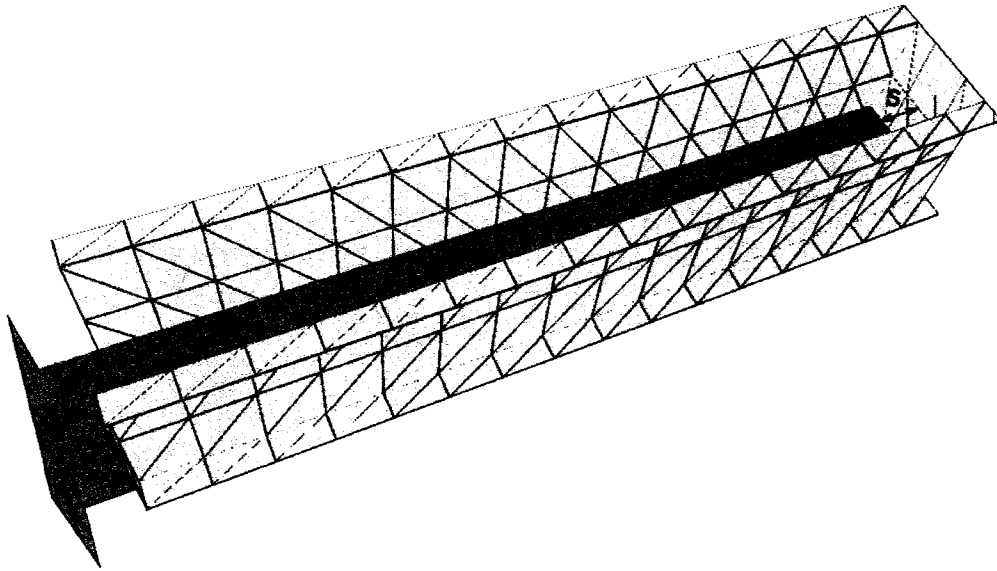


Figure 4.7: An electrostatic boundary element mesh of a unit comb drive showing the w and s dimensions. Model built in IntelliSuite™'s 3D Builder™ and ThermoElectroMechanical Analysis™ modules.

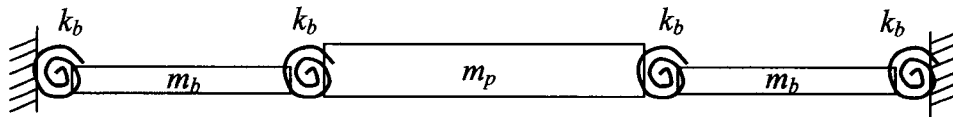


Figure 4.8: The model used to estimate the natural frequencies of the three piston designs. $k_b = 2KG/L_s$.

Table 4.2: The first three natural frequencies of the piston designs predicted with finite element simulations.

Natural Frequency	A (Hz)	B (Hz)	C (Hz)
p_1	2514	2781	2919
p_2	6578	6708	7939
p_3	7366	7278	8017

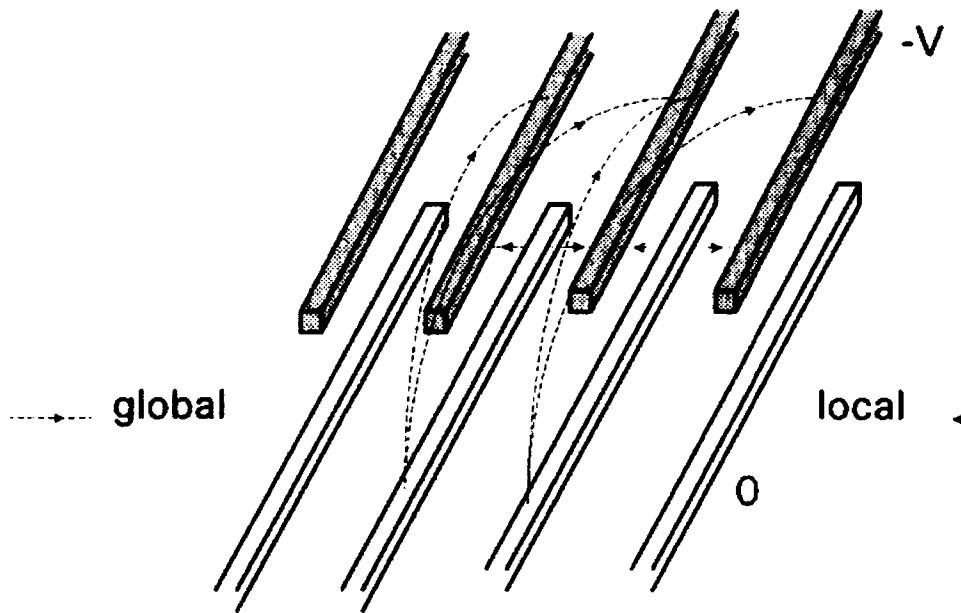


Figure 4.9: A schematic of opposing comb teeth showing the difference between the electrostatic forces occurring within the region directly between them (local forces), and the electrostatic forces occurring outside of this region (global forces). Adapted [39].

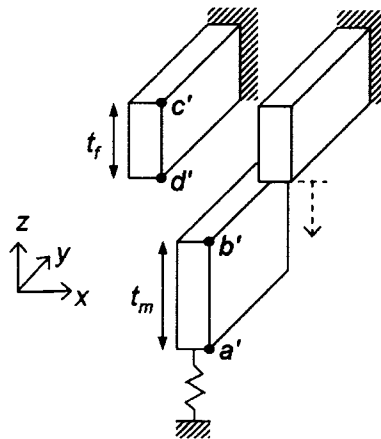
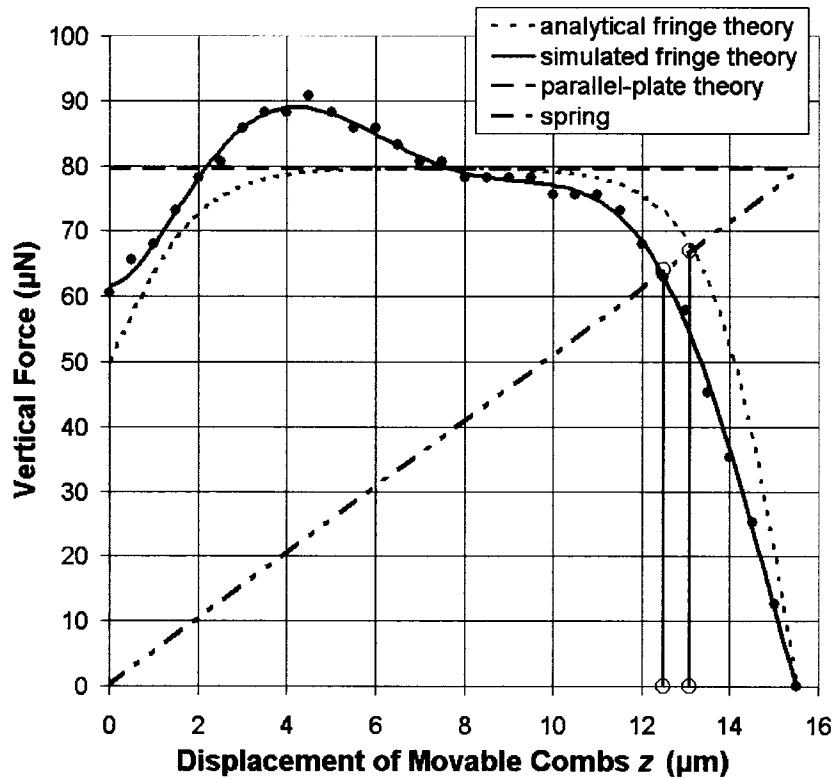
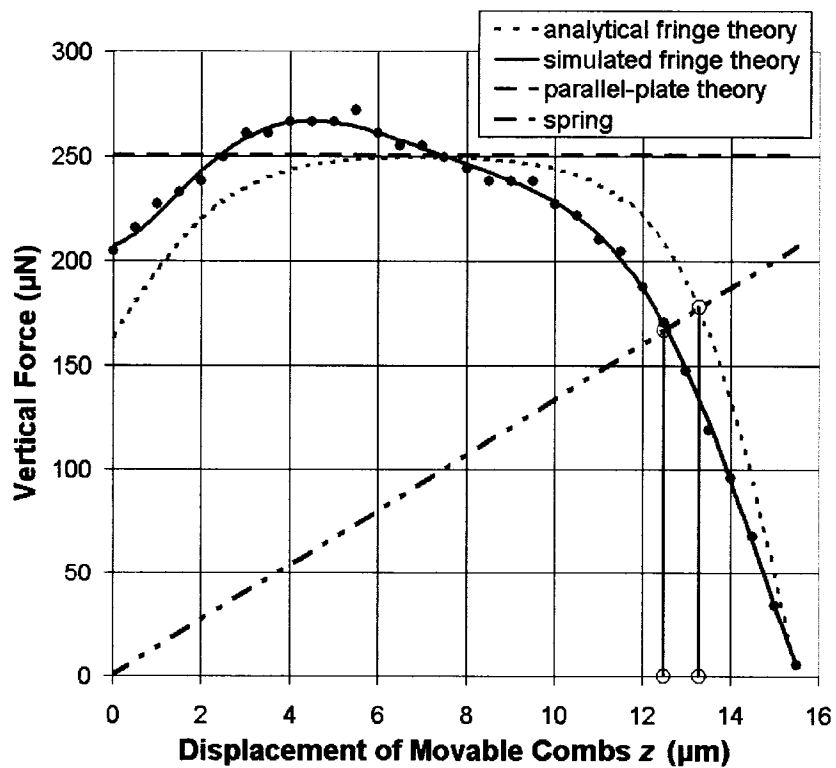


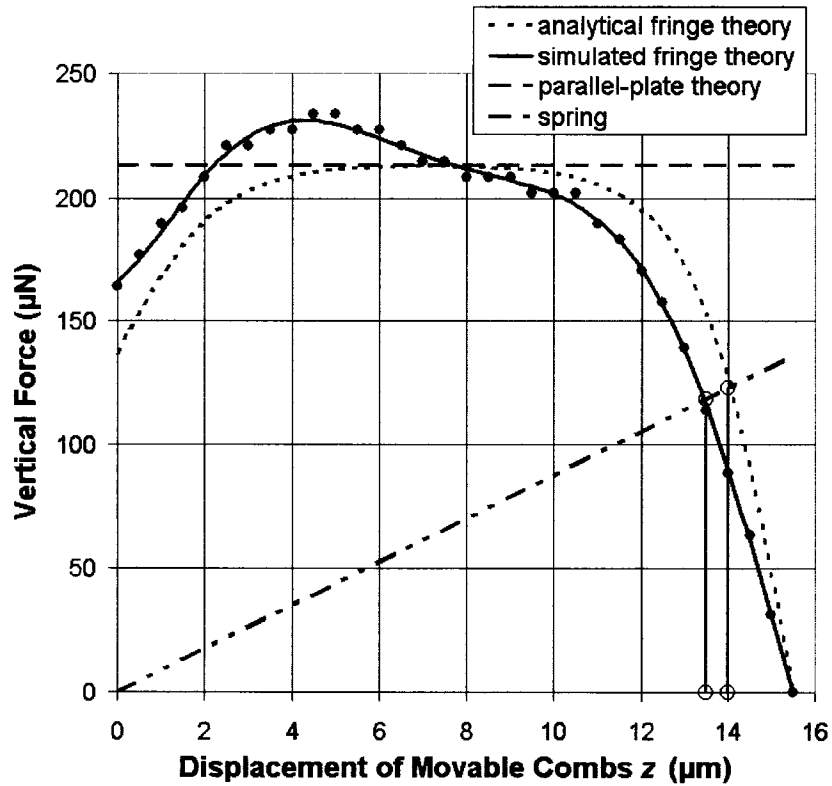
Figure 4.10: A schematic of opposing comb teeth displaying some of the dimensions used in the analytical fringe correction given in Equations 4.10 – 4.19.



(a)



(b)



(c)

Figure 4.11: A comparison of the proposed electrostatic force models on prototypes A (a), B (b), and C (c).

Table 4.3: A summary of the final displacements of the three pistons predicted with different electrostatic theories.

Design		A	B	C
displacements predicted by:	intersection of "analytical fringe theory" & "spring" lines	13.1µm	13.3µm	14.0µm
	intersection of "simulated fringe theory" & "spring" lines	12.5µm	12.5µm	13.5µm
	simulation conducted with full piston model	9.0µm	11.5µm	---

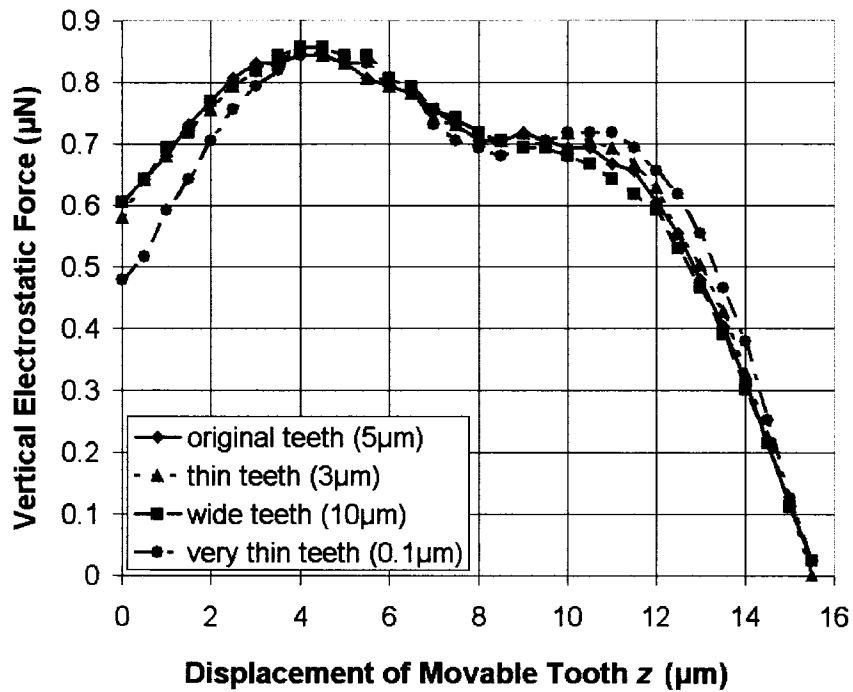


Figure 4.12: A study of the effect of tooth width, w , on the magnitude of the electrostatic force exerted on the movable teeth of a comb drive.

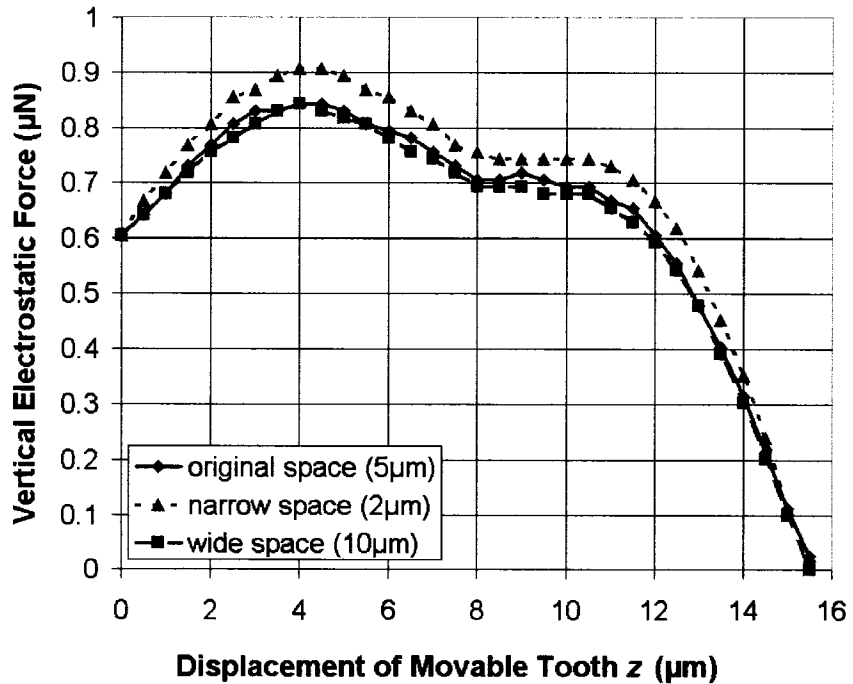


Figure 4.13: A study of the effect of the distance between the ends of the teeth and the inside walls of the opposing combs, s , on the magnitude of the electrostatic force exerted on the movable teeth of a comb drive.

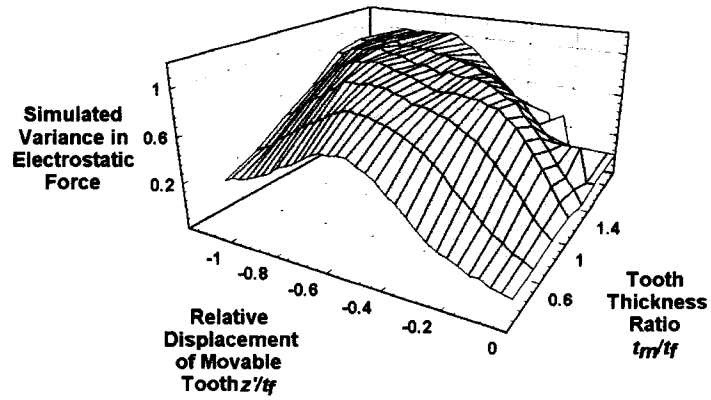
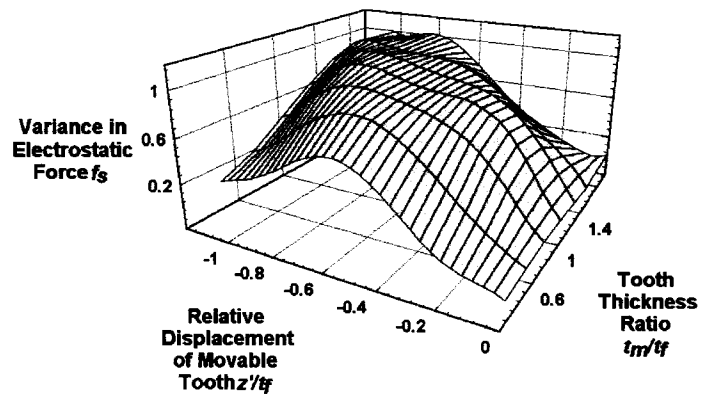
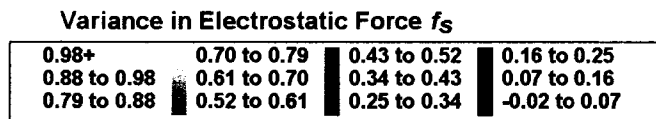
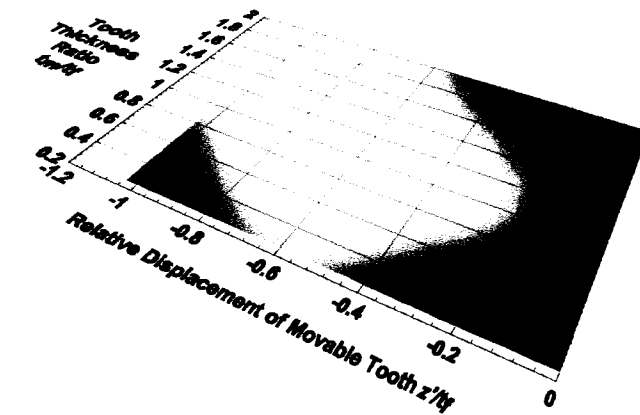


Figure 4.14: The simulation data used to derive the numerical fringe correction.



(a)



(b)

Figure 4.15: The surface (a) fit to the simulation data and a contour plot (b) of this same surface.

Table 4.4: The coefficients of the fringe-correction derived from simulation data.

$a \begin{matrix} / \\ i \end{matrix} \begin{matrix} \backslash \\ j \end{matrix}$	0	1	2	3	4
0	-0.0368413	0.0585756	0.20089	-0.291962	0.0917768
1	-2.4601	4.16221	-0.928224	-5.88943	2.90735
2	-7.26628	-124.203	475.365	-444.2	120.414
3	-8.14573	-876.518	2841.36	-2498.69	653.372
4	-3.06406	-1869.41	5858.19	-5092.25	1323.91
5	-1.12141	-1624.01	5085.25	-4427.49	1153.44
6	-1.03266	-503.245	1593.69	-1396.31	365.45

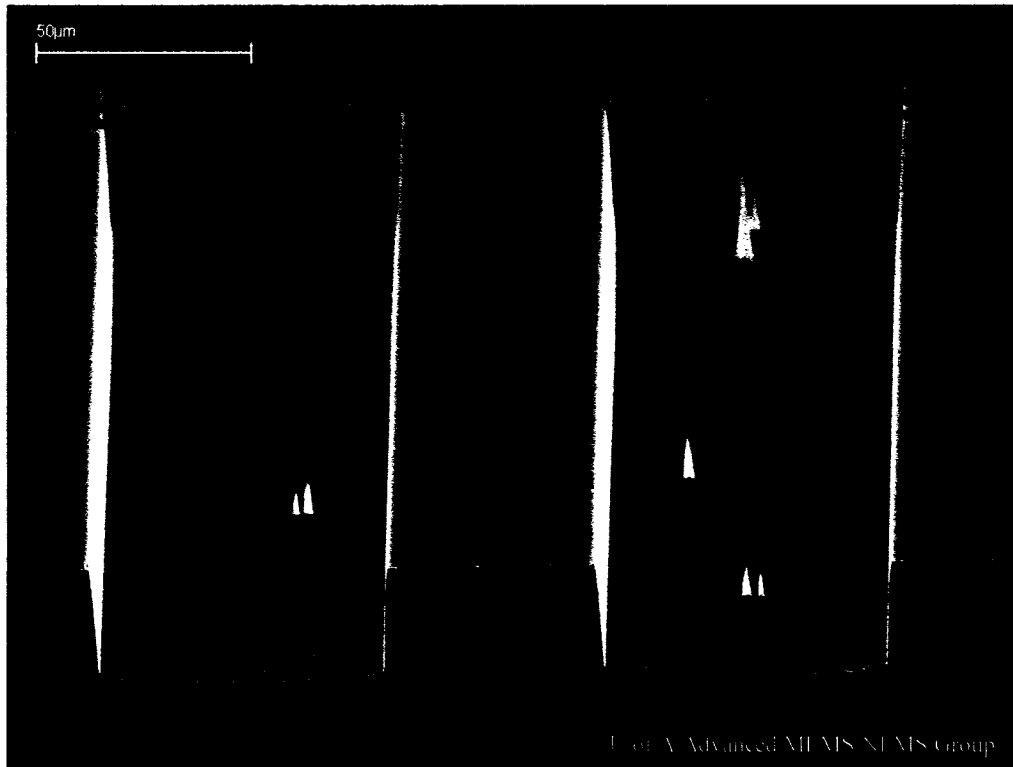


Figure 4.16: An SEM picture of the cross-section of one of the Bosch-etched coin-rolled wafers.

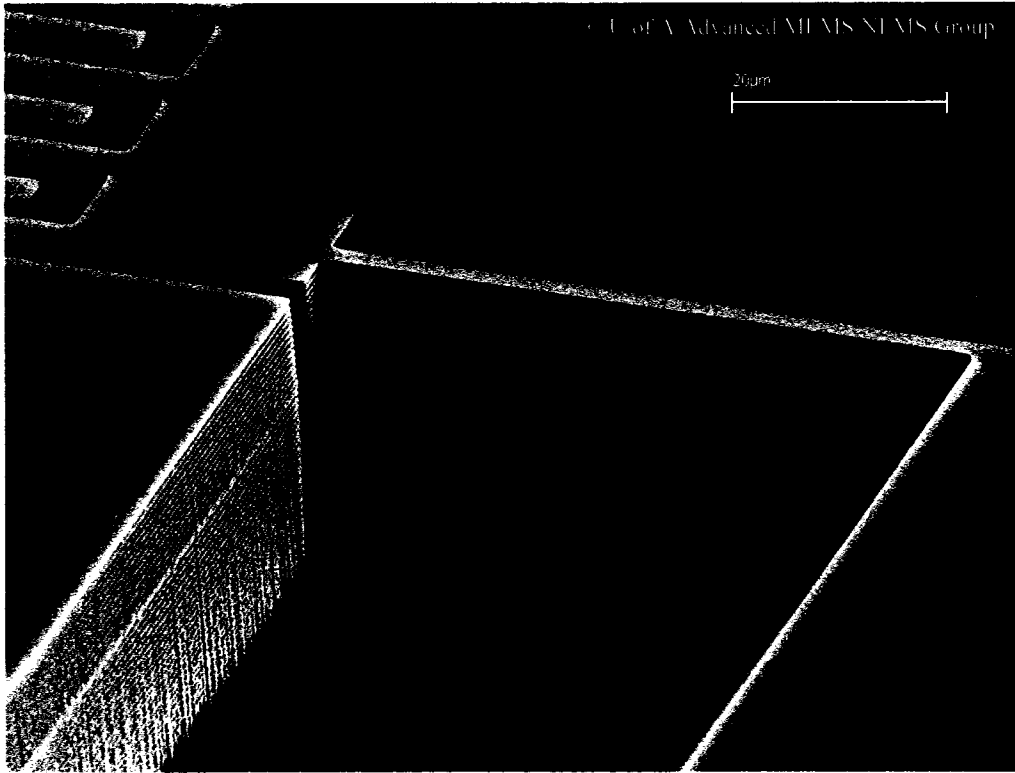


Figure 4.17: An SEM picture of a thin spring beam Bosch-etched from one of the coin-rolled wafers.

Chapter 5: Conclusion

The objective of the research presented here was to explore the capabilities of comb drives by designing a system where one is used to actuate a micropump. Micropumps have a number of important applications in a variety of fields that place a variety of design constraints on them, and, while many different types of drivers for them have been studied, there are many that have not yet been explored – and there are still a number of applications for micropumps that are awaiting compatible designs. While comb drives have a number of applications themselves, their compatibility with applications other than their current ones is something that should be studied further.

Two attempts were made at connecting comb drives with micropumps; such components not being naturally compatible, both attempts involved designing a new type of one or the other. In both attempts the prototypes were designed to be machined out of SOI wafers, so that they would not need to be annealed part-way through the fabrication process, their opposing combs could easily be isolated from each other, and the thicknesses of their springs and comb teeth would not be limited by surface micromachining technologies. The relatively standard process steps that were carried out on the wafers included growing silicon dioxide hard masks on top of their device layers, patterning these photolithographically, and anisotropically etching through the silicon layers such that the prototype components etched from them would have vertical sidewalls.

The first attempt made at pairing a comb drive with a micropump involved designing a type of micropump that could be connected to a standard comb drive. A typical comb drive design was taken and modified to be attached to a piston, and a pump chamber, valves, and microchannels were arranged around it that could be machined beside the comb drive with minimal added process steps. All three masks required for the resulting system were drawn, and several prototypes were partially fabricated – in an initial round involving only the process steps required for the comb drives themselves (such that the pumps would have their internal components etched from the device layers of SOI wafers, with their movable components freed from the handle wafers with a partial etch of the insulator layers) – so that these steps could be optimized before further ones were carried out to complete the pumps. From the low yield of working prototypes it was determined that both the system design and fabrication process will need some adjustment before complete prototypes of the micropumps can be manufactured. However, although some ideas were considered as to what these adjustments should be, it was decided that another approach altogether should be taken with designing a comb-driven micropump, as from this initial attempt it is suspected, particularly because of leakage and other efficiency concerns, that

standard comb drives, without converting their motion into something non-standard, may not be the best type of actuator for micropumps.

The second attempt made at pairing a comb drive with a micropump involved designing a type of comb drive that could be connected to a standard micropump – in the hope that the diaphragm of a standard micropump would prevent leakage of the working fluid into the comb drive components, and that larger net electrostatic forces could be generated from lower voltage differences with comb teeth that can easily be machined to be long in the direction relevant to the magnitudes of such forces. This new type of comb drive is very similar to a type normally used for tilting micromirrors, and this attempt is based on the idea that whether such comb drives can be used in other applications should be examined. A fabrication process for a mirror-tilting comb drive – that had its fixed and movable teeth etched from either the device layer or handle wafer of an SOI wafer, respectively, and aligned by being patterned with one mask – was selected from the literature and modified to suit the new application. The design it was intended for was also modified – its mirror was replaced with a piston, and its springs were re-designed to allow pure vertical motion (as opposed to torsional).

Sets of governing equations, considering the electrostatic and restoring forces that would be exerted on the movable combs of the comb drive, were assembled to assist in deciding on the dimensions of prototypes. Again, all three masks required for the prototypes were drawn, and some fabrication process optimization was started, but more needs to be done before it can be said whether such a comb-driven micropump could find a useful application. However, during the design of the prototypes, and specifically, while attempting to predict the maximum static displacements that can be expected from their pistons, something was realized regarding this new type of comb drive: when used in the manner intended here, its motion is limited such that there is only a short distance over which its fixed and movable teeth will properly overlap so that fringe effects can be ignored when predicting the net electrostatic force that will be generated between them. Normally, because their teeth move parallel to each other, the net electrostatic forces generated within comb drives can be assumed to remain constant over their actuation. The electric field generated between parallel plates, if they are large enough and close enough together, can be approximated as being uniform (as the fringing-fields around the corners of the plates can be neglected). Thus the electrical potential energy between the plates (the derivative of which is usually taken as the net electrostatic force between them) varies only linearly with their displacement in a single direction. Unfortunately, for this new type of comb drive the decrease in the net electrostatic force as its movable teeth begin to align with its fixed will need to be considered when trying to predict at what piston displacement this force will balance the restoring force exerted by its springs.

Some literature was found that proposes an analytical expression to characterize, in a one-dimensional sense, the variance in the net electrostatic force in a comb drive as its movable teeth displace relative to its fixed. It was compared to finite and boundary element simulations conducted with three-dimensional models of the new type of comb drive, and the static displacements

of the prototypes were predicted graphically by examining where the various proposed electrostatic force curves intersected the restoring-force lines (with slopes equal to that of the calculated spring constants). Finally, with further boundary element simulations of three-dimensional models, an alternate, numerical, expression to characterize the variance in the net electrostatic force in a comb drive was derived by fitting a polynomial surface to simulation data obtained for opposing comb teeth with various different thickness ratios.

5.1 Future Work

Work will continue in exploring the capabilities of comb drives by taking an even closer look at predicting the fringe effects that occur within them. Upon closer examination of the non-dimensionalized simulation results for the net electrostatic forces occurring in the prototypes of the new type of comb drive, they were found to vary between prototypes – if only by a small amount – but in a predictable manner, which implies that perhaps the parallel-plate assumptions normally made for comb drives need to be studied even further. Since all of the relevant dimensions of the prototypes were varied from one to another, an additional parametric study will need to be conducted where only one dimension of the models is changed at a time.

The process optimization for the new type of comb drive can also be continued, and once prototypes are completed they can be probed under an optical profilometer to measure the final displacements of their pistons. Also, the pump to be attached to this type of comb drive could be designed. It is likely that such a design would begin with simply the pump's diaphragm – the material to be used could be chosen, as well as its desired thickness. What stiffness such a diaphragm would add to the system will need to be considered, and most likely modeled with finite elements, and plans would need to be made as to how to attach it to this type of comb drive.

Finally, work will also continue in exploring the capabilities of comb drives by seeing whether this new type of comb drive – likely in the form of a sensor, rather than an actuator – can be used in the tips of atomic force microscopes to ease their calibration and extend their range of applications.

Bibliography

- [1] J. S. Denker. (2004). Definition of Anode and Cathode [Online]. Available: <http://www.av8n.com/physics/anode-cathode.htm>
- [2] B. Wilson. (2003, June 20). Applying Metal/Sputtering [Online]. Available: <http://cnx.org/content/m11369/1.1/>
- [3] M. J. Madou, *Fundamentals of Microfabrication: The Science of Miniaturization*, 2nd ed.. Boca Raton, FL: CRC Press, 2002, pp. 1 – 6, 78, 79, 85, 97, 99, 100, 104, 105, 107, 131 – 134, 138 – 140, 285, 294 – 297, 299 – 302.
- [4] J. W. Gardner, V. K. Varadan, and O. O. Awadelkarim, *Microsensors, MEMS, and Smart Devices*. New York: Wiley, 2001, pp. 10 – 21, 23 – 27.
- [5] W. C. Tang, T.-U. H. Nguyen, and R. T. Howe, “Laterally driven polysilicon resonant microstructures,” *Sens. Actuators*, vol. 20, no. 1 – 2, pp. 25 – 32. Nov. 1989.
- [6] V. P. Jaecklin, C. Linder, N. F. de Rooij, and J. M. Moret, “Micromechanical comb actuators with low driving voltage,” *J. Micromech. Microeng.*, vol. 2, no. 4, pp. 250 – 255. Dec. 1992.
- [7] *A Deep Silicon RIE Primer: Bosch Etching of Deep Structures in Silicon*, University of Alberta Nanofab, Edmonton, AB, April 2002.
- [8] D. J. Laser and J. G. Santiago, “A review of micropumps,” *J. Micromech. Microeng.*, vol. 14, no. 6, pp. R35 – R64. June 2004.
- [9] P. H. Pham, D. V. Dao, S. Amaya, R. Kitada, and S. Sugiyama, “Straight movement of micro containers based on ratchet mechanisms and electrostatic comb-drive actuators,” *J. Micromech. Microeng.*, vol. 16, no. 12, pp. 2532 – 2538. Dec. 2006.
- [10] V. P. Jaecklin, C. Linder, and N. F. de Rooij, “Comb actuators for xy-microstages,” *Sens. Actuators*, vol. A 39, no. 1, pp. 83 – 89. Sept. 1993.
- [11] C. Chen, C. Lee, and Y.-J. Lai, “Novel VOA using in-plane reflective micromirror and off-axis light attenuation,” *IEEE Communications Magazine*, vol. 41, no. 8, pp. S16 – S20. Aug 2003.
- [12] D. Halliday, R. Resnick, and J. Walker, *Fundamentals of Physics – Extended*, 5th ed.. New York: Wiley, 1997, pp. 629 – 637.
- [13] R. Legtenberg, A. W. Groeneveld, and M. Elwenspoek, “Comb-drive actuators for large displacements,” *J. Micromech. Microeng.*, vol. 6, no. 3, pp. 320 – 329. Sept. 1996.
- [14] C. Liu, *Foundations of MEMS*. Upper Saddle River, NJ: Pearson Prentice Hall, 2006, pp. 133, 134.
- [15] G. K. Fedder, “MEMS fabrication,” in *itc*, 2003, pp. 691 – 698.
- [16] T. Zhou, Micralyne Inc., Edmonton, AB, private communications, 2003 – 2005.
- [17] S. L. Miller, *et al.*, “Failure modes in surface micromachined microelectromechanical actuation systems,” *Microelectronics Reliability*, vol. 39, no. 8, pp. 1229 – 1237. Aug. 1999.

- [18] M. I. Kilani, P. C. Galambos, Y. S. Haik, and C.-J. Chen, "Design and analysis of a surface micromachined spiral-channel viscous pump," *ASME J. Fluids Eng.*, vol. 125, no. 2, pp. 339 – 344. March 2003.
- [19] J.-L. A. Yeh, H. Jiang, and N. C. Tien, "Integrated polysilicon and DRIE bulk silicon micromachining for an electrostatic torsional actuator," *J. MEMS*, vol. 8, no. 4, pp. 456 – 465. Dec. 1999.
- [20] J.-H. Lee, *et al.*, "SOI-based fabrication processes of the scanning mirror having vertical comb fingers," *Sens. Actuators*, vol. A 102, no. 1 – 2, pp. 11 – 18. Dec. 2002.
- [21] U. Krishnamoorthy, D. Lee, and O. Solgaard, "Self-aligned vertical electrostatic combdrives for micromirror actuation," *J. MEMS*, vol. 12, no. 4, pp. 458 – 464. Aug. 2003.
- [22] J. M.-L. Tsai, H.-Y. Chu, J. Hsieh, and W. Fang, "The BELST II process for a silicon high-aspect-ratio micromachining vertical comb actuator and its applications," *J. Micromech. Microeng.*, vol. 14, no. 2, pp. 235 – 241. Feb. 2004.
- [23] V. Milanović, "Multilevel beam SOI-MEMS fabrication and applications," *J. MEMS*, vol. 13, no. 1, pp. 19 – 30. Feb. 2004.
- [24] D. Hah, S. T.-Y. Huang, J.-C. Tsai, H. Toshiyoshi, and M. C. Wu, "Low-voltage, large-scan angle MEMS analog micromirror arrays with hidden vertical comb-drive actuators," *J. MEMS*, vol. 13, no. 2, pp. 279 – 289. April 2004.
- [25] V. Milanović, G. A. Matus, and D. T. McCormick, "Gimbal-less monolithic silicon actuators for tip-tilt-piston micromirror applications," *IEEE J. Quantum Electronics*, vol. 10, no. 3, pp. 462 – 471. May/June 2004.
- [26] D. Hah, C.-A. Choi, C.-K. Kim, and C.-H. Jun, "A self-aligned vertical comb-drive actuator on an SOI wafer for a 2D scanning micromirror," *J. Micromech. Microeng.*, vol. 14, no. 8, pp. 1148 – 1156. Aug. 2004.
- [27] V. Milanović, S. Kwon, and L. P. Lee, "High aspect ratio micromirrors with large static rotation and piston actuation," *IEEE Photonics Tech. L.*, vol. 16, no. 8, pp. 1891 – 1893. Aug. 2004.
- [28] K.-H. Jeong and L. P. Lee, "A novel microfabrication of a self-aligned vertical comb drive on a single SOI wafer for optical MEMS applications," *J. Micromech. Microeng.*, vol. 15, no. 2, pp. 277 – 281. Feb. 2005.
- [29] Q. X. Zhang, A. Q. Liu, J. Li, and A. B. Yu, "Fabrication technique for microelectromechanical systems vertical comb-drive actuators on a monolithic silicon substrate," *J. Vac. Sci. Technol.*, vol. B 23, no. 1, pp. 32 – 41. Jan./Feb. 2005.
- [30] E. T. Carlen, K.-H. Heng, S. Bakshi, A. Pareek, and C. H. Mastrangelo, "High-aspect ratio vertical comb-drive actuator with small self-aligned finger gaps," *J. MEMS*, vol. 14, no. 5, pp. 1144 – 1155. Oct. 2005.
- [31] D. Hah, *et al.*, "Low voltage MEMS analog micromirror arrays with hidden vertical comb-drive actuators," *2002 Solid-State Sensor, Actuator, and Microsystems Workshop*, Hilton Head, pp. 11 – 14.

- [32] J. Kim, S. Park, and D.-I. Cho, "A novel electrostatic vertical actuator fabricated in one homogeneous silicon wafer using extended SBM technology," *Sens. Actuators*, vol. A 97 – 98, pp. 653 – 658. April 2002.
- [33] S. Kwon, V. Milanović, and L. P. Lee, "Large-displacement vertical microlens scanner with low driving voltage," *IEEE Photonics Tech. L.*, vol. 14, no. 11, pp. 1572 – 1574. Nov. 2002.
- [34] W. C. Young and R. G. Budynas, *Roark's Formulas for Stress and Strain*, 7th ed.. McGraw-Hill, 2002, ch. 10.
- [35] J. Kim, D. Cho, and R. S. Muller, "Why is (111) silicon a better mechanical material for MEMS?" *11th International Conference on Solid-State Sensors and Actuators*, Munich, 2001, pp. 662 – 665.
- [36] T. Hirano, T. Furuhashi, K. J. Gabriel, and H. Fujita, "Design, fabrication, and operation of submicron gap comb-drive microactuators," *J. MEMS*, vol. 1, no. 1, pp. 52 – 59. March 1992.
- [37] S. D. Senturia, *Microsystem Design*. Boston: Kluwer Academic Publishers, 2001, append. C.
- [38] G. McKinnon, Norcada, Edmonton, AB, private communications, 2005 – 2006.
- [39] W. A. Johnson and L. K. Warne, "Electrophysics of micromechanical comb actuators," *J. MEMS*, vol. 4, no. 1, pp. 49 – 59. March 1995.
- [40] J.-L. A. Yeh, C.-Y. Hui, and N. C. Tien, "Electrostatic model for an asymmetric combdrive," *J. MEMS*, vol. 9, no. 1, pp. 126 – 135. March 2000.
- [41] I. S. Gradshteyn and I. M. Ryzhik, *Table of Integrals, Series, and Products*, 6th ed., A. Jeffrey, Ed., D. Zwillinger Assoc. Ed., translated from the Russian by Scripta Technica, Inc. San Diego: Academic Press, 2000, pp. 851, 852.
- [42] S. Bozic, University of Alberta Nanofab, Edmonton, AB, private communication, May 2006.